EFFECT OF MONOMERIC BINDING AFFINITY ON SCAFFOLD MEDIATED PROTEIN AGGREGATION:

by

Candace Kay Goodman

A dissertation submitted in partial fulfillment
of the requirements for the degree

of

Doctor of Philosophy

in

Chemistry

MONTANA STATE UNIVERSITY
Bozeman, MT

January 2015

DEDICATION

This work is dedicated to my baby boy, wonderful husband and entire supportive family.

ACKNOWLEDGEMENTS

There are many people I have been blessed to interact with and encouraged me in my decision to attend graduate school and continue through to the bitter end. Thanks to Greg Gillispie for the inspiration and challenge; whose Socratic methods of teaching made me into the scientist I am. Thank you to Mary Cloninger for her compassion and motivation. No matter how terrible I felt before entering her office, I would leave with hope and inspiration. Greg and Mary are the role models I aspire to be.

I would not have attended college, let alone graduate school if not for my parents. Thank you Jeff and Laurel Furniss for encouraging and, at times, pushing me to achieve all I can. Hard work and dedication puts all goals within reach.

As with most dissertations, I would like to thank members of the Cloninger Lab: Mark Wolfenden for his preliminary work on which the basis of my galectin-3 studies were performed; Amanda Mattson for her 'tell it like it is' nature and beautiful mind; Anna Michal for our philosophical talks and her attempts at restricting my commitments; Jessica Ennist for her patience, questions and understanding, and for scolding me when I did take on additional commitments. And to the boys in the other office-Jon, Harrison, Sam and Ed. Special thanks are due to Megan Neufield, Jenni Monaco, Nikki Brown and Jaci Smith: your presence played to my extroverted strengths, I like to think. And Kurt Peterson at Fluorescence Innovations for help with the plate readers when I needed it.

Mostly, I need to thank my husband and sweet little boy. Thank you Chris, for cheering me on during the last half mile of this marathon. Thank you Connor for your love and yes, dinosaurs are "ex-stink".

TABLE OF CONTENTS

TABLE OF CONTENTS - CONTINUED

LIST OF TABLES

LIST OF TABLES - CONTINUED

Table Page

LIST OF FIGURES

LIST OF FIGURES - CONTINUED

Figure Page

LIST OF FIGURES - CONTINUED

LIST OF FIGURES - CONTINUED

Figure Page

ABSTRACT

The intermolecular interactions that occur in a system determine the degree and duration of the contact. They govern processes from signaling and recognition to aggregation and tumor formation. The ability to control and affect intermolecular processes requires an understanding of the assembly process and factors modulating the assembly, such as the strength of individual interactions (binding affinity) and the number of interactions between molecules (valency). Functionalized PAMAM dendrimers were used as nucleating scaffolds to study the significance of intermolecular interactions on aggregate assembly. Dendrimers functionalized with biotin, lactose and mannose units spontaneously aggregated when added to the appropriate protein binding partner (streptavidin, galectin-3, and Concanavalin A, respectively). Aggregates were characterized to provide insight regarding the effects of binding affinity, protein valency and concentration on the average diameter, regularity (polydispersity) and kinetics of aggregate formation. A number of tools were used in this investigation, including dynamic light scattering (DLS), fluorescence microscopy (FM) and fluorescence lifetime spectroscopy (FLS). FLS instrumentation was reconfigured to enable high thoughput formats. A discussion of the validation and re-design of the FLS instrumentation is included.

INTRODUCTION, BACKGROUND AND RATIONALE

Assembly Progression in Terms of Binding

Molecular interactions are responsible for a significant portion of chemical and biological processes. The binding of small molecules such as drugs and hormones, for example, can stimulate or inhibit cellular responses. Similarly, addition of phosphate groups to proteins regulates processes such as transcription, mitosis, apoptosis and degradation.[1, 2, 3] Intermolecular interactions also result in formation of higher order oligomers, supramolecular complexes and macromolecular assemblies.[4] The existence of such systems is a consequence of molecular interactions overcoming the entropic favorability of disassembly. The significance of the interaction depends on the number and strength of binding events. Engineering of systems able to attenuate or stimulate the formation of large complexes requires understanding of individual interactions and their contribution overall. This is especially useful when disease is the result of the created complex.

Molecular interactions can be classified as monovalent or multivalent based on the complexity of binding. In the simplest case, monomeric binding, there are two entities involved each interacting in a one-to-one ratio. Schematically, this is represented by Figure 1.1 below.[5]

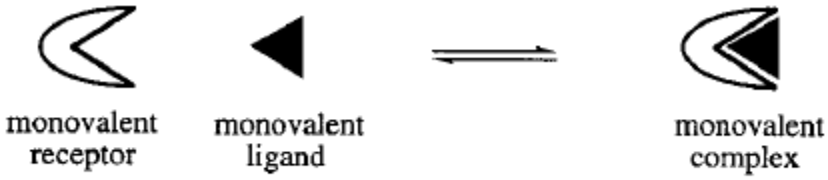

Figure 1.1. Monovalent interaction between a ligand and receptor (taken from reference 5).

The binding constant, which for most biochemists is expressed as the dissociation constant, K_d, characterizes the strength of an interaction. Strong, good and weak binding are thought of as interactions with less than nanomolar, millimolar, and micromolar to molar dissociation constants, respectively.[6] To compensate for the generally weak binding affinity of monovalent interactions multiple ligand-receptor pairs may form. Recognizing molecular crowding and the complexity in the composition of cellular and tissue environments, it seems reasonable to consider multiple ligand-receptor pairs. The number of ligand-receptor pairs reflects the valency of the system. Multivalent systems benefit from significant affinity enhancements, typically greater than the sum of individual affinities.[5;7,8] Studies have shown affinity enhancement occurs regardless of the scaffold architecture selected for ligand display, although more significant increases in avidity were observed for large, flexible and more densely decorated polymers. [9] The affinity enhancement is a result of several factors. The presentation of multiple ligands simultaneously, as done by multivalent frameworks, increases the probability of contact between receptor and ligand (Figure 1.2 and Figure 1.3, d). This is analogous to increasing the local concentration and is described as proximity/statistical effects. Simultaneous binding of two ligands to a single receptor is known as the chelate effect due to the similarity between this and polydentate ligand binding to a central atom

(conventional chelation). The chelate effect can occur as a result of identical interactions (Figure 1.2) or with two distinct interactions on the same molecule (Figure 1.3, c).

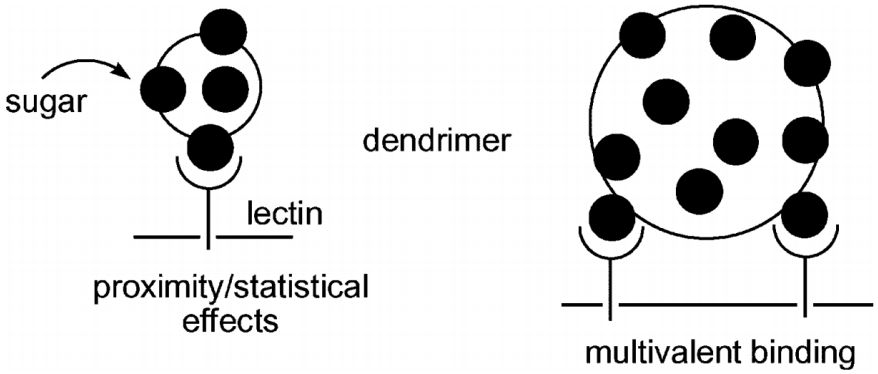

Figure 1.2. Examples of proximity/statistical effect and multivalent binding characteristic of multi-ligand display using dendritic architectures.[10]

One consequence of multivalent interactions is crosslinking through the polymeric scaffold. Crosslinking generally refers to when ionic or covalent bonds tether polymers to create a complex matrix or network. The physical characteristics such as the strength and flexibility of the material can be tuned through chemical crosslinking. Crosslinking occurs at several levels in natural systems, some of which have negative consequences. In order to design mechanisms to disrupt or interfere with crosslinking an understanding of the significance of contributing effects (such as statistical and multivalent effects) must be clarified. The dynamics of the ensemble and the system in which it's contained must also be considered. The following discussion elaborates on naturally observed multivalent systems and the negative crosslinking events that can occur.

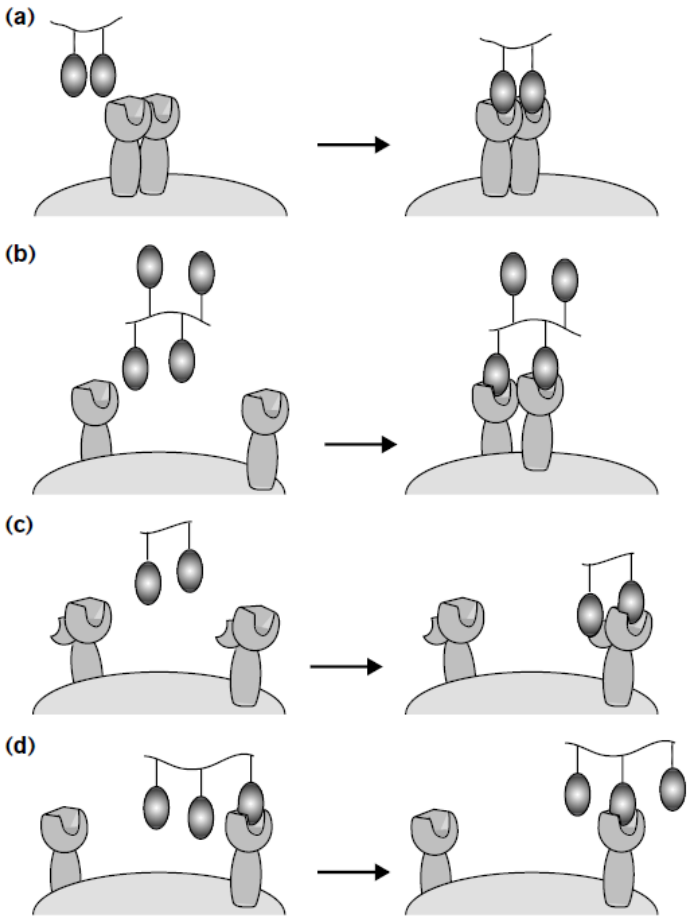

Figure 1.3. Interactions contributing to affinity enhancement of multivalent interactions, specifically speaking to cell-surface interactions. Multivalent ligands can bind to (a) clustered receptors or (b) recruit nearby receptors. (c) The presence of additional binding sites within the same receptor demonstrates chelation effects. (d) Enhancement by increased local concentration of ligand (statistical/proximity effect).[11]

Natural Polyvalency: Protein Oligomerization and Repeating Sugar Units

Cross linking is present at several levels in natural systems. At the cellular level cross linking within the extracellular matrix between multivalent receptors and ligands can result in cellular aggregation or tumor formation.[12] Multivalent ligands containing repeating entities were recognized within the cellular environment as early as 1966.[13] The tandem array presentation of sugars can be found on glycoproteins and glycolipids

contained in cellular membranes and serve as poly-ligated structures for oligomeric proteins to engage in multivalent interactions. These carbohydrate-protein interactions are responsible for cellular recognition (Figure 1.4) and stimulating immune responses. Not completely understood is the relation between the glycosylation patterns, their biological role, and their relation to disease.[14] For example, over expression of the glycoprotein mucin 1 (MUC1) has been correlated to poor prognosis in colorectal cancer suggesting glycoproteins may play a role in this cancer's progression.[15] Kotera *et al*. points out the "aberrant glycosylation of mucins by tumor cells has been shown to result in the differential expression of novel mucin epitopes that are associated with tumors."[16] For this reason, highly glycosylated proteins are candidates for disease biomarkers and targets in drug delivery systems.[17]

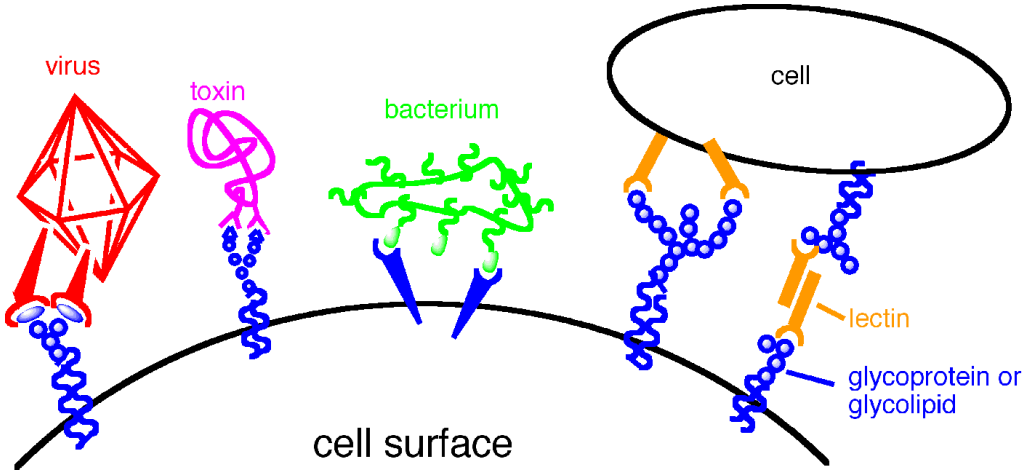

Figure 1.4: Cellular multivalent interactions as recognition beacons.

Cross-linking also occurs among proteins. It is well known that the polypeptide subunits participate in homo- and heteromeric interactions. As well stated by Lalonde *et al.*, these interactions are "…crucial for all levels of cellular function, including

architecture, regulation, metabolism and signaling."[18] Longstanding complexes that are favorable under physiologically relevant concentrations are assigned the native oligomeric state of a protein. This suggests that the oligomeric state of a protein plays a role in the function of the protein and that this is a significant property to characterize. Evolutionarily, oligomerization offers several advantages including diversity in chemical composition which provides opportunity for additional control (allosterism), and reduction of errors in peptide sequencing due to the generation of shorter sequences.[4] Given that binding constants for monomeric interactions are typically weak, oligomerization is also a mechanism for proteins to attain increased valency.

Proteins are highly flexible entities, existing in multiple conformations. The structure of each conformation has a higher propensity for interacting with specific binding partners, and the population distribution of conformers is hypothesized to shift as a result of binding.[19-21] The concentration dependence of specific protein-protein interactions implies expression levels could correlate to valency and crosslinking potential of the system. When the equilibrium of a system is altered, or the protein becomes misfolded, proteins can increase their ability to associate and cross link. Crosslinking at this level results in receptor clustering and formation of inclusion bodies, folding aggregates and amyloid fibers.[22,23] Once in the aggregated state, some proteins lose the ability to function properly, leading to diseases such as Alzheimer's, Parkinson's, Huntington's , Type II diabetes and cancer.[24, 25] Aggregation in lab settings prevents key properties from being studied and prevents the study of some proteins altogether. Synthetic molecules that can mimic multivalent environments can guide our

understanding of molecular recognition and signaling processes. Possible treatments for protein aggregation diseases could ultimately emerge.

PAMAM Dendrimers as Scaffolds to Study Aggregation

Many synthetic multivalent frameworks have been developed for the study of multivalency and aggregation processes. Gold nanoparticles, quantum dots, star polymers, linear polymers, hyperbranched polymers, and arrays on surfaces, for example, have been reported. [11] Given that the free energy of a system results from both enthalpic and entropic contributions, varying the architecture of a polyvalent scaffold offers additional tunabilty to the synthetic molecule. Dendrimers are an attractive system from which to study and mediate protein aggregation because of their highly modular and systematic nature. Poly(amidoamine) (PAMAM) dendrimers are well-defined, water soluble, symmetric scaffolds with a controlled and tuneable number of end groups.[26] The number of end groups is dictated by the dendrimer generation and approximately doubles for each subsequent generation as shown in Figure 1.5. The amine termini can be functionalized with a variety of molecules, making these scaffolds an excellent choice for systematic studies of chemical and biological phenomena.[27,28]

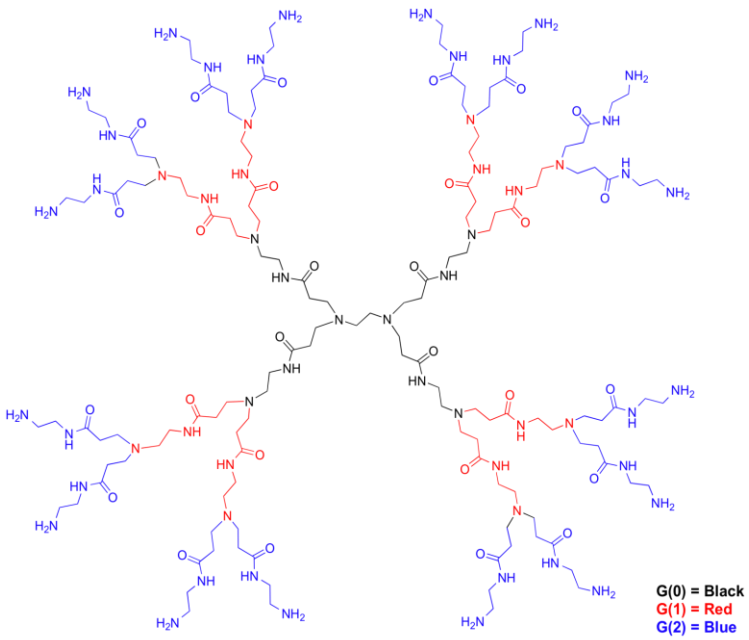

Figure 1.5. Generation 2 PAMAM dendrimer.

Review of Aggregation Characterization Methods

Techniques for monitoring protein aggregation include calorimetry, electron microscopy, light scattering, circular dichroism, surface plasmon resonance, quartz crystal oscillator, mass spectrometry, fluorescence (using intrinsic and extrinsic probes) and turbidity. However, most techniques are unable to resolve the multivalent binding event from cross-linking that causes aggregation. For a complete review of physical methods to monitor protein aggregation see the supporting information in reference 29. Each method has an operable concentration range that depends on the limits of detection and relies on different properties of the interaction to characterize it. Methods such as turbidity and absorbance are simple and straightforward to measure but distinguishing size or shape is impossible. Calorimetry uses temperature changes relative to a reference cell to determine thermodynamic parameters and overall very effectively tracks the

effects of large scale aggregation. Calorimetry is incapable of resolving multivalent interactions from aggregation. Conventional fluorescence techniques rely on signals from dyes, e.g., Thioflavin T,[30] Nile Red,[31] and 1-Anilinonaphthalene-8-Sulfonic Acid[32], that undergo emission shifts as a result of binding to exposed hydrophobic areas and thus are an indirect measurement of aggregation.[33] Electron microscopy (EM) is another example of an indirect method where the actual measurement is of backscattered electrons reflecting off the surface of the sample. EM can provide information on the morphology and size, but the atomic resolution capabilities of EM make attaining accurate descriptions of the sample distribution difficult (a very high number of images are required to get a statistically meaningful evaluation). [29] Fluorescence intensity measurements are susceptible to increased noise and scatter due to aggregation, making it difficult to evaluate data collected using this method. Therefore, aggregation is likely to require multiple techniques for full characterization. The research reported here used three methods in tracking mono- and multivalent interactions: fluorescence lifetime spectroscopy, dynamic light scattering and fluorescence microscopy.

Fluorescence lifetime spectroscopy (FLS) measures the photon-emitting relaxation of an electron in a photo-excited molecule. This technique is insensitive to concentration and is independent of scatter, making it better than conventional fluorescence intensity measurements. The challenge for FLS is to position the fluorophore within the system to effectively monitor the aggregation process. Both binding affinity of a receptor-ligand interaction and the stability of an aggregate formation can be studied using FLS. Novel instrumentation allows rapid data collection,

making this technique desirable for conducting multiparameter experiments. While fluorescence lifetime can provide information on the strength and duration of an interaction, the short timescale of typical fluorescence decays prohibit size characterization of large particles, such as aggregates.

However, if a fluorophore is integrated into the aggregate, fluorescence microscopy techniques allow direct visualization of the particles. Sensing through specific attachment of a fluorophore to a protein of interest is not a novel concept. Attachment either through interaction with dye-labeled antibodies or fusion to a fluorescent protein, has provided valuable insight regarding expression and localization of proteins within a cell.[34,35] This has been extended to nanoparticle characterization *in vitro* and *in vivo* to determine concentration and metabolism of fluorescently labeled nanoparticles.[36, 37] The benefit of FM over EM is that samples can remain in the liquid phase and the resolution allows one to sample a greater population of molecules. While it does not permit the atomic resolution of EM, aggregate morphology can still be evaluated at the nm-μm scale.

Another technique for evaluating the size and population distribution of aggregates is dynamic light scattering. When light is scattered by spherical, non-interacting particles, randomly moving according to Brownian motion, the time-correlated decay rate can be fit to determine molecular diffusion. Approximation of particle radius comes from assumption that the cubic molecular weight is inversely proportional to diffusion.[38] This method has proven useful in nanoparticle characterization and polymer assembly.[39, 40]

Summary

Interactions of ligand and receptor molecules are not limited to single entities. Rather, multivalent systems comprised of a series of ligand/receptor interactions occur often and are more realistic of nature. The dynamics of the ensemble and the system in which it's contained must also be considered.

The ability to create and to study systems from which the effect of valency, the entropic and enthalpic contributions of multivalent systems, and the tipping factors that cause interactions to result in disease are significant. Dendrimers are macromolecules with already proven therapeutic potential, and as such they are effective tools for the study of multivalent biologically relevant processes.[30, 41-44] Increased understanding of multivalency allows rational design of macromolecules such as dendrimers to be created to intervene and/or to prevent aggregation diseases. Dendrimers of variable cores and modifiable endgroups provide the flexibility needed to create disease specific mediators. Dendrimers can also serve as a mimic of the cellular environment for the study of multivalent interactions.

The measurement and evaluation of complex multivalent interactions is essential for understanding biological recognition and signaling processes. Conventional techniques often have limited utility in the study of multivalent interactions since processes such as aggregation (energy due to loss of solvation) must be considered.

Research provided in this thesis builds on previous work using PAMAM dendrimers to mimic the cellular environment and create complex assemblies. Specifically, investigations of the effect of valency and binding affinity on the nucleation

and aggregation of proteins to a functionalized scaffold were conducted. This work is significant for the remediation of diseases that result from protein aggregation. Light was the primary vector used in this investigation. Light scattering, light emitted as a form of energy release, and light as a molecular beacon are all reported here for viewing and characterizing multicomponent systems involved in complex and multivalent interactions. The development of new spectroscopic methods and analyses for multivalent interactions is reported here and holds vast potential for future work.

Organization

Introduction of fluorescence lifetime spectroscopy, the novel direct waveform recording approach developed by Fluorescence Innovations, and how it can provide a solution to the need for high-throughput fluorescence lifetime instrumentation are discussed in the proceeding chapter. Design modifications to previously developed, cuvette-based instruments to afford a microplate format are shown, along with results from calibration and validation experiments.

The possible applications of fluorescence lifetime spectroscopy are introduced in the third chapter, including binding constant determination, chemical denaturation, and measuring reaction kinetics. It is in this chapter that discussion of multivalent interactions begins. Studies to (1) determine binding constants for galectin-3 and different size lactose-functionalized dendrimers, (2) investigate the native oligomerization state of galectin-3 through chemical denaturation, and (3) characterize

aggregation kinetics for mixtures of mannose-functionalized dendrimers and the well characterized plant lectin Concanavalin A were performed.

Further studies of multivalent systems using dynamic light scattering, fluorescence microscopy and UV-Vis spectroscopy to evaluate the effect of monomeric binding constants and valency on the size, morphology and stoichiometry of scaffold-induced aggregates are the focus of Chapter 4. In addition to the two previously mentioned systems (Concanavalin A with mannose-functionalized dendrimers and galectin-3 with lactose functionalized dendrimers), streptavidin and biotin-functionalized dendrimers were also evaluated.

Chapter 5 provides a summary of the results presented in chapters 3 and 4. The first section speculates on the role and oligomeric state of galectin-3, followed by suggestions for additional experiments to further elucidate its function and the effects of post-translational modifications on function. The final section discusses the potential for multivalent scaffolds as therapeutic agents in aggregate related diseases and also discusses suggested assay development for characterizing these molecules.

CHAPTER 2

FLUORESCENCE LIFETIME SPECTROSCOPY

Introduction to Fluorescence and Fluorescence Lifetime Spectroscopy

Fluorescence is a mechanism for molecules to release energy via emission of light. In the simplest case there are 3 processes attributed to fluorescence: (1) photon absorption, (2) internal conversion and (3) photon emission. Absorption of electromagnetic radiation by molecules results in a transition from the ground electronic state (S_0) to any of the vibrational levels of an excited electronic state (S_1, S_2), as depicted by blue arrows in the Perrin-Jablonski diagram shown below (Figure 2.1). Molecules then undergo rapid thermal equilibration (on the order of 10^{-12} s). This is known as internal conversion (Figure 2.1, black dashed arrows) and populates the lowest energy vibrational level of the lowest energy electronic excited state (S_1). Further relaxation, which in fluorescence is coupled with photon emission, returns the molecule to a vibrational level of the ground electronic state (Figure 2.1, green arrows). Due to internal conversion, emission spectra are typically independent of excitation wavelength (Kasha's rule) and reflect the S_1 to S_0 transition. The shape of emission spectra will depend on the vibrational energy level spacing and interactions with surrounding matter (solvent or ligand). Each $S_1 \rightarrow S_0$ transition creates a peak in the spectra whose wavelength and intensity are determined by the energy gap and probability, respectively. The electronic transitions between two widely spaced states will emit higher energy photons and the

more probable transitions will create more photons, producing higher signals. Molecules displaying more structured spectra possess more vibrational energy states.

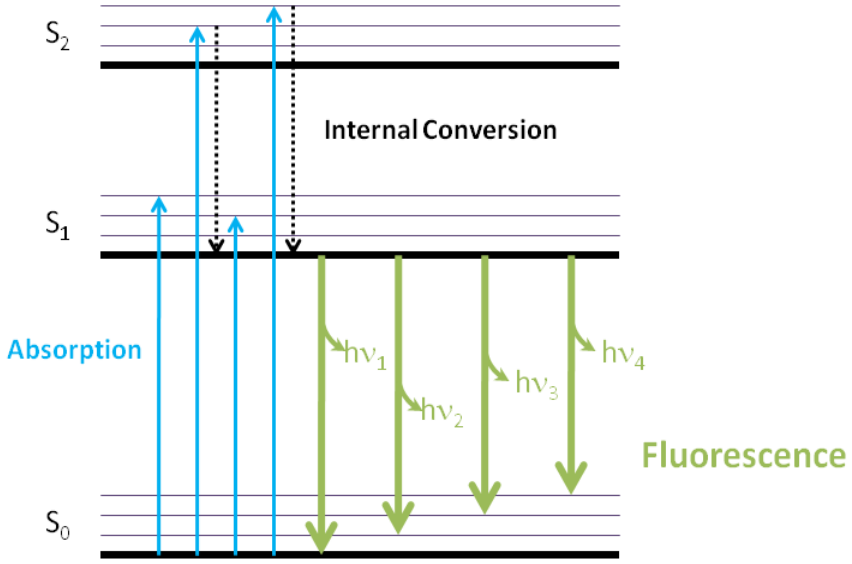

Figure 2.1: Perrin-Jablonski diagram of photon absorption and emission processes.

Emission spectra are influenced by a fluorophore's local environment. Solvent effects, complex formation, energy transfer, etc., can all result in a shift in the emission spectra. For example Figure 2.2 shows the emission spectra of native (dashed line) and a denatured form (solid lines) of cottonseed protein isolates (CSPI). Both the alkaline soluble fraction and total protein isolate, CSPa and CSPI respectively, display an approximate 15 nm red shift for the solvent exposed, denatured form relative to the native folded protein isolates. The water soluble cottonseed extract fraction (CSPw) did not show a spectral response with addition of denaturant suggesting that the tryptophan of proteins in this fraction were already solvent accessible. [45]

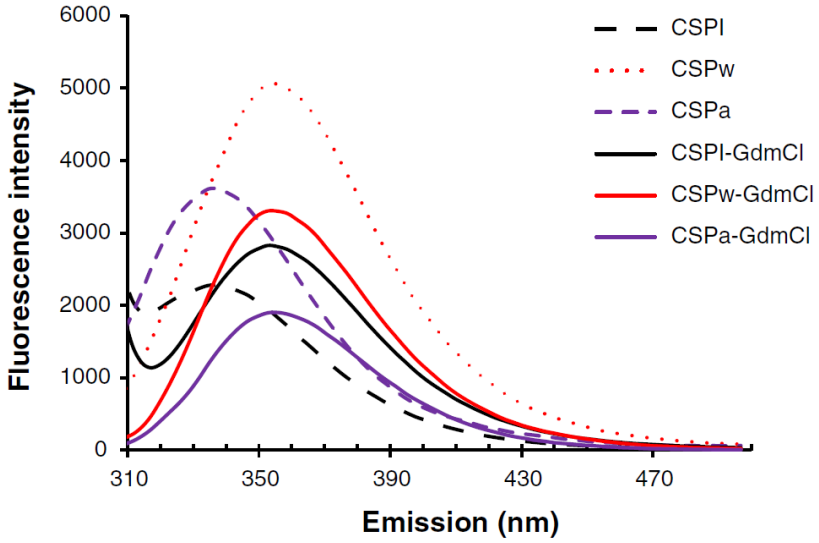

Figure 2.2. Fluorescence emission spectra of cottonseed protein isolate (CSPI, black), cottonseed protein water soluble fraction (CSPw, red) and alkali soluble fraction (CSPa, purple) collected under conditions promoting native (dashed line) and denatured (solid line) conformations. Shifts to longer wavelengths, as seen for the denatured form of CSPI and CSPa are commonly observed when fluorophores become solvent exposed.[45]

Changes in emission spectra have become a valuable tool for researchers to observe product formation,[46] ligand interactions and characterize segmental motions of a protein.[47] The total shift observed between emission and absorption spectra, caused by combined effects of internal conversion and the environmental factors listed above, is known as the Stoke's shift.

The most common fluorescence signal that is measured is steady-state fluorescence or fluorescence intensity. Steady-state fluorescence is a measure of the average number of the photons emitted over a long period of time (typically milliseconds or seconds), enough time for the system to reach a photoequilibrium. Steady-state fluorescence measured as a function of emission wavelength is referred to as the emission

spectrum (Figure 2.3, b). Likewise, steady-state fluorescence measured as a function of excitation wavelength is an excitation spectrum.

Fluorescence lifetime (FL), or the time dependent intensity decay of a sample, reflects the average time a molecule spends in an excited state, and typically occurs on the order of 0.1-10 ns. Steady-state fluorescence can be determined by integrating the signal of time-resolved measurements (Figure 2.3). The FL can be acquired by measuring the intensity decay using a pulsed light source (time-domain), or using the amplitude and phase changes of an intensity modulated light source (frequency-domain). Since the instrumentation discussed within is a type of time-domain measurement, frequency-domain fluorometry will not be discussed and all future references to time-resolved data implies intensity decays collected in the time domain. Conventionally, time-resolved data is referred to as a fluorescence decay curve. In this document, a fluorescence decay curve may also be referred to as a waveform to emphasize the generality of the measurement for data analyses.

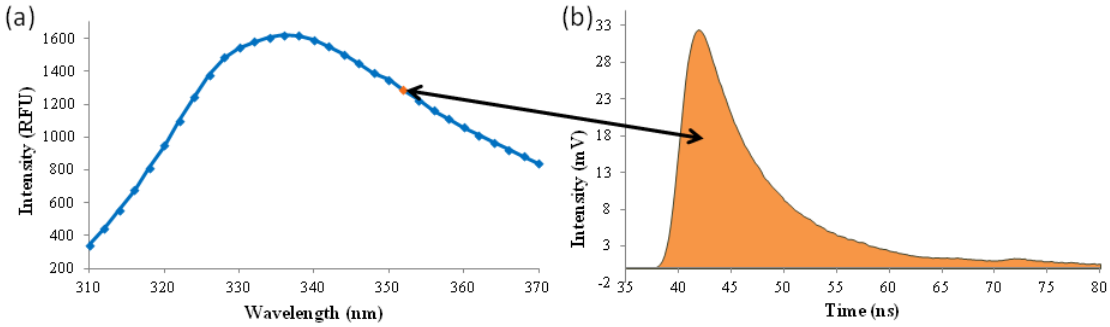

Figure 2.3: Schematic emphasizing (a) steady state fluorescence as the integral of (b) time-resolved fluorescence.

FL is sensitive to alterations in the environment directly surrounding the fluorophore and can be used as a readout to monitor protein binding, reaction kinetics (*in vitro*[48] and *in vivo*[49]) and structural changes. Excited molecules return to the ground state by either radiative or non-radiative pathways. Non-radiative pathways include energy transfer to the surrounding medium through physical and non-physical means. The fluorescence lifetime (τ) depends on rates of both radiative (Γ) and non-radiative (k_{nr}) processes (Equation 1).

$$\tau = \frac{1}{\Gamma + k_{nr}} \tag{1}$$

Electron relaxation from an excited state back to the ground state is a random event; therefore depopulation of the excited state can be defined by Equation 2,

$$\frac{-dn(t)}{dt} = (\Gamma + k_{nr}) n_0 e^{-t/\tau} \tag{2}$$

where $n(t)$ is the number of molecules in the excited state at time t, and n_0 is the total number of molecules excited (number of molecules excited at $t = 0$). The intensity observed can be written as

$$I(t) = I_0 e^{-t/\tau} \tag{3}$$

Equation 3 assumes that all molecules are excited at the same instant (i.e., infinitesimally sharp excitation pulse). Since this is not the case, the width of the excitation laser pulse must be integrated into the fitting parameters to accurately determine lifetime. As shown pictorially in Figure 2.4 below, the measured fluorescence decay curve, $N(t_k)$, is the convolution integral of the instrument response function and fluorescence decay signal. The laser pulse can be represented as a series of infinitesimally sharp excitation events (orange lines, bottom graph), each exciting a

population of fluorophores proportional to the signal strength. The top figure demonstrates this for a laser profile modeled by three sharp excitation pulses occurring at times k = 1, k = 2 and k = 3. The first and third pulses are of lower intensity compared to the second pulse. The total intensity measured (green line, $N(t_k)$) after the first pulse represents the decay of a relatively small population of fluorophores. The second pulse, at time k = 2 pushes a larger population of molecules into the excited state and the observed signal becomes the additive emission from molecules excited by both k = 1 and k = 2 excitation events. Finally, the third excitation pulse promotes a smaller population of fluorophores (relative to pulse at k = 2) into the excited state which then emit. Because the third excitation pulse is less in intensity, the measured signal increase is less than the signal increase observed following the second excitation pulse. To resolve the laser profile and fit the fluorescence signal to a sum of exponentials, a mathematical process known as iterative deconvolution is done.

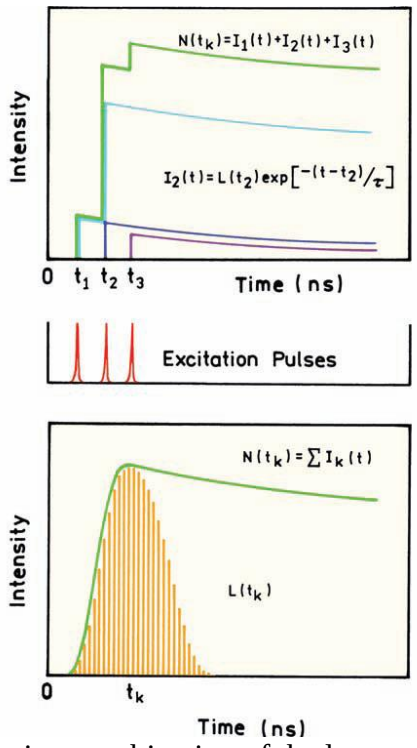

Figure 2.4. Fluorescence data is a combination of the laser pulse profile and fluorescence emission.[50] The measured time dependent intensity, as a result of three infinitesimally narrow excitation pulses at times t_1, t_2 and t_3, is shown in the top figure. Similarly, the measured fluorescence intensity profile as a function of time, $N(t_k)$, is the additive signal from many excitation pulses and the resulting emission from all pulses.

The laser profile (a.k.a., instrument response function, IRF) can be measured directly using a non-fluorescent scattering sample, such as glycogen or silicon beads, or by measuring the Raman scatter of the solvent. Analysis of lifetime data collected in this thesis used primarily Raman scattering of a water sample as an IRF in the deconvolution process.

Development of Fluorescence Instrumentation to Meet High-Throughput Demands

Due to rapidly growing compound libraries (theoretically ~100 million compounds)[51] and therapeutic targets, the current state of drug development necessitates

high-throughput to accelerate formulation. According to a recent review by McGregor and Hornig, "HTP (high throughput) technology…is crucial for the identification and validation of novel drug targets and next-generation antivirals."[52] This need has shifted instrumentation to microfluidic and microplate formats, reducing time and sample requirements. Fluorescence lifetime is inherently more robust compared to fluorescence intensity. Fluorescence lifetime is independent of concentration (assuming no change in state with increasing concentration), volume, slit width, and unaffected by inner filter effects or laser power fluctuations. These characteristics help reduce false readouts in assays. Currently available microplate fluorimeters advertising time-resolved capabilities (Infinite® 200 PRO, PHERAstar® *FS*, SpectraMax Paradigm Multi-Mode Microplate Reader) only offer microsecond lifetime acquisition. This is in part due to the incompatible collection times of nanosecond time resolved instrumentation currently available.

The most common technique for acquiring time-resolved data on a nanosecond time scale is time-correlated single photon counting (TCSPC). TCSPC measures the fluorescence decay by determining the time between excitation and detection of the first emitted photon, then counts the number of photons detected for specified time intervals. A histogram of the number of photons counted is built as shown in Figure 2.5, eventually arriving at the final decay curve.[53] To ensure detection of a single photon, the excitation pulse energy is kept low, typically less than 1 nJ. Due to the statistics of random emission, TCSPC experiments record 10,000 counts in the peak channel corresponding to a noise level of approximately 1%.[53] To collect this number of photons quickly, the pulse

repetition frequency (PRF) of the laser must be high, on the order of 10^6 Hz. However, acquisition times for the fastest TCSPC systems still remain outside the limits for high-throughput applications.

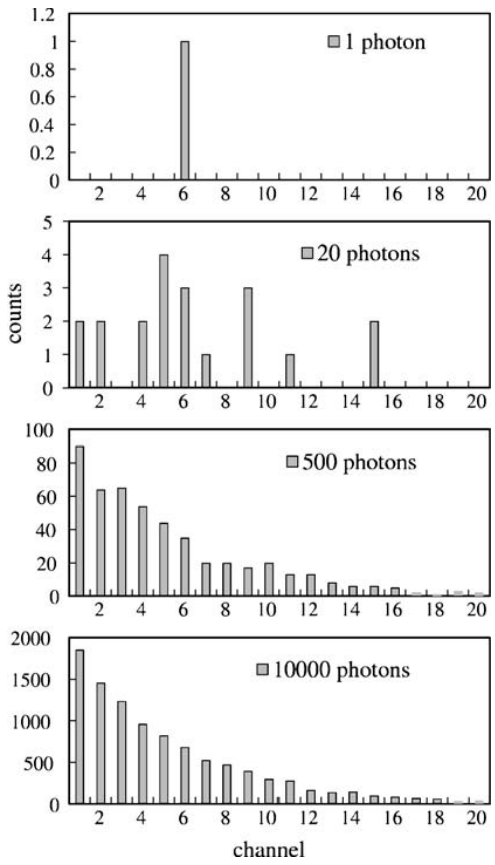

Figure 2.5: Histograms representing the build-up of the TCSPC emission decay curve after 1, 20, 500 and 10,000 photon events. [53]

Direct time-resolved measurements or direct waveform recording (DWR) is probably the most direct approach to collecting decay information. This method uses a transient recorder which stores the input from the PMT for digitization.[53] The time resolution is limited to the capabilities of the photodetector and transient recorder, typically in the nanosecond range. However, for almost all biological and biochemical

applications, this is adequate. Fluorescence Innovations, Inc. (FII) has developed proprietary digitization technology capable of acquiring accurate (0.5%) and precise (1%) direct time-resolved fluorescence lifetime data in 0.1 ms.[54] The high precision is a consequence of recording thousands of photons for every laser pulse. A detailed description of the cuvette-based instrument design, components and comparative study to TCSPC method can be found in reference 54.

The collection times of FII's technology make it the only nanosecond time-resolved instrument on the market compatible for high-throughput, microplate formats. This first section will detail the changes made to FII's prototype cuvette instrument to microplate format and the characterization/validation of these instruments.

Design of Nova Fluor FLS Plate Readers

Two fluorescence lifetime spectrophotometers (Vis NovaFluor and UV NovaFluor) were designed to utilize FII's technology. Because this technique is not limited to counting single photons, lower repetition frequencies and more powerful lasers can be used, resulting in more emitted photons, better photon statistics and shorter collection times. Both instruments implemented similar design schemes (Figure 2.6), differences being excitation laser sources and emission wavelength selection.

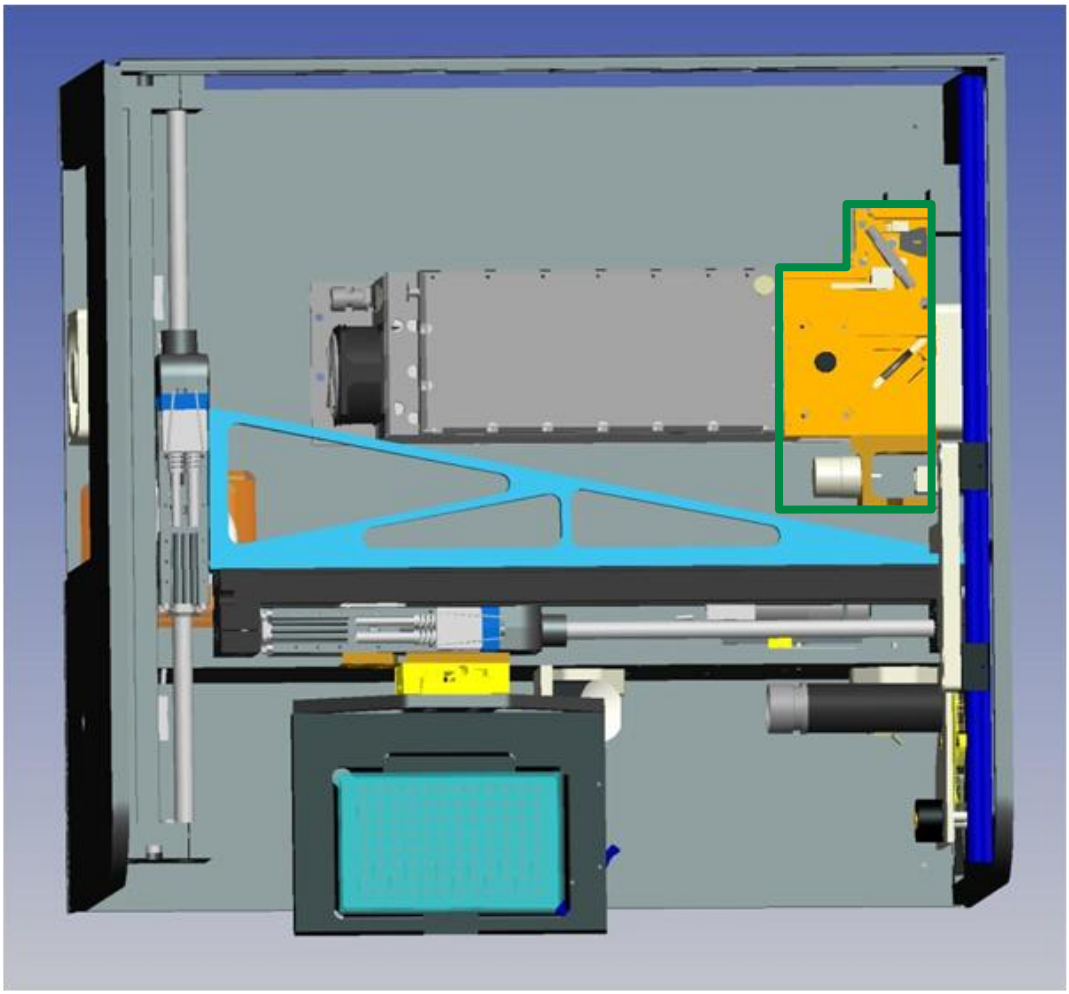

Figure 2.6: Diagram of NovaFluor FLS plate readers. Dye flow cell outlined in green is specific to the UV NovaFluor. Detection module not shown.

The Vis NovaFluor system contains two passively Q-switched microchip lasers producing 355/532nm (Teem photonics) and 473 nm (Concepts Research Corporation, model) excitation. Passively Q-switched lasers eliminate electromagnetic noise that would otherwise disrupt detection electronics. [54] Highly uniform pulses created by these lasers (1 ns full width at half maximum, ≤3% pulse-to-pulse deviation) contribute to extraordinarily high data precision and eliminate the otherwise necessary IRF collection between samples. The emitted light is collected with an off-axis parabolic mirror

(Newport). The appropriate filter (532, 365 and 473 nm long pass filters, Semrock) can be secured to the lens tube to remove any scattered light. A six position filter wheel containing 5 bandpass filters provides emission selection and subsequent photodetection by a PMT (Hamamatsu). The second instrument, UV NovaFluor, contains a high power (>20 μJ) 532 nm passively Q-switched laser (Teem photonics, model PNG-002025) that acts as a pump for a pyrromethane dye (600 μM in ethanol) to create a 560-610 nm lasing output. The output is selected via rotation of a tunable bandpass filter (Semrock), and subsequently passed through a doubling crystal to produce 285-310 nm excitation (1 μJ/pulse). Emitted light is again collected with an off-axis parabolic mirror and directed to a monochromator for emission selection.

Collection Modes. Several types of data can be collected on this instrument. Each measurement is represented by a three letter acronym. The two terminal letters of almost all measurement acronyms are TM, representing Time Matrix. This naming was derived from the measured data matrix which always contains the fluorescence intensity as a function of time (fluorescence decay curve) in one dimension. The first letter represents the 'other variable' which can be emission wavelength, excitation wavelength, sample, time (longer time scale, typically seconds), polarization, attenuation, temperature, etc. Text files containing data are set up to record all parameter settings as shown in Figure 2.7. A definition of each collection acronym is given in Appendix 1.

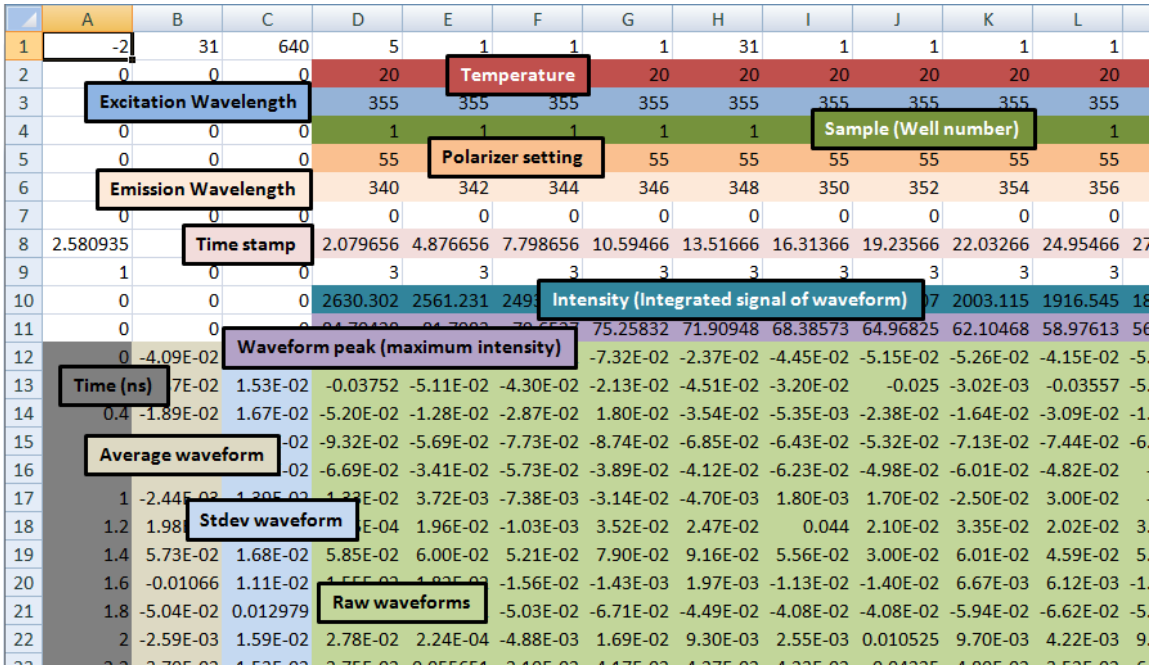

Figure 2.7: Labeled data matrix for data collected using NovaFluor instruments.

Instrument Calibration and Validation

Fluorescence is one of the most common reporters available to researchers, not only in chemistry but biology and biomedical science. High sensitivity makes fluorescence a valuable indicator of cell membrane, protein and DNA processes and a driving force for optical imaging advances.[55] Fluorescence has even been used to visualize tumors in live mice.[56] The chemical information reported by a fluorescent probe is observed and evaluated through changes in fluorescence intensity or quantum yield, shifts in emission spectra, and alterations in decay kinetics (or lifetime). The measurement of fluorescence lifetime and intensity data rely on the response of detection electronics and compatible optics. As well stated by Zenger *et al.*, "objective methods to assess the quality of data obtained by (fluorescence) measurements are critically

important to research scientists, clinical laboratory personnel, and regulatory reviewers."[57] The fluorescence signal is sensitive to both environmental stimuli (sample content) and instrumental factors (efficiency/sensitivity of electronics and optics). Evaluation of instrument inconsistencies come by way of universal standardization procedures for fluorescence instrumentation.[57,58] The fluorescence lifetime plate readers introduced in the previous section were validated using techniques recommended by the American Society for Testing and Materials (ASTM) and inferred from reference 59. The following are results of this validation process.

Wavelength Accuracy and Spectral Responsivity

Collection of absolute emission spectra is a challenge due to the distortion caused by both instrumental factors (transmission efficiency and polarization sensitivity of the monochromator, mirror reflectivity, and PMT sensitivity) and sample-related effects (such as inner filter effects and competing absorption). The minimum correction required to compare emission spectra collected on different instruments corrects only for instrumental factors distorting spectra. Methods of determining instrumental correction factors include using an irradiation standard with known spectral distribution (such as a tungsten-halogen lamp) or quantum counters. Since this equipment is typically unavailable, the most common method to correct emission spectra is to collect spectra using secondary emission standards and compare this to literature reported values. Secondary emission standards include (but are not limited to) laser dyes and inorganic dyes imbedded in a solid substrate.[60]

Emission spectra of fluorescein and 9,10-diphenylantrhacene (DPA) were measured and compared to reference spectra[61] to determine the spectral responsivity of NovaFluor detection optics. Fluorescein (3.8 mg, 10.1μmol) was dissolved in 5 mL 0.1 M NaOH, then diluted 1:1000 for a 2 μM stock solution. Similarly, DPA (1.5 mg, 4.5μmol) was dissolved in 3 mL benzene and diluted 1:1000 to produce a 1.5 μM stock solution. Fluorescence emission scans on solvents were recorded prior to solution preparation to check for possible fluorescent contaminations. Stock dye solutions (150 μL) were diluted with an equal volume of solvent and scanned (295nm excitation, 400 V PMT gain, 1 second signal averaging[190 shots], 300-650 nm emission). Final dye concentrations were 1 and 0.7 μM for fluorescein and DPA, respectively.

Overall, the monochromator appears to be well calibrated, with peaks of both dyes corresponding to that reported (Figure 2.8). The slight variation observed for DPA spectra could be a result of oxygen quenching (samples were not degassed). The detector response was slightly lower for wavelengths longer than roughly 550 nm. A majority of measurements on the UV-NovaFluor will be made at wavelengths below 400 nm. In fact, the only data collected on this instrument at wavelengths longer than 400 nm thus far are reported here. Therefore, the need to integrate a correction factor into the software did not merit the time required to do so.

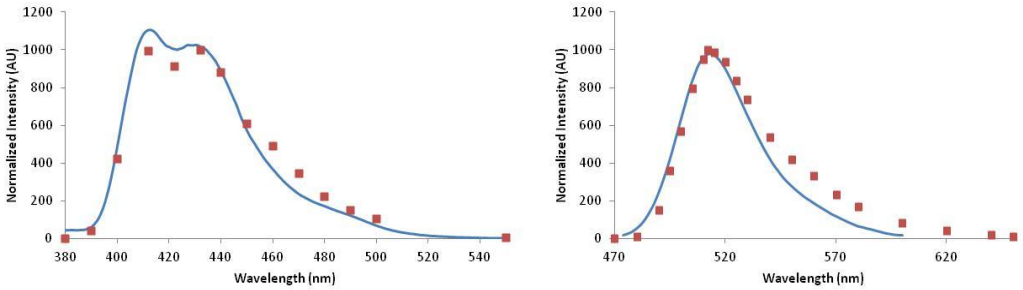

Figure 2.8: Normalized emission spectra of DPA in benzene and fluorescein in 0.1M NaOH for UV Nova Fluor (blue line) and reference corrected spectra[61] (red squares).

Detection System

Linearity and Limits of Detection

The linearity of each instrument was determined by measuring the fluorescence signal produced at different concentrations of fluorophore. Two of the fluorophores selected, p-terphenyl (PTP) and Rhodamine 6G (R6G), were standard dyes possessing the following recommended characteristics: (1) responsive and stable at the selected excitation wavelength, (2) large quantum yield independent of concentration, (3) and broad emission spectra.[62] The third sample tested was the protein standard bovine serum albumin (BSA). It was chosen as the representative protein sample simply due to its availability and stability. Fluorescence intensities for R6G, BSA and PTP are shown as a function of concentration on both linear and log scales (Figure 2.9). Intensity was calculated as the integral of the fluorescence decay curve from 0-90 ns.

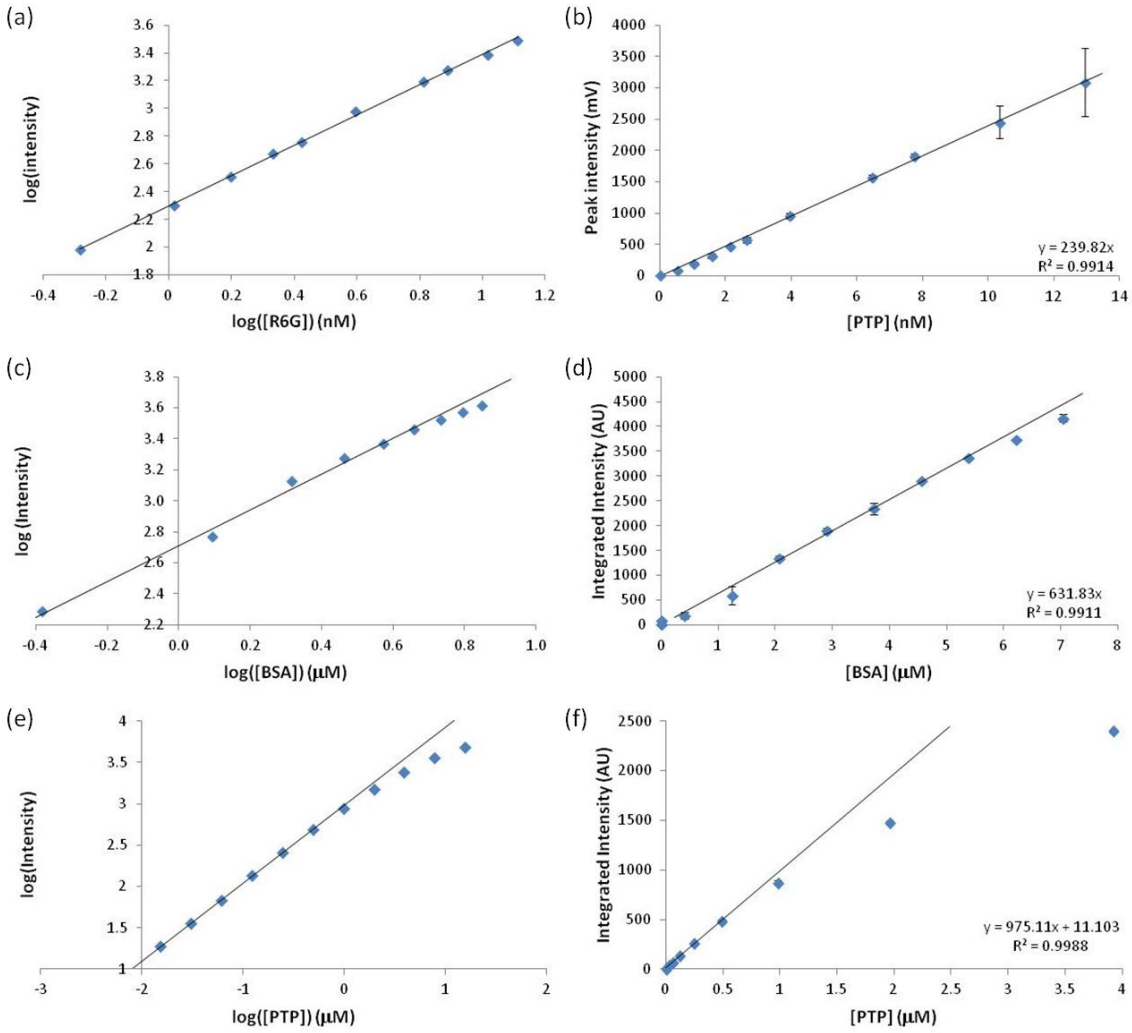

Figure 2.9: Fluorescence intensity of varying concentrations of R6G (a-b) collected on the Vis NovaFluor, and BSA (c-d) and PTP (e-f) collected on UV Nova Fluor, respectively. (a), (c), (e) log scale; (b), (d), (f) linear scale.

The upper limit of linearity was defined as the upper point that deviated more than 5% from the straight line fit. The integrated signal shown in Figure 2.9 appears to be linear for Vis NovaFluor at the range tested (i.e., an upper limit could not be determined with this data set). Greater variability was observed for signals exceeding 80 mV at the peak (Figure 2.9, b). This could be a result of pipetting errors, reflecting the sensitivity of intensity measurements to changes in the volume or path length. Deviation from linearity

was observed for the UV NovaFluor instrument for sample concentrations exceeding 6.2 μM BSA and 1 μM PTP.

The limit of detection (or lower limit of linearity) was determined as the concentration where the signal deviates by more than twofold from the average percent deviation (as determined by the middle five data points). Lower limits of detection were determined to be 1.2 μM BSA, 30 nM PTP for the UV NovaFluor instrument. The visible system had higher sensitivity due to the use of bandpass filters in place of a monochromator. Bandpass filters transmit between 87-95% of incident light depending on wavelength compared to 30-50% efficiency of a typical monochromator. The lower limit of detection of the Vis NovaFluor was determined to be 2.6 nM R6G. The average straight line deviations for each fluorophore were 3.4%, 4.9% and 1.9% for R6G, PTP and BSA, respectively.

Time-resolved data is expected to maintain shape regardless of concentration or signal magnitude. This was verified by directly comparing the overlap of area normalized waveforms (Figure 2.10), and by iterative reconvolution to determine lifetimes (Figure 2.11). Deformation of time-resolved data was not observed for either Vis-NovaFluor or UV-NovaFluor data with peak amplitudes between 7-80 mV and 5-45 mV, respectively. Negligible differences of first moment and lifetime values (iterative reconvolution with Raman scatter IRF) further support the lack of distortion with increasing signal (Table 2.1). BSA required a bi-exponential fit as expected for the fluorescence decay curve of tryptophan containing protein. This was reduced to the

average lifetime (Equation 4) which was within the range of literature reported data (6.05 ns[63] and 6.77 ns[64]).

$$< \tau >= \sum_{i=1}^{i} \frac{\alpha_i \tau_i^2}{\alpha_i \tau_i} \quad (4)$$

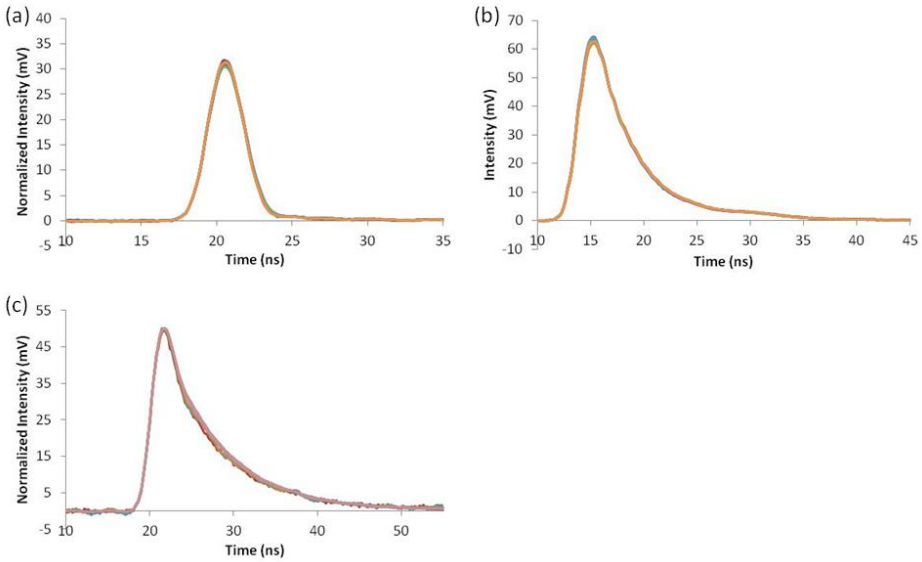

Figure 2.10. Normalized waveforms of varying amplitudes for (a) PTP, 4-35 mV, (b) R6G, 7-91 mV, and (c) BSA, 4-45 mV.

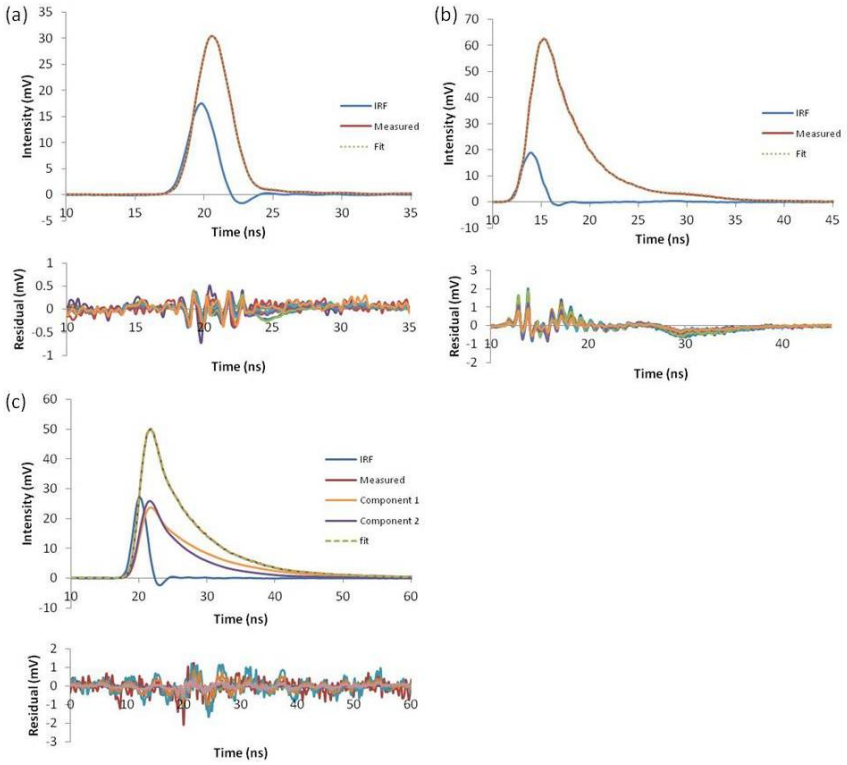

Figure 2.11. Sample fits and residuals for iterative reconvolution of fluorescence decay spectra. (a) PTP (12 waveforms, 60-980 nM), (b) R6G (12 waveforms, 1-10.4 nM) and (c) BSA (8 waveforms, 0.4-2.9 μM).

Table 2.1. Lifetimes for R6G, PTP and BSA decay curves (data represents average of duplicate or triplicate samples). Single exponential functions sufficiently fit R6G and PTP waveforms. A biexponential fit was required for BSA. The value reported is the weighted average lifetime (equation 4).

[R6G] (μM)	Avg τ ± σ (RSD)
1	3.94 ± 0.06 ns (1.5%)
0.80	3.87 ± 0.13 ns (3.2%)
0.60	3.96 ± 0.02 ns (0.5%)
0.50	3.90 ± 0.08 ns (2.0%)
0.40	3.88 ± 0.05 ns (1.3%)
0.30	3.91 ± 0.04 ns (1.0%)
0.20	3.92 ± 0.04 ns (1.0%)
0.17	3.90 ± 0.02 ns (0.5%)
0.12	3.86 ± 0.10 ns (2.7%)
0.08	3.88 ± 0.08 ns (2.1%)
0.04	3.84 ± 0.01 ns (0.30%)
Overall (0.08-0.80)	**3.90 ± 0.07 ns (1.70%)**

[PTP] (μM)	Avg τ ± σ (RSD)
15.7	NA
7.8	NA
3.9	NA
2.0	1.29 ±0.22 ns (17%)
1.0	1.19 ±0.15 ns (17%)
0.49	1.18 ±0.005 ns (0.45%)
0.25	1.12 ±0.008 ns (0.76%)
0.12	1.08 ±0.006 ns (0.51%)
0.061	1.07 ±0.048 ns (4.48%)
0.03	1.18 ±0.005 ns (0.45%)
0.015	NA
Overall (0.08-0.80)	**1.10 ±0.05 ns (4.11%)**

[BSA] (μM)	Avg $\langle\tau\rangle^*$ ± σ (RSD)
0.4	6.66 ± 0.07 ns (1.0%)
1.2	6.55 ± 0.13 ns (2.0%)
2.1	6.56 ± 0.03 ns (0.4%)
2.9	6.57 ± 0.01 ns (0.2%)
3.7	6.65 ± 0.11 ns (1.7%)
4.6	6.75 ± 0.001 ns (0.02%)
5.4	6.82 ± 0.0008 ns (0.01%)
6.2	6.89 ± 0.0002 ns (0.003%)
7.0	6.93 ± 0.03 ns (0.4%)
Overall (1.2-3.7 μM)	**6.58 ± 0.08 ns (1.5%)**

Experimental. Stock Rhodamine 6G (R6G, 7.1 μM) was prepared by dissolving an arbitrary amount in water. The absorbance at 530 nm of a 5x dilution was measured to determine the concentration (A_{530} = 0.14, ε = 116,000 $M^{-1}cm^{-1}$). This sample was diluted further such that a 300 μL sample (approximately 0.4 μm path length) produced a signal close to 100 mV at 532 nm excitation, 610 nm emission (20 nm band pass). Samples were prepared according to Table 2.2, weighed after each addition, and then transferred to a quartz microplate (300 μL × 3 samples).

Table 2.2 Sample preparation and weight data for Vis NovaFluor linearity experiment.

Well	Volume water (mL)	Volume R6G (mL)	Weight water (g)	Weight R6G solution (g)	Weight % (v/v) [R6G]
1, 13, 25	0	1.5	NA	NA	100
2, 14, 26	0.30	1.2	0.30	1.213	80
3, 15, 27	0.60	900	0.609	0.908	60
4, 16, 28	0.75	750	0.759	.757	50
5, 17, 29	0.90	600	0.908	0.608	40
6, 18, 30	1.0	500	1.058	0.463	30
7, 19, 31	1.2	300	1.200	0.309	20
8, 20, 32	1.25	0.25	1.249	0.247	17
9, 21, 33	1.3	0.20	1.322	0.183	12
10, 22, 34	1.4	0.10	1.384	0.121	8
11, 23, 35	1.45	0.05	1.459	0.061	4
12, 24, 36	1.5	0	NA	NA	0

Scans were recorded using 0.50 s averaging (100 laser pulses), 400 V gain setting for the photomultiplier tube (PMT), 500 mV digitizer range, 532 nm excitation and 610 nm emission. Water Raman was collected at 556 nm emission (20 nm bandpass) without either polarizer or 532 nm cutoff scatter filter. Curves were compared by normalization,

moment analysis and iterative reconvolution using the Raman scattering as an instrument response function.

A stock solution of PTP (157 μM) was diluted 10 fold with ethanol in a quartz microplate. Successive dilutions (two fold) were repeated in 11 adjacent wells providing concentrations of 15.7, 7.8, 3.9, 2.0, 1.0, 0.49, 0.25, 0.12, 0.061, 0.031, and 0.015 μM. Fluorescence decay curves were recorded with UV NovaFluor at 295nm excitation, 350 nm emission, 1.05 s sample averaging (200 shot) and 400 V PMT gain.

Stock BSA (A_{280} = 0.73, ε = 43,000 $M^{-1}cm^{-1}$, 17 μM) was dissolved in Aquafina water then diluted according to Table 2.3 (duplicate samples). Waveforms were acquired at identical settings as for PTP. Seven scans were recorded at varying excitation attenuation (iris adjustment) to produce roughly 50 mV peak amplitude for BSA samples between 2.1-7.0 μM (data shown in repeatability section).

Table 2.3: Volumes used and corresponding concentration of BSA.

Well	**Volume H_2O (μL)**	**Volume BSA solution (μL)**	**[BSA] (μM)**
1, 13	200	0	0
2, 14	200 (PBS)	0	0
3, 15	200	5	0.4
4, 16	190	15	1.2
5, 17	180	25	2.1
6, 18	170	35	2.9
7, 19	160	45	3.7
8, 20	150	55	4.6
9, 21	140	65	5.4
10, 22	130	75	6.2
11, 23	120	85	7.0
12, 24	0	0	0

Solvent scans were recorded under identical instrument settings to experimental data prior to adding sample. This was done to verify cleanliness of microplate and solvent.

Reproducibility

Assessment of data reproducibility provides confidence that any observed changes are a direct result of the experimental variable being tested. The repeatability of the NovaFluor instruments was evaluated through three separate experiments.

Day-to-day repeatability was evaluated through collection of water Raman decay curves collected randomly over 13 months then compared to verify the excitation pulse width stability of the UV NovaFluor. These waveforms varied in intensity due to adjustment of an iris preceding the parabolic mirror (refer to Figure 2.6 for instrument diagram). A significant time shift (0.5 ns) was observed for the water Raman signal collected April 2013 (unshifted data not shown) which was due to adjustment and recalibration of the tuning mechanism and doubling crystal. Therefore, waveforms underwent a waveform overlap procedure to compare the shape of Raman signals. This procedure matched waveform amplitudes and shifted waveforms in time to provide maximal overlap. The results of this overlap are shown in Figure 2.12. Excellent stability was observed for the pulse width over long periods of time.

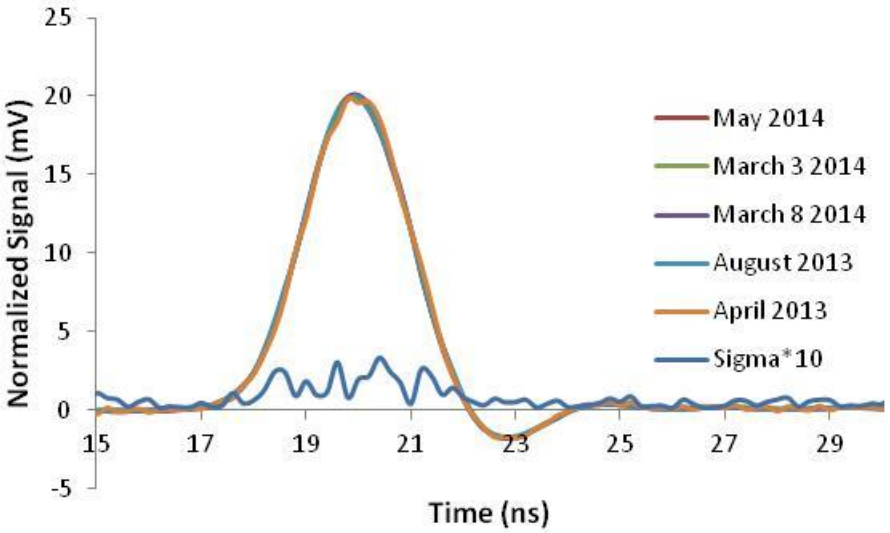

Figure 2.12. Normalized and time shifted Raman waveforms for 5 water samples collected over a 13 month time period. The standard deviation has been scaled by a factor of 10.

The sample-to-sample repeatability was tested for both UV and Vis NovaFluor systems using reference solutions. For the Vis NovaFluor, eleven samples of rhodamine B (RB), anthracene, and coumarin 480 (C480) were scanned using the 532 nm, 355 nm and 473 nm laser sources, respectively. Emission was collected through the 610, 438 and 500 nm bandpass filters for RB, anthracene and C480, respectively. The PMT gain was set to 400 V, and 1.05 s (200 shot) waveform averaging was used. The same waveform overlap procedure used to evaluate the water Raman shape was applied to compare waveforms for RB, anthracene, and coumarin 480. Waveforms for each dye were found to be identical with high precision (Figure 2.13).

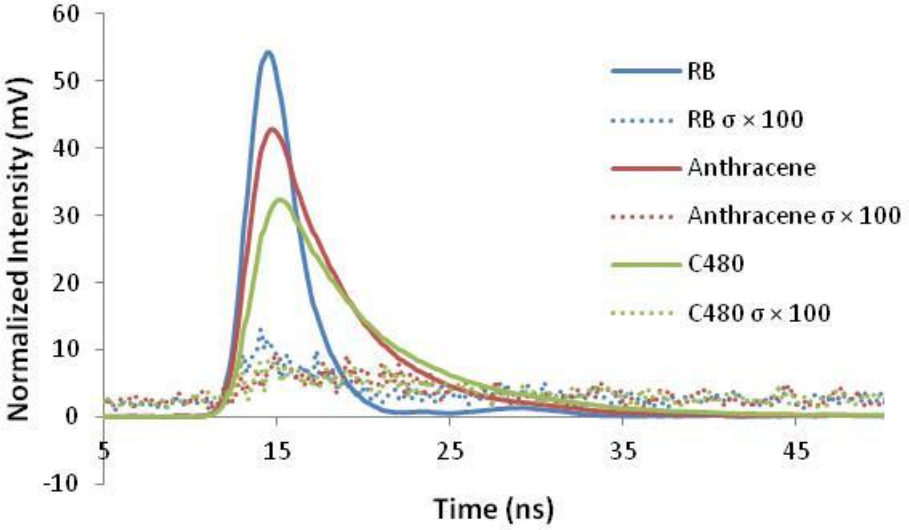

Figure 2.13. Average (solid line) and standard deviation (dashed line, scaled 100 fold) of overlapped waveforms for RB (blue), anthracene (red), and C480 (green).

The UV NovaFluor repeatability was evaluated using eight of the waveforms collected for the linearity study (0.4 mM-6.2mM, duplicate samples). BSA was excited at 295 nm the resulting emission at 340 nm was evaluated. Fluorescence decay curves of BSA collected on the UV NovaFluor were normalized such that the integrated area under each waveform was equal. These waveforms were also highly repeatable. The average relative standard deviation of BSA decay curves at 8 different concentrations (duplicate samples) was 0.74% for t=18-40ns (Figure 2.14).

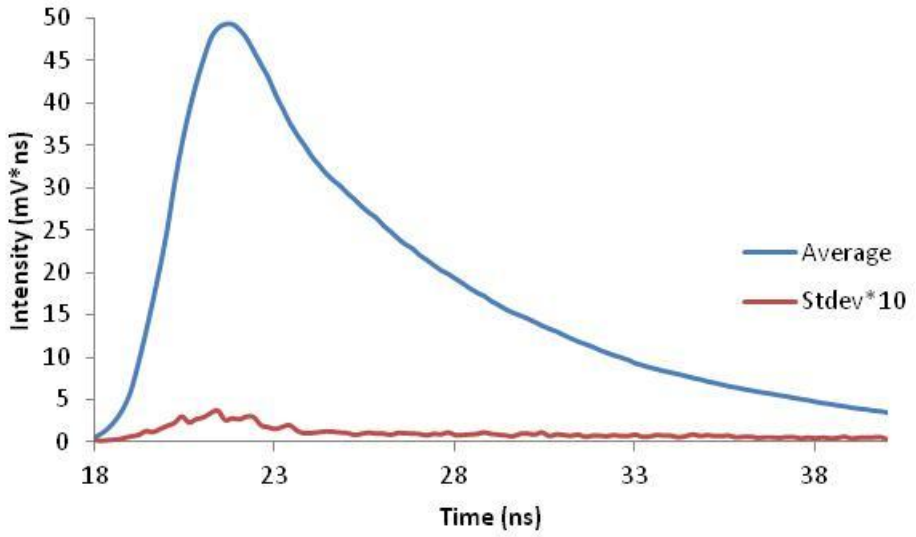

Figure 2.14: Average (blue) and standard deviation (scaled 10 fold, red) of BSA waveforms (15 decay curves, 8 concentrations).

The waveform comparisons performed above demonstrate the excellent precision and stability of the NovaFluor instruments (Figures 2.12-2.14). This high precision is comparable to the precision observed for cuvette based instruments equipped with the same technology (Figure S11 of reference 48). This suggests conversion to a microplate format did not adversely affect the acquired data.

Fluorescence Lifetime Standards

The accuracy of time-resolved fluorescence measurements was evaluated through comparison of the deconvoluted lifetime values with those reported in the literature for eight reference dyes. Recommended reference dyes have the characteristics of large Stokes shifts and quantum yields to avoid problematic interferences such as self quenching and intermolecular interactions.[65] They are readily available in high purity and soluble in common, high grade solvents. A majority of the dyes selected for this study

meet these criteria with the exception of D L-tryptophan, which was selected because it is the primary, intrinsic fluorophore of proteins. Table 2.4 provides the solvent used, the appropriate excitation and emission wavelengths range, and literature reported lifetimes for each fluorophore.

Table 2.4. Calculated lifetimes for reference dyes.

Dye	Solvent	Excitation/Emission Wavelength (nm)	Lifetime, Literature (ns)	Ref	Lifetime, measured (ns)
Anthracene	Methanol	295-360/375-442	5.1±0.3	65	3.90±0.01ǂ
	Ethanol		4.21±0.02	59	3.99±0.01ǂ
Fluorescein	0.1M NaOH	495/517	4.16	66	4.06±0.07
Coumarin 480	Methanol	390/407-473	τ_1=5.50 ± 0.01 τ_2=0.02 ± 0.004	67	τ_1=5.60 ± 0.02 τ_2=0.04 ± 0.02
DPA	Methanol	355/430	8.7±0.5	65	5.88±0.04ǂ
Rhodamine B	Water	532/590	1.74±0.02	65	1.74±.01†
			1.68±0.1	68	
R6G	Water	525/555	4.08±0.1	68	4.06±0.05
			3.8± 0.45	69	
PTP	Methanol	295/336	1.17±0.08	65	1.26±0.01
	Ethanol		1.05	59	1.11±0.05
D L-tryptophan	Water	295/350	3.3	70	τ_1=0.03 ± 0.02 τ_2=3.24±0.05

ǂQuenched by molecular oxygen (sample were not de-gassed).
†Reconvolution required biexponential fit (τ_2 = 0.57 ± 0.03 ns)

As shown in Table 2.4, determined lifetimes for fluorescein, rhodamine B, R6G, PTP and D L-tryptophan are all consistent with published data.

Anthracene and DPA both had significantly shorter than expected lifetimes. These fluorophores are highly susceptible to oxygen quenching and samples were not degassed. This is most likely the source of the reduced lifetimes.

The biexponential fit necessary for rhodamine B is most likely an artifact of the IRF. Reconvolution with a Rayleigh scatter IRF collected at a later time provided a good single exponential fit (1.72 ± 0.01 ns) but required a time shift of 0.08 ns.

The short component of the Coumarin 480 decay curve correlated with that reported but the long lifetime component was slightly longer. The cause of this is currently unknown. Coumarins are highly sensitive to their environment, which makes them excellent chemical sensors.[71] It is possible that a trace amount of another solvent, for example water, was present in the well into which C480 was loaded, and is responsible for the lifetime difference.

The experimental lifetime of the major component of the tryptophan fluorescence (τ_2 = 3.24 ns) is consistent with the literature reported data. A second exponential was required for a good fit which could be a result of a possible contaminant, an inaccurate IRF, or, due to the absence of an emission polarizer in the UV NovaFluor. The emission polarizer, when set to the appropriate angle removes rotational bias of the fluorescence emission. Rotational bias is a consequence of preferential excitation of molecules with absorption dipoles aligned with the electric vector of the exciting light. This means that the fluorophores able to absorb light are similarly oriented. Molecules free in solution are able to rotate during the period between excitation and emission, meaning that the resulting emission may not have identical orientation as the incident light. Photodetectors are sensitive to the changes in light polarization and will tend to favor one orientation. The bias of photodetectors combined with the changes in the orientation of the fluorophore result in slight shifts in the measured fluorescence decay.

Analyzing Fluorescence Lifetime Data

One significant problem with time-resolved data comes in the reduction of decay curves to a set of parameters. There is a need to select enough parameters to provide an adequate fit; however, fitting exponentials to too many parameters results in less precise measurements. (This is not limited to fluorescence decay curves, but rather applies to all exponential functions.) As a response, alternative methods that involve treating the decay curve as a spectrum have been developed.

The spectrum approach requires more sophisticated data processing, but mathematical algorithms to analyze spectral data for the purpose of mixture analysis are well known. Spectral analyses, where all data points are used in the fitting, originated in chemometrics but are increasingly being used in spectroscopy.[72, 73] Spectral analyses processes are variously referred to as spectral decomposition[74], spectral deconvolution[75], spectral unmixing[76], multivariate curve resolution, etc. The choice of name depends in part on the intended use of the data. Which procedure is most effective may depend on the data quality. In many cases, the signal changes can be modeled using a weighted linear combinations of pure responses, as discussed in chapter 3.[73] The procedures could be applied to a variety of spectral data including Raman, absorbance, excitation, emission and, in this case, the decay spectra.

Conventionally, time-resolved fluorescence is deconvoluted to a set of amplitude factors and fluorescence decay times. These lifetimes can then be modeled to characterize the biological or chemical process that is occurring. This method of analysis is complicated, and sometimes the link between the reaction (or interaction) and

fluorescence lifetime is not fully understood. The reason for multiple lifetimes of tryptophan containing proteins, for example has been[77] and continues to be a topic of debate.[78] The high precision of NovaFluor technology permits treatment of the fluorescence decay as a spectrum, similar to an emission spectra/wavelength-intensity spectrum. This reduces the noise because it relies on the shape of the curve, which is a molecular property.

Summary

Fluorescence lifetime spectroscopy offers a versatile platform for evaluating molecular interactions. A combination of lifetime, intensity and polarization data has the potential to report on binding, size and relative distances (referring to FRET which was not discussed but a possible measurement). The need to properly calibrate new fluorescence based instrumentation is validation necessary to rely on data acquired by the system. Validation experiments of the UV and Vis NovaFluor plate readers show there excellent linear response and no waveform distortion was observed as a result in either electronics or optics.

CHAPTER 3

APPLICATIONS OF FLUORESCENCE LIFETIME SPECTROSCOPY

Introduction and General Considerations in Experimental Design

The following summarizes analysis techniques and equations used in the treatment of fluorescence decay curves as spectra for various applications. Specifically, this chapter discusses their use in determining binding constants, kinetic rates of reactions, and thermodynamic stability. This treatment prevents the need for deconvolution. These analyses rely on the ability to define physical states of the system by the observed lifetime and are dependent on the distinct lifetimes that exist for each physical state. Decay curves, or waveforms, can be defined as a linear combination of "state" or "basis" waveforms when this criterion is met. This is shown for two hypothetical states, X and Y, each represented by distinct waveforms W_X and W_Y, respectively (equation 5). In this case, the population of each state is determined by the variable i, and determined by the coefficients $f_{x,i}$ and $f_{y,i}$. i can represent ligand concentration, time, temperature, denaturant concentration, etc.

$$W_i = f_{X,i}W_X + f_{Y,i}W_Y \tag{5}$$

Application 1:Protein-Ligand Binding Constant Determination

Assuming that there only exists, on average, a single free and bound form of an intrinsically fluorescent or fluorescently labeled protein, the observed waveform can be described as the linear combination of waveforms characteristic to each form.

$$W_i = W_f f_{f,i} + W_b f_{b,i} \tag{6}$$

Here W_f, W_b and W_i represent the waveform of free protein, bound protein and protein at some ligand concentration, i. The fraction of free and bound protein for a given ligand concentration, i, is represented by $f_{f,i}$ and $f_{b,i}$, respectively.

The dissociation constant and the law of mass action can relate the fraction of free and bound protein to the ligand concentration, $[L]_i$ and the dissociation constant, K_d by equations (7) and (8).

$$f_{f,i} = \frac{K_d}{K_d + [L]_i} \tag{7}$$

$$f_{b,i} = \frac{[L]_i}{K_d + [L]_i} \tag{8}$$

Substitution of (7) and (8) into (6) results in the following equation:

$$W_i = W_f \left(\frac{K_d}{K_d + [L]_i} \right) + W_b \left(\frac{[L]_i}{K_d + [L]_i} \right) \tag{9}$$

The free spectra and ligand concentrations are measured parameters. If the bound waveform is unattainable through direct measurements, data extrapolation using a modified version of equation (6) allows for simultaneous solution of K_d and W_b:

$$W_b = W_i\left(\frac{K_d + [L]_i}{[L]_i}\right) - W_f\left(\frac{K_d}{[L]_i}\right) \quad (10)$$

Data sets can be fit using equation 6 and the coefficients ascribed to the free state modeled with equation 7 to determine K_d. In both fitting techniques, a non-linear least squares approach was taken to minimize the difference between measured and theoretical data.

Monomeric Binding
of Lactose to Galecin-3

Galectin-3 is a member of the galectin family of proteins, a family characterized by their ability to bind β-galactoside sugars. Galectin-3 contains three tryptophan residues, two in its unstructured, N-terminal collagen like domain and one in the binding site of the C-terminal carbohydrate recognition domain (CRD). Given the position of the tryptophan residue (Figure 3.1) relative to incoming β-galactosides, it was reasonable to believe binding could be characterized by changes in the intrinsic fluorescence of the protein.

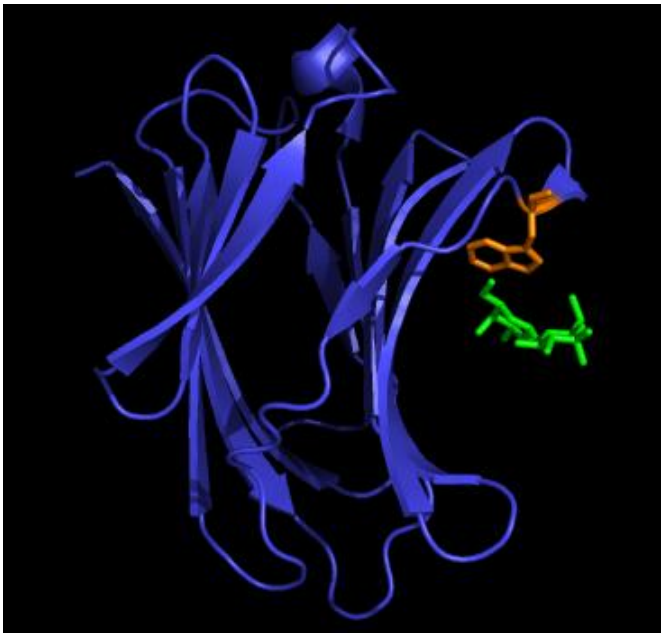

Figure 3.1. Crystal structure of galectin-3 CRD (blue) bound to lactose (green). Tryptophan residue is shown in orange. [79]

In this scenario, W_f and W_b from equation 6 above represent the waveforms of free and lactose bound galectin-3, respectively (Figure 3.2). W_i is the measured fluorescence decay curve in the presence of a given concentration of lactose, *i* and is assumed to be a linear combination of W_f and W_b. The difference between bound and free waveforms is small but significantly different given the precision of the fluorescence waveform recording technology used (as discussed in the Reproducibility section of Chapter 2).

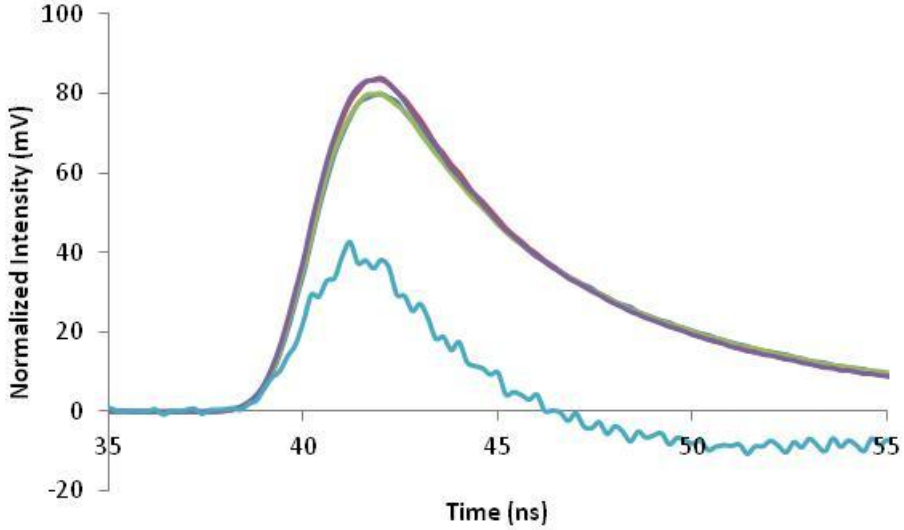

Figure 3.2. Normalized free (blue and green) and bound waveforms (red and purple) of galectin-3. The free and bound forms were averaged and the difference of these averages is shown in light blue (scaled 10 fold).

The coefficients calculated for these two data sets were fit to equation 7 to afford an average K_d of 49 ± 4 μM (Figure 3.3). The calculated K_d was slightly lower than the binding constants reported for the galectin-3/lactose interaction (0.14 mM-0.22 mM), but given the variability it seems reasonable.[6] Furthermore, shifts were observed in the emission spectra of galectin-3 upon lactose addition (data not shown) supporting that an interaction occurred.

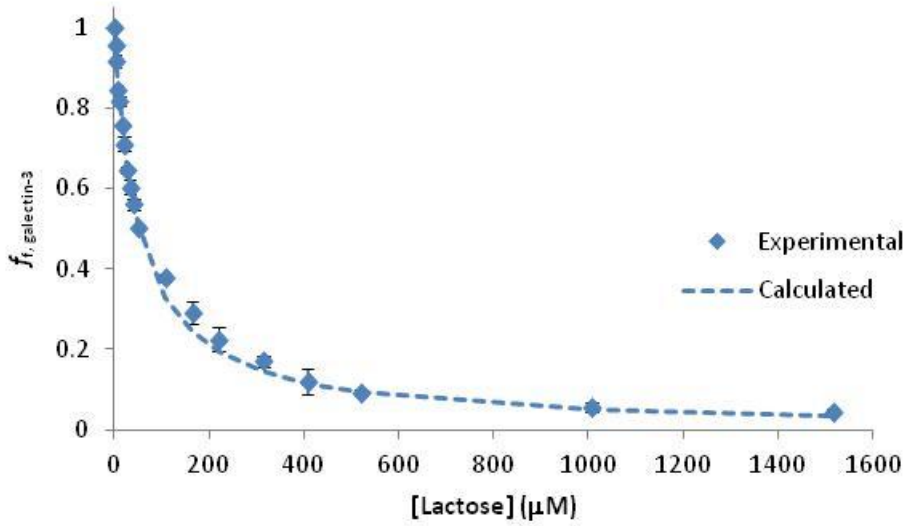

Figure 3.3. Lactose binding curve for galectin-3. The coefficient corresponding to the fraction of free galectin-3 (equation 6) from the fluorescence waveform analysis was used.

This experiment was repeated with lactose functionalized dendrimers (generations 2, 4 and 6). The glycodendrimer concentrations were attenuated to match the concentration of lactose used in the previous study (concentrations of each glycodendrimer series are shown in Table 3.1). Equation 7 was modified to include a cooperativity term (*n*) to compensate for the multivalent nature of the glycodendrimers used (equation 11).

$$f_f = \frac{K_d}{K_d + [GX]^n} \tag{11}$$

Here [*GX*] represents the concentration of glycodendrimer used.

The effect of the cooperativity term in fitting the binding curve was significant for G2-lactose functionalized dendrimers but insignificant for G4 and G6 glycodendrimers (Figure 3.4). When *n* was not included as a fitting parameter, the resulting K_d was significantly higher in most cases, with the exception of trial 2 data of G4 glycodendrimer

(Table 3.1). The cooperativity term was <1 in most cases, suggesting multiple galectin-3 were bound to a single glycodendrimer.

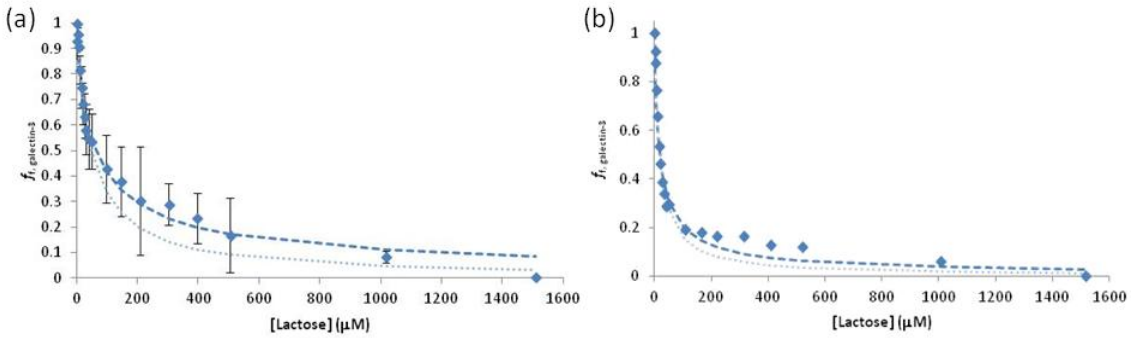

Figure 3.4. Binding curve for generations 2 (a) and 6 (b) lactose functionalized dendrimers. Measured data was fit with (dashed line) and without (dotted line) the cooperativity term, *n*.

Table 3.1. Binding constants calculated for galectin-3 and lactose functionalized dendrimers.

Glyco-dendrimer	Trial	*n*	K_d (μM)	SSE†	K_d (n=1)	SSE (n=1)
G2-lactose	1	0.87	20	1.1	32	1.2
	2	0.73	36	0.40	126	0.90
	3	0.67	15	0.60	52	1.50
G4-lactose	1	0.85	24	2.78	42	2.86
	2	1.25	77	0.19	33	0.32
G6-lactose	1	0.81	12	0.64	22	0.78

†SSE is the summed square error

When the cooperativity term is fixed to 1, implying a single galectin-3 binds to a single glycodendrimer, the binding constant for G2 and G4 lactose dendrimers (70 ± 50 μM and 38 ± 6 μM, respectively) were similar to monomeric lactose (49 ± 4 μM). The generation 6 glycodendrimer showed a slight enhancement (Figure 3.5 and Table 3.1). However, more trials are necessary to verify this.

In summary, the position of the tryptophan within the binding site of galectin-3 allowed characterization of lactose binding using FLS.

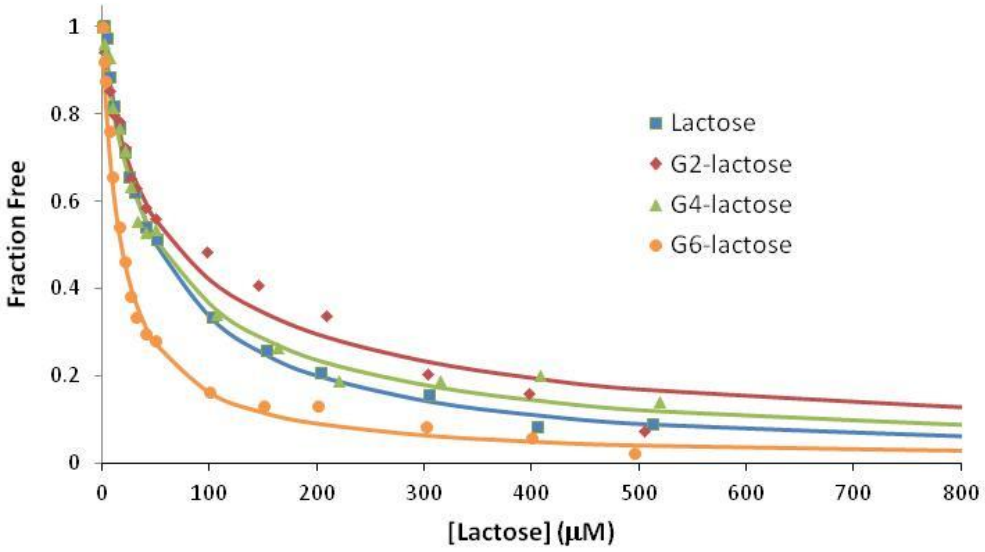

Figure 3.5. Sample binding curves for Galectin-3 with lactose functionalized dendrimers and monomeric lactose.

Application 2: Reaction Kinetics

In this second study, the change in fluorescence as a function of time following ligand addition was used to model the kinetics of aggregate formation between Concanavalin A (Con A) and mannose functionalized PAMAM dendrimers. Con A is a stable and well characterized plant lectin that binds to α-D-mannose and α-D-glucose.[80] It contains four tryptophan residues per monomer, most buried within the β-sheet motif (Figure 3.6). One of the four tryptophan residues is located on the most exterior β-strand suggesting that it could be used to report interactions between tetramers (Figure 3.6,

yellow). This was verified by observed quenching for mannose-functionalized dendrimers that was not present for the monomeric version of the sugar (Figure 3.8).

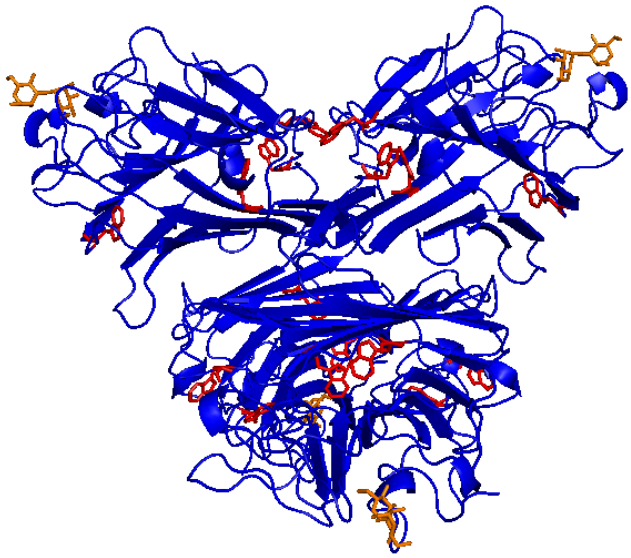

Figure 3.6. Crystal structure of Concanavalin A. Tryptophan residues are shown in red and bound mannose in yellow.

In this case, the two basis waveforms define the fluorescence decay of free and complexed forms of Con A (Figure 3.7, blue and pink curve, respectively). The free waveform was measured preceding glycodendrimer addition and the complexed waveform is obtained from the last thirty seconds of the most concentrated glycodendrimer addition. A linear combination of these two vectors was used to fit each decay curve (equation 6).

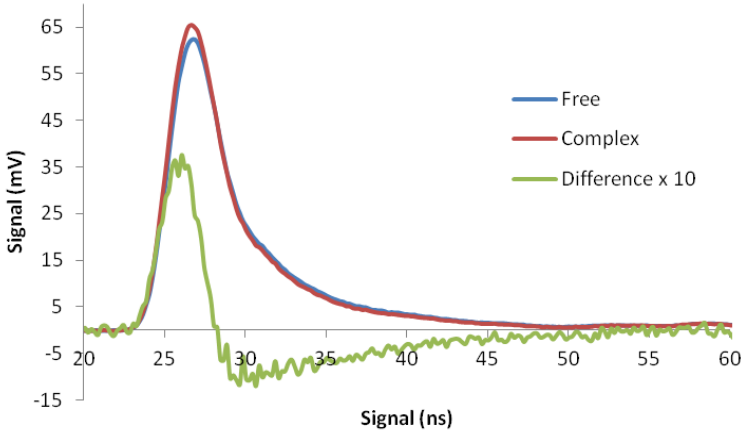

Figure 3.7. Free and complexed waveforms for Con A bound to mannose glycodendrimers.

In this case, the waveform at time *i*, *Wi*, can be represented by mixing the basis waveforms of the free and complexed Con A (W_f and W_b, respectively). The variable *i* now represents time, and *b* refers to the complexed rather than sugar-bound Con A. The relative amount of each basis waveform is again determined by the preceding coefficients. Hence, for any given time *i*, f_{fi} and f_{bi} identify how much of the free and complexed waveform, respectively, are present. Consequently, the coefficients reveal the concentration of each species at a given time (Figure 3.8). At maximal dendrimer concentration, all Con A is assumed to have entered into a protein-protein interaction, and this is an approximation.

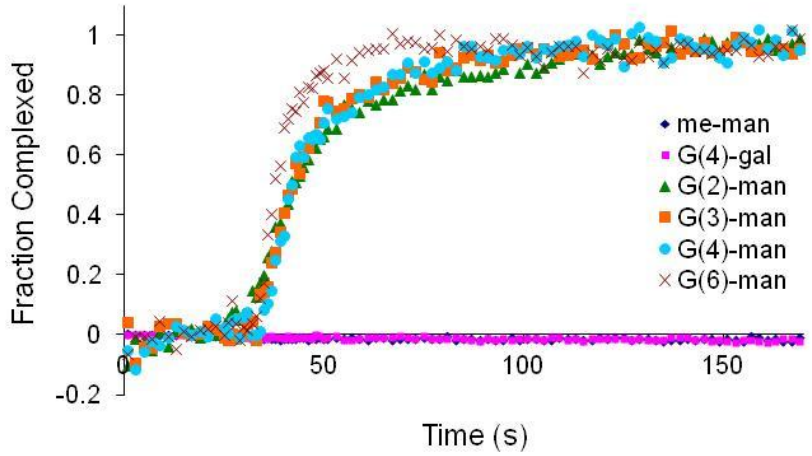

Figure 3.8. Lifetime changes expressed as the fraction complexed for a series of mannose functionalized dendrimers (G2-G6, 21-25μM), a galactose functionalized G4 dendrimer (16 μM) and monomeric mannose.(17 mM).

The kinetic profiles shown in Figure 3.8 were then modeled using the first order rate equation (equation 12). A sample fit is shown for GX-mannose + Con A (Figure 3.9).

$$f_{b,i} = f_{b,i=\infty}\left(1 - e^{-k_{obs}(T-T_0)}\right) \quad (12)$$

In this equation, k_{obs} is the observed kinetic rate, T is time of collection, T_o is time of glycodendrimer addition, $f_{b,i=\infty}$ is the fraction complexed at long times due to the pseudo first order process being modeled. It is apparent from the fit below that at times longer than 150 s the system deviates, suggesting another process is occurring. This was absent when low concentrations of glycodendrimer were used (Figure 3.10).

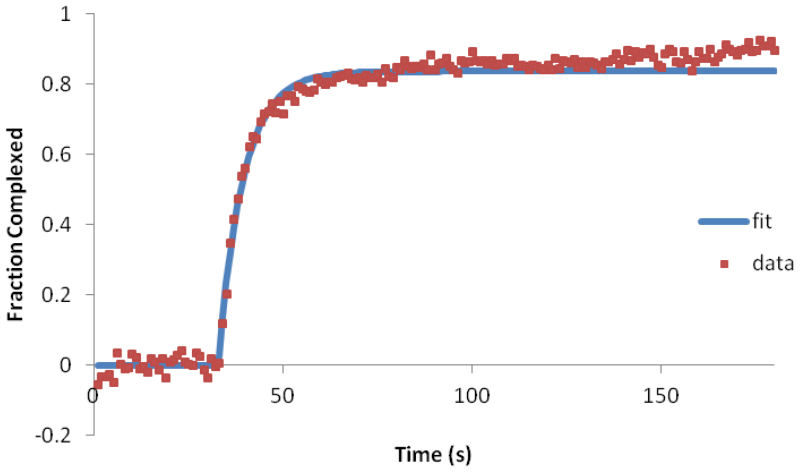

Figure 3.9. Kinetic profile of G6-mannose (65 μM) modeled using equation 12.

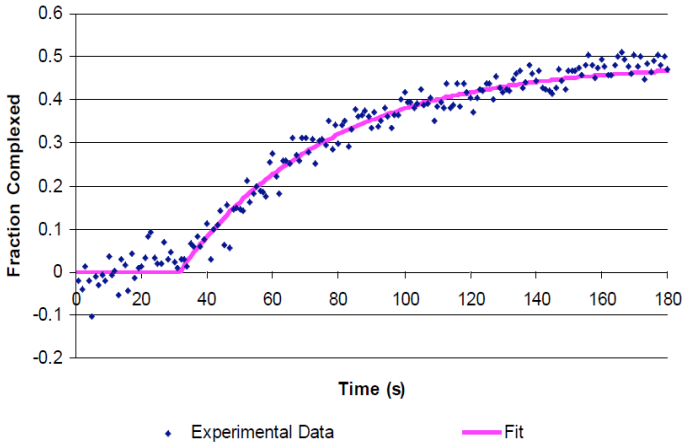

Figure 3.10. Kinetic profile of G3-mannose (1.8 μM) modeled using equation 12 (taken from supplementary materials of reference 48)

These profiles show similar rates for G2-G4 glycodendrimers and a slight increase for G6-mannose. The distance between binding sites on Con A is roughly 7 nm (Figure 4.1). Therefore, the increased rate observed for G6-mannose is likely a consequence of multivalent interactions between it and Con A. Experimental details and kinetic results can be found in reference 48 or in Chapter 5 of the graduate thesis of Dr. Kristian Schlick.

This shows that FLS can be used to track aggregate formation rates by correct positioning of the fluorophore. Kinetic data were fit using first order assumptions but the possibility to model more complex scenarios exists.

Application 3: Chemical Denaturation

The ability to track protein denaturation can provide information on the stability of a protein and factors that affect stability. The pioneering work, led by Nick Pace formed a foundation of equations to model thermal and chemical denaturation processes.[81-84] Stability can be investigated by altering the environment of the protein, say by addition of potentially stabilizing small molecules, then evaluating the effect on thermodynamic parameters calculated from denaturation profiles. Collection of denaturation profiles can be done through a variety of techniques. Examples include circular dichroism, viscosity, NMR, optical rotation, absorbance and, of course, fluorescence. A recent study on calcium ion binding to the C2A domain of synaptotagmin (a protein involved in the regulation and release of neurotransmitters and hormones) combined circular dichroism, and FLS to determine the mechanistic basis of this domain's function.[85] In this section, the chemical denaturation curves were collected using FLS as a measure of folded protein content: the stability contribution of the N-terminal domain on the overall structure of galectin-3 was evaluated.

For this case, the two 'state' waveforms from equation 6, W_f and W_b, represent the native and unfolded protein respectively. W_i represents the waveform recorded for varying concentrations, i, of denaturant. A linear combination of the native and denatured

waveforms is used, each contributing $f_{f,i}$ and $f_{b,i}$, respectively, at the specified concentration *i*. Figure 3.11 shows the chemical denaturation curve for full length (FL) and the carbohydrate recognition domain (CRD) of galectin-3. In this experiment urea was used; another common denaturant is guanidine hydrochloride.

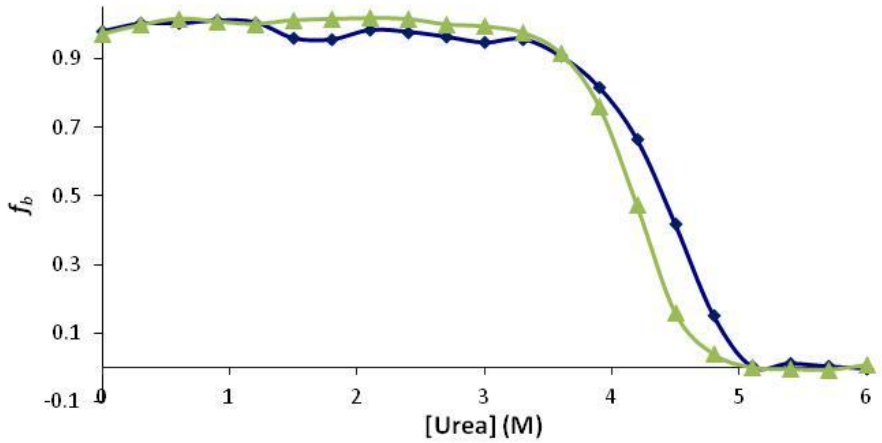

Figure 3.11. Denaturation of FL (blue) and CRD (green) of galectin-3 as a consequence of urea addition.

Urea shifts the equilibrium between the native and denatured protein to increase the population of the denatured state (equation 14).

$$N \overset{K_{eq}}{\longleftrightarrow} D \tag{14}$$

The equilibrium constant, K_{eq}, reflects the shift and can be related to the Gibb's free energy of the system (ΔG°). Since K_{eq} is simply the ratio of native and denatured forms, ΔG° can be determined using equation 15. This calculation was done for every urea concentration tested and was plotted as a function of urea concentration (Figure 3.12).

$$\Delta G^{\circ} = -RT \ln K_{eq} = -RT \ln \frac{f_b}{f_f} \tag{15}$$

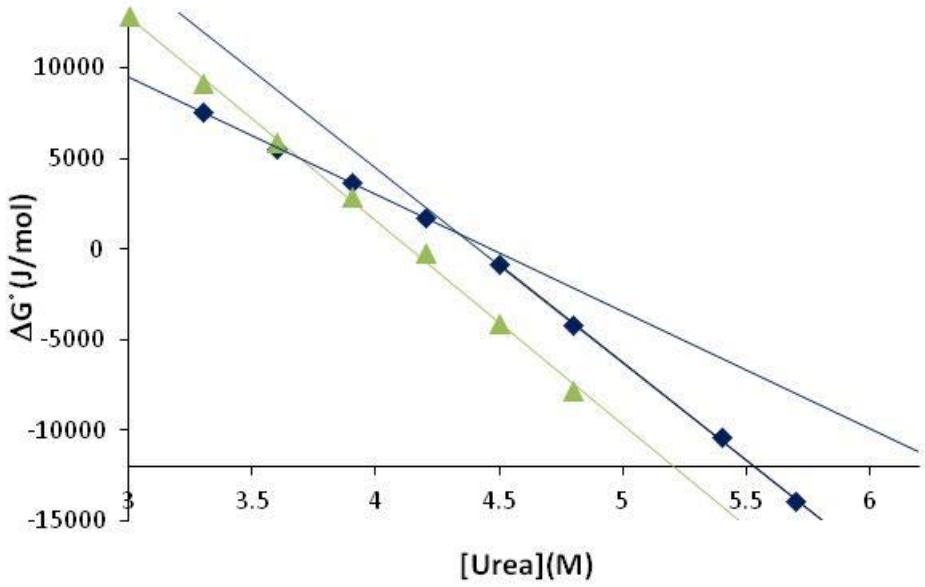

Figure 3.12. Free energy as a function of urea concentration for FL (blue) and CRD (green) constructs of galectin-3. The bi-phasic nature of FL galectin-3 required two linear fits; the fit at higher urea concentrations resembles that of the CRD.

Fitting the plot shown in Figure 3.12 provides the thermodynamic information of the system. Extrapolation to 0 M urea gives the stability of the protein in water (ΔG^{H_2O}) and the point where $\Delta G^\circ = 0$ is the midpoint of the denaturation process. Plots of ΔG° versus concentration of denaturant required a two line fit for full length galectin-3, while a single straight line fit was sufficient for the CRD. The 2nd phase of the FL profile was very similar to the CRD, (Table 3.2) suggesting that at higher than 4.5 M urea, any stabilizing effect of the N-terminal domain is eliminated. If it is assumed that this stabilization is a result of galectin-3 dimerization (i.e., the ΔG° extrapolation reflects the stability of binding), the calculated association constant is 9 μM.

Table 3.2. Denaturation results for full length galectin-3 (FL) and the carbohydrate recognition domain (CRD).

galectin-3 construct	Denaturation Midpoint (M urea)	$\Delta G^{H_2O,1}$ (kJ/mol)†	$\Delta G^{H_2O,2}$ (kJ/mol)†
FL	4.34	46.6	28.8
CRD	4.16	47.6	NA

†$\Delta G^{H_2O,1}$ and $\Delta G^{H_2O,2}$ are from the straight line fits at high and low urea concentrations, respectively. At high concentrations, the stability enhancement due to the presence of the N-terminal domain is gone and represents the unfolding of the CRD.

This study shows the applicability of FLS in determining protein stability. Given that higher concentrations of urea were required to unfold galectin-3, it is assumed that the N-terminal domain can serve as a stabilizing factor. Further investigation would need to be done to determine if this stabilization was a result of the N-terminal domain interacting with the CRD or if the N-terminal domain facilitates oligomerization which is the stabilizing factor.

Summary

This chapter discussed several studies that use the same technology integrated in the NovaFluor microplate readers to evaluate thermodynamic and kinetic parameters. These studies reveal the robust and precise nature of this technology and the sensitivity of protein tryptophan fluorescence. The basis of the various analyses comes from the ability to analyze fluorescence decay spectra as linear combinations of basis functions. Typically one or both basis functions are measured, but this would not be necessary if more complex algorithms (such as principle component analysis) were used.

The FLS studies of glycodendrimer binding to lectin proteins show increased avidity and possible multivalent interactions (Con A with G6-mannose) as a result of sugar attachment to the PAMAM scaffold. The tryptophan positioning within the protein matrix is critical in deciding what parameters can be evaluated. For galectin-3, the tryptophan lies in the binding site and only the sugar binding event could be characterized. Con A does not contain a tryptophan in the binding site, so sugar binding did not affect the fluorescence waveform. However, when another Con A was in close proximity, quenching was observed. This is likely a result of the tryptophan located on the exterior β-strand being quenched.

CHAPTER 4

PROTEIN AGGREGATION MEDIATED BY FUNCTIONALIZED DENDRIMER SCAFFOLDS

Background on Protein Models and Dendrimer Functionalization

The primary goal of this project was to determine how the strength of binding and valency of oligomeric proteins affect aggregates formed with multivalent scaffolds. There are several factors to consider for a multivalent interaction, including (1) monomeric binding affinity, (2) spacing between binding sites/ligands, (3) valency or number of binding sites, and (4) induced interactions between similar entities docked in close proximity. These factors dictate the length of time for an interaction between two multivalent entities (i.e., k_{on} and k_{off}) and are expected to alter assembly characteristics. The three protein systems selected for this investigation are described below.

Concanavalin A

Concanavalin A (Con A) is a well-characterized plant lectin (Figure 4.1) that interacts with cell surface glycoproteins to trigger mitosis[86] and apoptosis[87]. Its native quaternary structure consists of four polypeptides oriented in a tetrahedral configuration. The four monomers each contain a single binding site for α-D-mannosyl and α-D-glucosyl groups.[80] The sugar binding site is shallow, resulting in a relatively weak (10^{-3} M) binding affinity for mannose. Multivalency is used in this protein-ligand system to enhance binding. When the spacing of functionalized dendrimer scaffolds positions mannose units at distances that meet or exceed the distance between Con A binding sites

(6.5 nm) a cooperative process vastly enhances binding avidity (>250 fold).[7, 88] Additionally, presentation of mannose in a trimeric form increases the binding affinity over 100 fold.[89,90] This enhancement is greater than that expected from statistical or proximity effects (see Figure 1.3 for diagram of statistical and proximity effects).

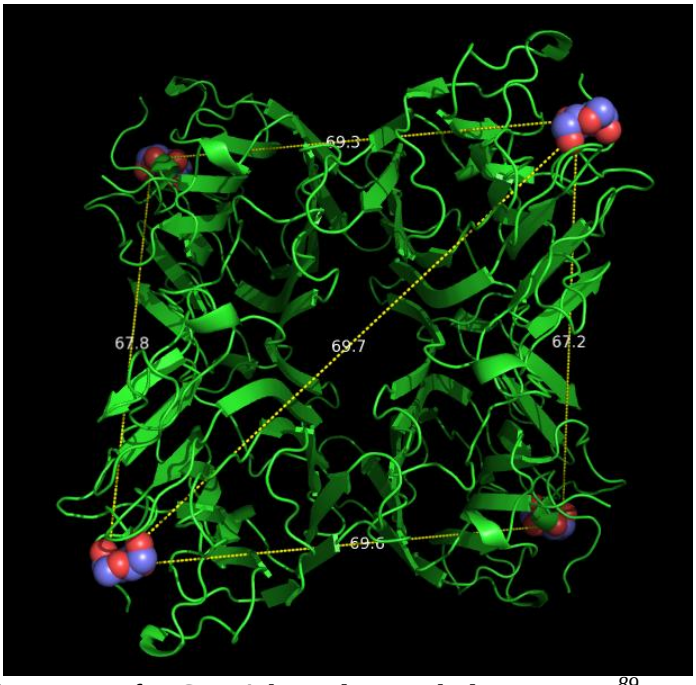

Figure 4.1. Crystal structure for Con A bound to methyl mannose. [89]

Streptavidin

Streptavidin is a biotin binding protein secreted from *Streptomyces avidinii*, and is commonly used in immunoassays due to its stability and high specificity for biotin.[91] The native oligomeric state for this protein is a tetramer and the distance between binding sites is approximately 2.5 nm (Figure 4.2).

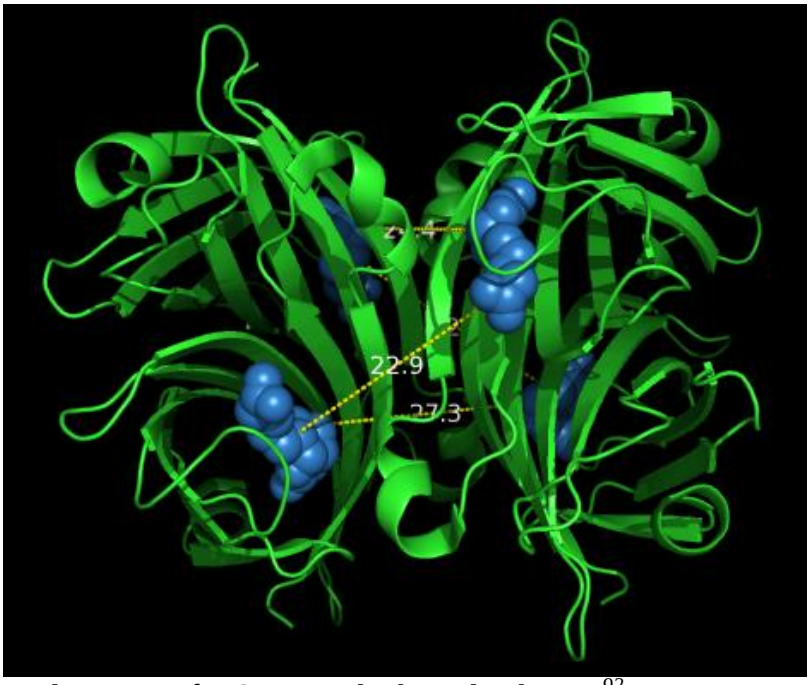

Figure 4.2. Crystal structure for Streptavidin bound to biotin.[92]

The monomeric binding affinity for biotin is on the order of 10^{-14} M. Rather than containing a shallow binding pocket, as seen for Concanavalin A, the twisted β-sheet structure and flexible loop surround biotin upon entering the binding pocket (Figure 4.3). X-ray diffraction data reveal that biotin binding alters the β-sheet at the dimer interface creating a more compact, stable structure. [92] It is for these reasons that biotin forms an almost irreversible interaction with streptavidin.

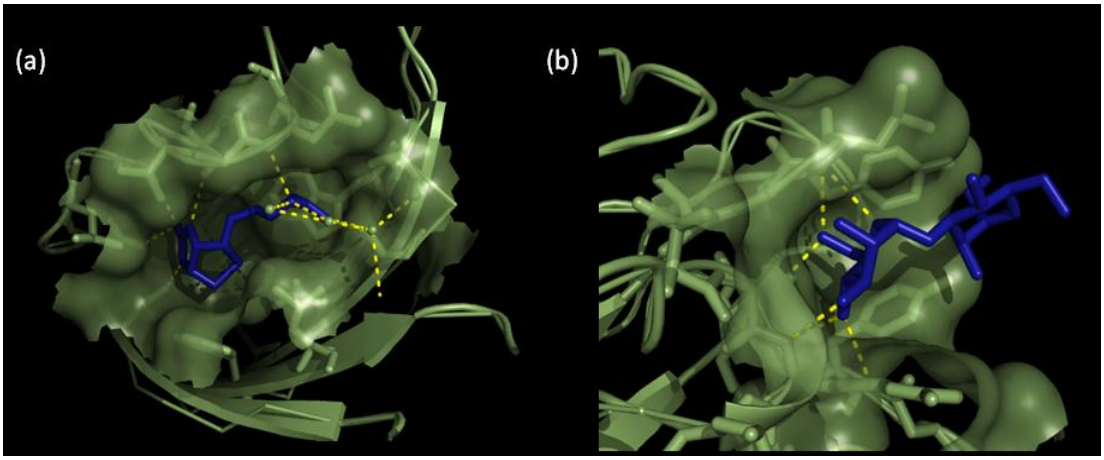

Figure 4.3. Surface rendition of binding pockets for (a) biotin bound by streptavidin and (b) mannose bound by Con A. Con A has a relatively shallow binding pocket and fewer hydrogen bonds between oxygen and nitrogen atoms of side chain residues when compared to streptavidin. The flexible loop regions between β-sheets organize around the biotin molecule within the streptavidin binding site.

Galectin-3

Galectin-3 is a member of the galectin family of proteins. This family is characterized by their ability to bind β-galactoside sugars. The function and exact mechanism used by galectins for interpreting biological information encoded in glyco-conjugates remains largely unknown. Expression levels of galectin-3 are highest in innate immune cells and epithelial cells, and modulation of expression is correlated with certain bacterial infections[92] and increased invasiveness and metastatic potential of several cancers. [93] Localization to cellular interfaces suggests a role in cell-cell adhesion. [94] The chimeric structure of galectin-3 contains an unusually long and unstructured N-terminal domain and a conserved carbohydrate recognition domain (CRD) (Figure 4.4). The residues within the binding site reorganize water molecules to facilitate binding of β-galactosides..[79] The tail domain is highly flexible, is rich in proline and glycine residues, and is implicated in oligomerization, secretion and signaling activities of galectin-3. [95]

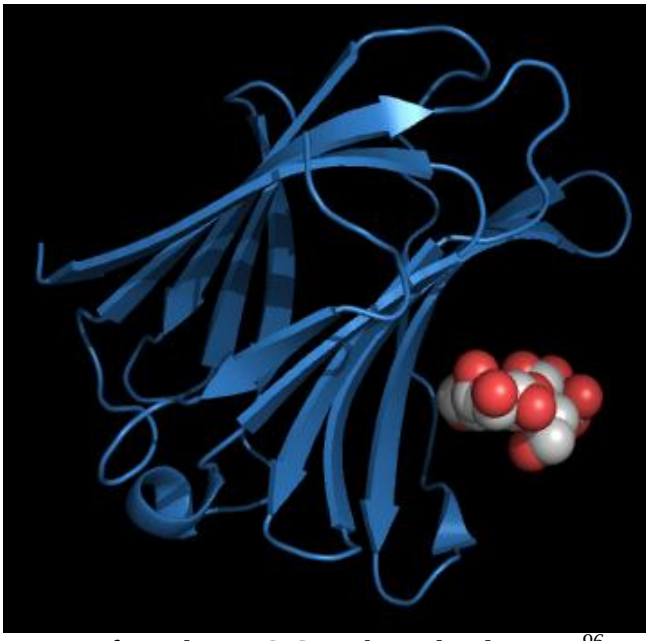

Figure 4.4. Crystal structure for galectin-3 CRD bound to lactose.[96]

The multivalent potential of galectin-3 lies in the ability of N-terminal domains to interact and promote oligomerization. Increased affinity and proximity have been observed for full length galectin-3 compared to a CRD variant, supporting this domain's role in oligomerization.[94, 97] The preferred oligomeric state is believed to be a dimer, however, pentamers have been observed at high concentrations.[98] The amino acid sequence of the N-terminal domain consists of 9 tandem repeats of Y-P-G-X(3)-P-G-A which is similar to the G-P-X and G-X-P(OH) motif found in collagen. Collagen provides strength and resilience to tissue by forming triple helical fibrils. Their formation requires Vitamin C to oxidize proline residues to hydroxyproline.[99] The sequence similarity of the N-terminal domain of galectin-3 to collagen suggests that this domain has the potential to interact with itself and that *in vivo* this interaction may require additional cofactors. Additionally, C-terminal domain interactions have been observed suggesting other forms

of protein-protein interactions.[100] Formation of oligomers having variable oligomerization states could contribute to the overall function of this lectin, allowing variability in the distance between carbohydrate binding sites and eliciting specific and distinct responses based on expression levels.[101]

Functionalized Dendrimer Scaffold

A series of three ligand functionalized dendrimers of second, third, fourth, and sixth generation PAMAMs were labeled with mannose, lactose and biotin endgroups (Figure 4.5). Mannoside and lactoside labeled PAMAM dendrimers were prepared according to previously reported methods.[88, 102] Amanda Mattson graciously synthesized biotinylated functionalized dendrimer by coupling a biotin containing linker to the mannose functionalized dendrimers; their synthesis and characterization will be reported in Amanda Mattson's doctoral dissertation. All functionalized dendrimers were characterized using MALDI-TOF MS, ^{1}H and ^{13}C NMR spectrometry.

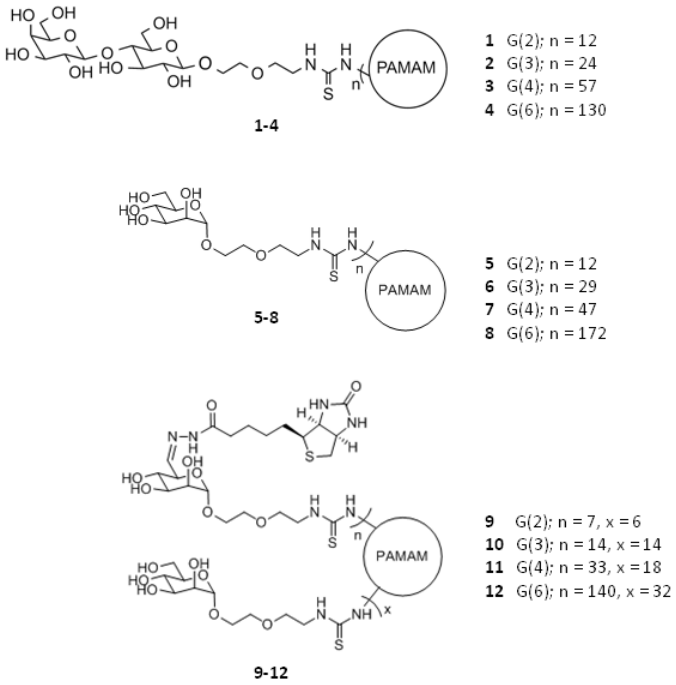

Figure 4.5. Ligand functionalized PAMAM dendrimers. Synthesis and characterization procedures can be found in References 88 and 102 for mannose and lactose functionalized dendrimers, respectively.

Aggregate Size Characterization

Spontaneous aggregates were formed when the above ligand-functionalized PAMAM dendrimers were added to solutions containing the corresponding protein binding partner. Two primary techniques were used to characterize these aggregates: dynamic light scattering and fluorescence microscopy. These techniques provided information regarding the effects of concentration, binding strength and valency on the size, morphology and population distribution of the particles formed. Micrographs were taken of fluorescently-labeled proteins incubated with functionalized dendrimers to directly view aggregates. Dynamic light scattering provided a more rapid technique to characterize the size and polydispersity of aggregates. Considering the different detection

levels of each technique, both methods provided similar results. This chapter briefly discusses the experimental considerations for each method and reports the results from these measurements.

Dynamic Light Scattering (DLS)

Dynamic light scattering (DLS) correlates fluctuations of scattered light with time to calculate hydrodynamic radii and polydispersity of a set of particles. The autocorrelation function ($g(t)$) is exponential in nature and fit assuming spherically shaped particles.

As discussed previously (Methods for Analyzing Fluorescence Lifetime Data, Chapter 3), fitting exponential decays such as the autocorrelation function is a sensitive procedure, and various routines are available. The analysis algorithms of the DLS software fit the autocorrelation function by either (1) expanding the exponential correlation function via Taylor series expansion then using a normal, linear least squares fit to determine cumulants; or (2) fitting the exponential directly using a non-linear least squares fitting algorithm to solve for Γ and amplitude factors. The first method is referred to as the method of cumulants. Cumulants are coefficients to the Taylor series expansion and can be related to the intensity correlation decay rate, Γ, and distribution width. NNLS and CONTIN algorithms make use of the second fitting procedure. In both cases, the resulting physical parameters (i.e., diameter and polydispersity) are calculated from the determined variables (cumulants or Γ and amplitude factors).

Both fitting methods provide similar mean values (within 5%), but the method of cumulants has increased sensitivity to background corrections.[103] Similarity was

experimentally observed when (1) precautions were taken to minimize background (filtering all solutions and pre-rinsing cuvettes with filtered buffer), (2) sufficient signals could be measured, and (3) samples were mostly monodisperse. When these criteria were not all met, then the method of cumulants did not provide reasonable results, and results from CONTIN analysis were reported.

Experimental. Samples were prepared at slight, moderate and large molar excess of protein and incubated for 1 hour at RT. Single scans were recorded prior to addition of functionalized dendrimers. Triplicate scans were recorded following the one hour incubation period. The concentration of stock protein samples was determined by measuring the absorbance at 280 nm and using an $\varepsilon^{1\%}$ of 6.1[98], 13.7, and 10.7 for galectin-3, Con A and streptavidin, respectively. Sugar functionalized glycodendrimers were synthesized similar to previous methods[102, 104] and stock samples prepared by dissolving the lyophilized powder in filtered Millipore water to a final concentration of 100, 10 and 1 μM. Varying amounts of glycodendrimer were added to the protein solution to give molar ratios of 3:1, 9:1 and 220:1,protein-to-functionalized dendrimer (see Tables 4.1-4.3 for concentrations used) and incubated for 1 hour at room temperature. The reported data is the average of triplicate measurements on 1-6 samples. High relative variances were obtained for samples where the particle size was too small or too few particles were present to be detected (counts per seconds were less than 20,000). High relative variances (greater than 0.5) are characteristic of highly polydisperse samples and could not be fit well using the method of cumulants.

In this study, Con A was resuspended in PBS and then filtered to remove any insoluble particles. PBS was selected because it is a universal buffer that represents physiological ionic strength and pH. Since the hydrodynamic radius calculated in light scattering is ultimately calculated from the ionic mobility, it was important to maintain this parameter.

Evaluation of DLS Data. Regardless of the amount of excess galectin-3 that was used, the size and polydispersity of the aggregates were shown to increase with increasing dendrimer generation (Figure 4.6 and Table 4.1). The largest aggregates were observed for the 9:1 ratio of galectin-3-to-glycodendrimer, and smaller aggregates were formed when a large excess or a very small excess of galectin-3 was used. This trend is logical if the glycodendrimer is serving as the nucleating agent for galectin-3 aggregation. For example, when the concentration of galectin-3 is comparable to the concentration of glycodendrimer, then galectin-3 is presented with many different nucleating scaffolds, and smaller particles are formed. On the other hand, when galectin-3 is present in large excess, not as many nucleating sites can be incorporated into each aggregate, which causes the aggregates to be smaller.

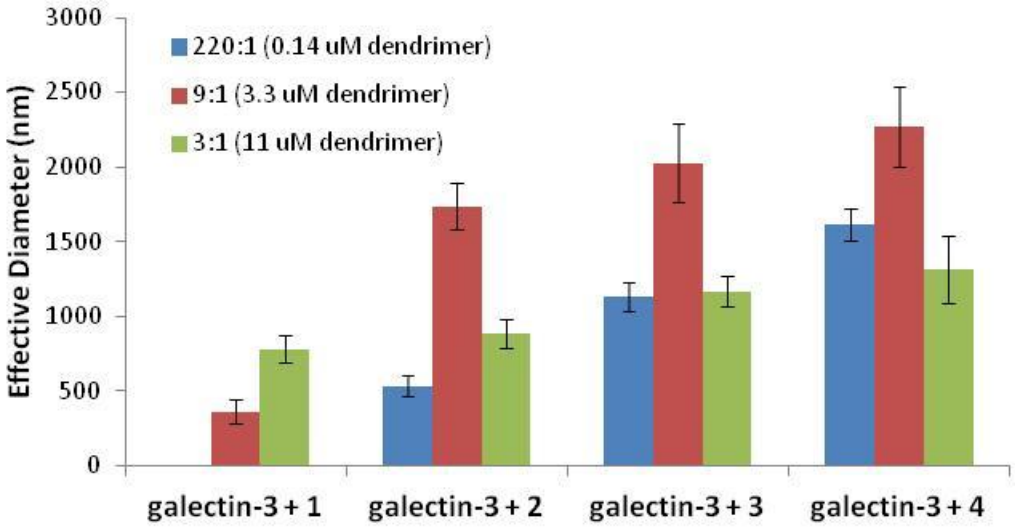

Figure 4.6. Galectin-3 nanoparticle formed in the presence of compounds **1-4** at (blue) 220 fold excess, (red) 9-fold excess, and (green) 3-fold excess galectin-3. Aggregates size increases as glycodendrimer generation increases. Largest aggregates are observed for samples containing 9x molar excess galectin-3.

Table 4.1: Summary of DLS results for galectin-3 and lactose functionalized dendrimer aggregates.

Compound Number	[gal-3] (μM)	[dendrimer] (μM)	Effective Dia. (nm)	Relative Variance	Signal (kcps)[a]
NA	32	0	NR[b]	NR[b]	14 ± 6
1	0	0.14	NR[b]	NR[b]	5.5 ± 2.2
	0	11.5	NR[b]	NR[b]	23 ± 0.6
2	0	0.14	NR[b]	NR[b]	3.2 ± 0.8
	0	11.5	2.0 ± 0.4[c]	42 ± 34[d]	244 ± 63
3	0	0.14	NR[b]	NR[b]	3.8 ± 0.8
	0	11.5	6.2 ± 1.1[c]	69 ± 78[d]	167 ± 5
4	0	0.14	NR[b]	NR[b]	4.4 ± 0.3
	0	11.5	10.6 ± 2.2[c]	10.6 ± 2.5[d]	208 ± 8
1	31	0.14	NR[b]	NR[b]	28 ± 12
	31	3.3	364 ± 77	0.21 ± 0.05	60 ± 23
	31	11.5	781 ± 88	0.20 ± 0.04	135 ± 28
2	31	0.14	533 ± 72	0.16±0.07	94 ± 24
	31	3.3	1744 ± 161	0.17±0.06	282 ± 59
	31	11.5	1275 ± 377	0.19±0.07	214 ± 134
3	31	0.14	1177 ± 81	0.19±0.03	385 ± 26
	31	3.3	2027 ± 263	0.20±0.10	246 ± 52
	31	11.5	871 ± 278	0.25±0.04	292 ± 74
4	31	0.14	1616 ± 111	0.23±0.09	271 ± 73
	31	3.3	2269 ± 266	0.23 ± 0.15	249 ± 65
	31	11.5	1316 ± 223	0.19 ± 0.08	252 ± 94
2 + 1 mM lactose	31	0.14	NR[b]	NR[b]	14 ± 2
3 + 1 mM lactose	31	0.14	NR[b]	NR[b]	17 ± 10
4 + 1mM lactose	31	0.14	NR[b]	NR[b]	25 ± 11
8	34	0.14	4 ± 3[x]	13 ± 9[b]	39 ± 11
NA	34(CRD)	0	NR[b]	NR[b]	5 ± 0.3
3	34(CRD)	0.14	NR[b]	NR[b]	10 ± 1

[a]kcps= kilocounts per second.
[b]Insufficient signal to accurately fit, NR = Not reliable result.
[c]Mean diameter of major peak (accounts for >99% of distribution population) from CONTIN analysis (cumulant fit inadequate due to the bimodal nature of the sample as evident from high relative variances from this analysis).
[d]Relative variance as reported from CONTIN fit.

A series of control experiments indicate that aggregation is induced by the binding of galectin-3 to lactose on the dendrimers. Aggregates could not be observed upon

addition of compound **8**, a mannose functionalized G6 dendrimer. Pre-incubation of galectin-3 with 1 mM lactose solution completely inhibited aggregate formation in the presence of glycodendrimers **2-4** (Table 4.1). Experiments using **4** and a truncated form of galectin-3 showed only a slight increase in the average scattered intensity and did not result in aggregate formation (Table 4.1). The truncated form of galectin-3 only contains the carbohydrate recognition domain without the *N*-terminal domain. No aggregates were observed for dendrimers **1**-**4** in solution without addition of galectin-3, and no aggregates were observed for galectin-3 when glycodendrimers were absent from the solution. Taken together, these data support aggregate initiation as a response to specific carbohydrate binding interactions between lectin and glycodendrimer. These data also reveal the significance of the *N*-terminal domain in formation of higher order aggregates.

Aggregates of Con A and mannose functionalized dendrimers **5**-**8** were more polydispersed than the glycodendrimer/galectin-3 aggregates (Figure 4.7 and Table 4.2). Significantly lower protein concentrations were required to remain within the specified limits of detection (LOD) of the DLS instrumentation (2 nm-2 μm). A set of experiments using compound **8** and 220x excess Con A were performed to determine the optimal protein concentration to characterize nanoparticles using DLS. Samples prepared at 4 μM Con A exceeded instrumental LOD after roughly 40 minutes (Figure 4.12). Scattering of lower concentration samples produced signals too low for reliable fitting (>20 kcps). Even at the optimized concentration, aggregates formed at 9:1 and 3:1 molar excess for compounds **6**-**8** exceeded the detection limits.

In general, by increasing the concentration of glycodendrimers larger aggregates were formed. The exception to this is compound **8** which showed a maximum aggregate size at molar ratios of 9:1 protein-to-glycodendrimer. The deviation in the calculated particle radius for all Con A/ glycodendrimer aggregates is shown in Figure 4.7 to be large, making it difficult to confidently compare between ratios. The Student T-test (unpaired, unequal variances) was used to validate the trend observed for compound **8** with Con A. Results for the t-test showed that there were statistically significant differences between aggregate diameters at 9:1 protein-to-glycodendrimer and 220:1 protein-to-glycodendrimer, and between aggregate diameter at 9:1 protein-to-glycodendrimer and 3:1 protein-to-glycodendrimer. The calculated t-statistics for both comparisons were very close to the critical value, demonstrating the high uncertainty of the radii measurements. Increasing the number of trials would provide higher confidence that the difference in average diameters is real. Comparison of aggregates between the 3:1 protein-to-glycodendrimer sample and 220:1 protein-to-glycodendrimer sample showed no significant difference.

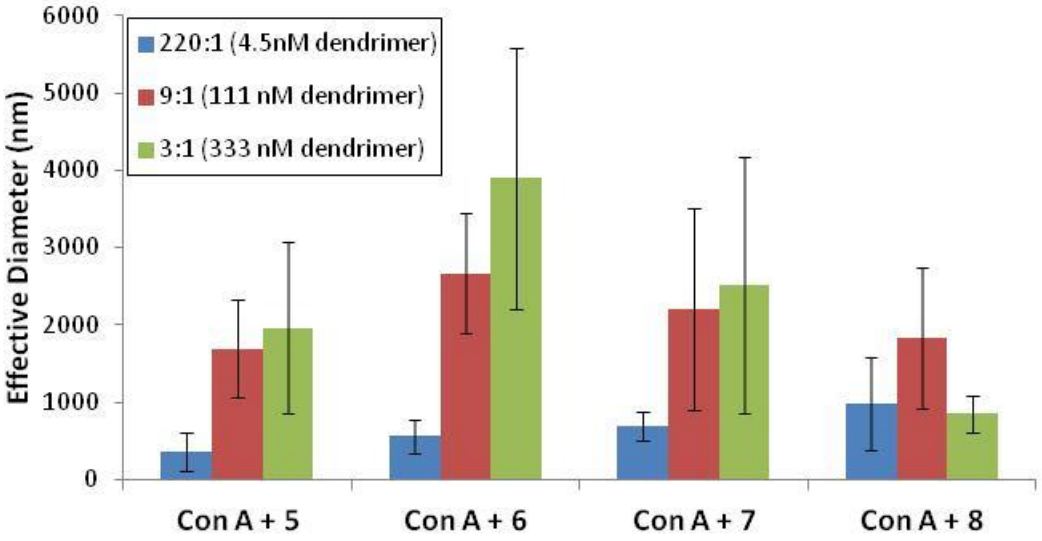

Figure 4.7. Con A aggregates formed in the presence of compounds **5**-**8** at 220 (blue), 9 (red) and 3 (green) times molar excess Con A. Larger aggregates are observed for increasing concentrations of glycodendrimer used with the exception of compound **8** which showed the largest aggregate at 9x molar excess protein.

That the dendrimer mediated aggregation of Con A was a response to sugar binding events was confirmed by aggregate disassembly in the presence of 16 mM mannose. A 16-fold higher concentration of the monomeric sugar than was required to dissolve galectin-3 glycodendrimer aggregates. Given that Con A contains 2 to 4 times more available binding sites per oligomer and that the multivalent binding for generation 6 dendrimers and Con A is known to significantly increase binding avidity[7] this is not an unreasonable result. This enhanced avidity could also explain the increased polydispersity of this system. Multivalent interactions prolong the time molecules spend in contact, meaning that transition from a kinetic to thermodynamic equilibrium state is slow. Fast assembly has been shown to adversely affect the formation of regular gold nanoparticles.[105] By slowing the kinetics, thermodynamically favored products can result for each set of interactions resulting in regular growth. DLS measurements assume a

spherical particle with isotropic scattering regardless of molecular orientation. Non-spherical aggregates are likely the source of the increased polydispersity observed for Con A and mannose functionalized dendrimers.

Table 4.2 Summary of DLS results for Con A and mannose functionalized dendrimer aggregates.

Compound Number	[Con A] (μM)	[dendrimer] (nM)	Effective Dia. (nm) [b]	Relative Variance	Signal (kcps)[a]
NA	1	0	NR[b]	NR[b]	3 ± 1
	3.9	0	NR[b]	NR[b]	23 ± 1
8	0	0.14	NR[b]	NR[b]	18 ± 1
		20	3.3 ± 1.4	0.70±0.02	115 ± 2.6
5	1	4.5	NR[b]	NR[b]	17 ±5
		111	1691 ± 634	0.49 ±0.38	229 ±50
		333	1963 ± 1111	1.6 ±3.2	288 ±24
6	1	4.5	558 ± 222	0.13 ±0.12	37 ±8
		111	2667 ± 782	0.28 ±0.28	306 ±84
		333	3894 ± 1689	0.61 ±1.0	222 ±69
7	1	4.5	686 ± 188	0.13 ±0.11	58 ±7
		111	2205 ± 1311	0.49 ±0.74	233 ±87
		333	2518 ± 1656	1.8 ±2.9	265 ±92
8	1	4.5	981 ± 601	0.50 ±0.68	139 ±103
		111	1828 ± 903	0.24 ±0.28	303 ±178
		333	848 ± 233	0.23 ±0.18	301 ±32
8 + 16 mM mannose	1	4.5	NR[b]	NR[b]	4 ± 2

Summary of DLS results for Con A and mannosyl dendrimer aggregates.
[a]kcps= kilocounts per second.
[b]Recorded from CONTIN analysis due to increased polydispersity yielding unacceptable cumulant fits,
NR = Not a reliable result.

Similar results were obtained for Streptavidin/biotin-labeled dendrimer systems. Aggregates formed non-spherical particles as shown by fluorescence microscopy (Figure 4.10). Results from DLS experiments are shown in Table 4.3 only to afford an indication of the size variability and high relative variances obtained with streptavidin. The high

affinity interaction, combined with the enhanced affinity of sugars displayed on a polyvalent scaffold prevented aggregates from being disrupted. This statement is supported by the observation of a structured autocorrelation curve and no appreciable change in signal upon addition of free biotin.

Table 4.3 Summary of DLS results for Streptavidin and biotin functionalized dendrimer aggregates.

Compound Number	[Streptavidin] (μM)	[dendrimer] (μM)	Effective Dia. (nm) [b]	Relative Variance
9	20	0.091	604 ± 930	12 ± 13
		2.2	407 ± 264	9 ± 11
		6.7	264 ± 409	13 ± 11
12	10	0.045	312 ±250	6 ± 7
		1.1	237 ± 364	8 ± 9
		3.3	324 ± 161	2 ±1
12	20	0.091	150 ± 39	10 ± 5
		2.2	444 ± 89	4 ± 2
		6.7	189 ± 135	9 ±6
8 + 1 mM biotin	20	2.2	8895 ± 2615	

[a]kcps= kilocounts per second.
[b]Recorded from CONTIN analysis due to increased polydispersity yielding unacceptable cumulant fits

Fluorescence Microscopy (FM)

To confirm the general trends observed in DLS measurements, micrographs of aggregates containing fluorescently labelled proteins were collected. Skrdla points out that "...although the fluorescence microscope cannot provide spatial resolution below the diffraction limit of the respective objects, detection of fluorescing molecules below such limits is readily achieved."[106] This is in part due to the sensitivity of fluorescence measurements.

FM Results and Discussion. FITC-Con A and FITC-streptavidin (Sigma Aldrich) were commercially available, and galectin-3 was labeled with AlexaFluor 488 following the manufacturer's protocol (brief description can be found in Appendix B). Functionalized dendrimer samples were added to fluorescently labeled protein samples using similar protein concentrations and molar ratios of protein-to-glycodendrimer as were used in the DLS experiments described above. After approximately 1 hour incubation at room temperature, a 10 μL aliquot was removed and mounted for viewing. An Olympus B61X microscope (100x oil immersion objective) equipped with a CCD camera was used to capture 20-30 images of fluorescent aggregates. Aggregate size was quantified using image analysis software (Pixcavator 6.0) in a similar manner to reference 34. Fluorescent microsphere standards (Dragon Green, Bangs Laboratories, Inc.) were used to create calibration equations to convert image pixels to particle diameter.

Image processing of standard particles provided a linear relationship between the reported particle diameter and number of pixels from the computed perimeter variable of the image analysis software (Figure 4.8, images of fluorescence standards are shown in Figure 4.9, a-d). Equations and goodness of fit are given in Table 4.4.

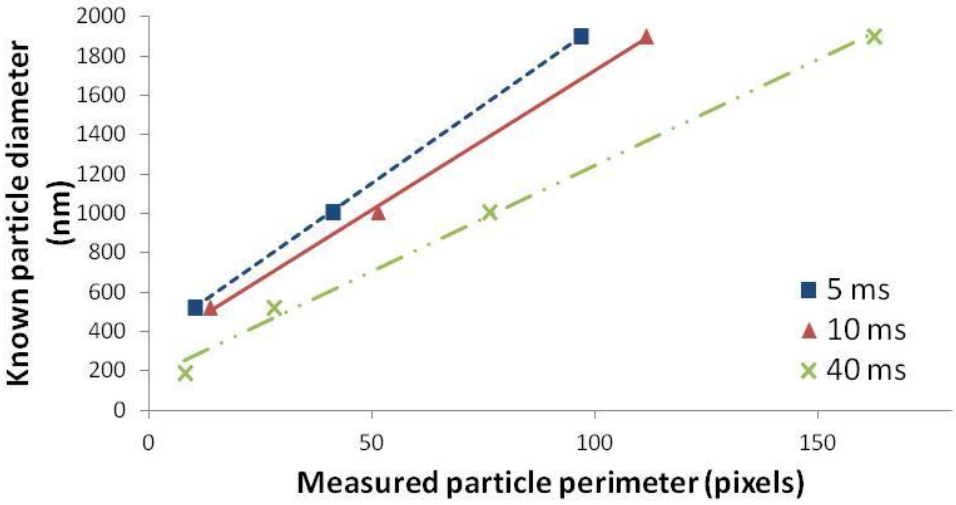

Figure 4.8. Calibration curve correlating pixel number (perimeter) to particle diameter Olympus microscopes.

Table 4.4. Calibration equations for fluorescent standard microspheres.

Camera	Exposure time (ms)	Calibration Curve Equation[a]	R-squared value
Olympus B61X	5[b]	Y=15.94x + 355.8	1.0
	10[b]	Y=14.19x + 309.8	0.9988
	40	Y=10.79x + 164.9	0.9956

[a]Y represents particle diameter, and x is the number of pixels of the particle perimeter as quantitated by Pixcavator. [b]190 nm standard could not be detected and was not included in the fit.

Initial attempts to use Alexa 488-labelled dendrimers revealed that the concentration of dendrimer was too low to obtain visible particles (0.14 μM dendrimer at lowest concentration tested). However, Alexa 488-labelled galectin-3 provided viewable aggregates for the tested ratio of 220:1 protein-to-glycodendrimer. The DLS measurements of the dye labelled protein and glycodendrimer aggregate reported an average diameter of 1550 ± 60 nm (single sample, triplicate scans). Therefore, addition of the dye did not affect the aggregation process. Processing of FM provided similar results to the unlabelled protein supporting the idea of a large monodispersed population of

particles (Table 4.5 and Figure 4.9, e-h). For both methods, the trend of increasing size and polydispersity with increasing dendrimer generation was observed.

Table 4.5. Micrograph characterization of galectin-3/lactose functionalized dendrimer aggregates following 1 hour incubation

Compound†	D_{hyd} (nm)	D_N (nm)	σ D_N (nm)	Relative Variance	D_W (nm)	PDI
1	ND	240	47	0.20	253	1.1
2	533	573	71	0.12	587	1.0
3	1177	1331	300	0.23	1402	1.1
4	1616	1788	647	0.36	1904	1.1

†Dendrimers were added at 1/220 the concentration of protein
D_{hyd}=hydrodynamic radius from DLS measurement
D_N=number average diameter
Relative variance = σ/D_N
D_W = weighted average diameter =Σ(diameter × frequency); frequency represented as a percent of total particles sampled
PDI=polydispersity index=D_W/D_N
ND=not determined

Micrographs of 220 fold excess Con A with mannose functionalized dendrimers contained a large number of small particles (less than 10 pixels) and a smaller population of larger particles, as shown in Figure 4.9 (i-l) and summarized in Table 4.6. In some cases, the relative variances calculated for DLS data collected on these samples were greater than 0.5 suggesting a multimodal distribution of particles, and the average particle diameter reveals the bias in favor of larger aggregates. (Table 4.2) Smaller particles were not consistently observed in DLS measurements, but evident in the Con A glycodendrimer micrographs suggesting that their presence is real. Taken together, these data support the view of a polydisperse population of aggregates.

Table 4.6. Micrograph characterization of Con A (1 and 4 μM)/mannose functionalized dendrimer aggregates following 1 hour incubation

[Con A]	Compound†	D_{hyd} (nm)	D_N (nm)	σ D_N (nm)	Relative Variance	D_W (nm)	PDI
1μM	**5**	ND	315	54	0.17	337	1.1
	6	558	397	150	0.38	525	1.3
	7	686	400	128	0.32	452	1.1
	8	981	370	116	0.31	506	1.4
4μM	**5**	ND	614	512	0.83	1044	1.7
	6	ND	549	343	0.63	819	1.5
	7	ND	608	491	0.81	1007	1.7
	8	1666*	2653	8491	3.20	28899	10.9

†Dendrimers were added at 1/220 the concentration of protein
D_{hyd}=hydrodynamic radius from DLS measurement
D_N=number average diameter
Relative variance = σ/D_N
D_W = weighted average diameter =Σdiameter×frequency; frequency represented as a percent of total particles sampled
PDI=polydispersity index=D_W/D_N
ND=not determined
*standard deviation for triplicate scans of triplicate samples was 730 nm

At higher concentrations of Con A, DLS could not provide reliable results for aggregate size. Particles could be visualized in fluorescence micrographs, and again there was a significant population of small particles (Figure 4.9). Images were processed in a similar manner as galectin-3/lactose dendrimer aggregates to determine the particle diameter even though particles for this system were not spherical (Table 4.6). This means that the 2-dimensional images fail to fully capture the 3-dimensional features of the aggregates. Depending on the selected Z-plane, a different aggregate size could be measured for the same particle due to the highly irregular shapes of these particles. The irregular morphology of these aggregates means that the quantization procedure will likely not reflect the absolute size of the particle.

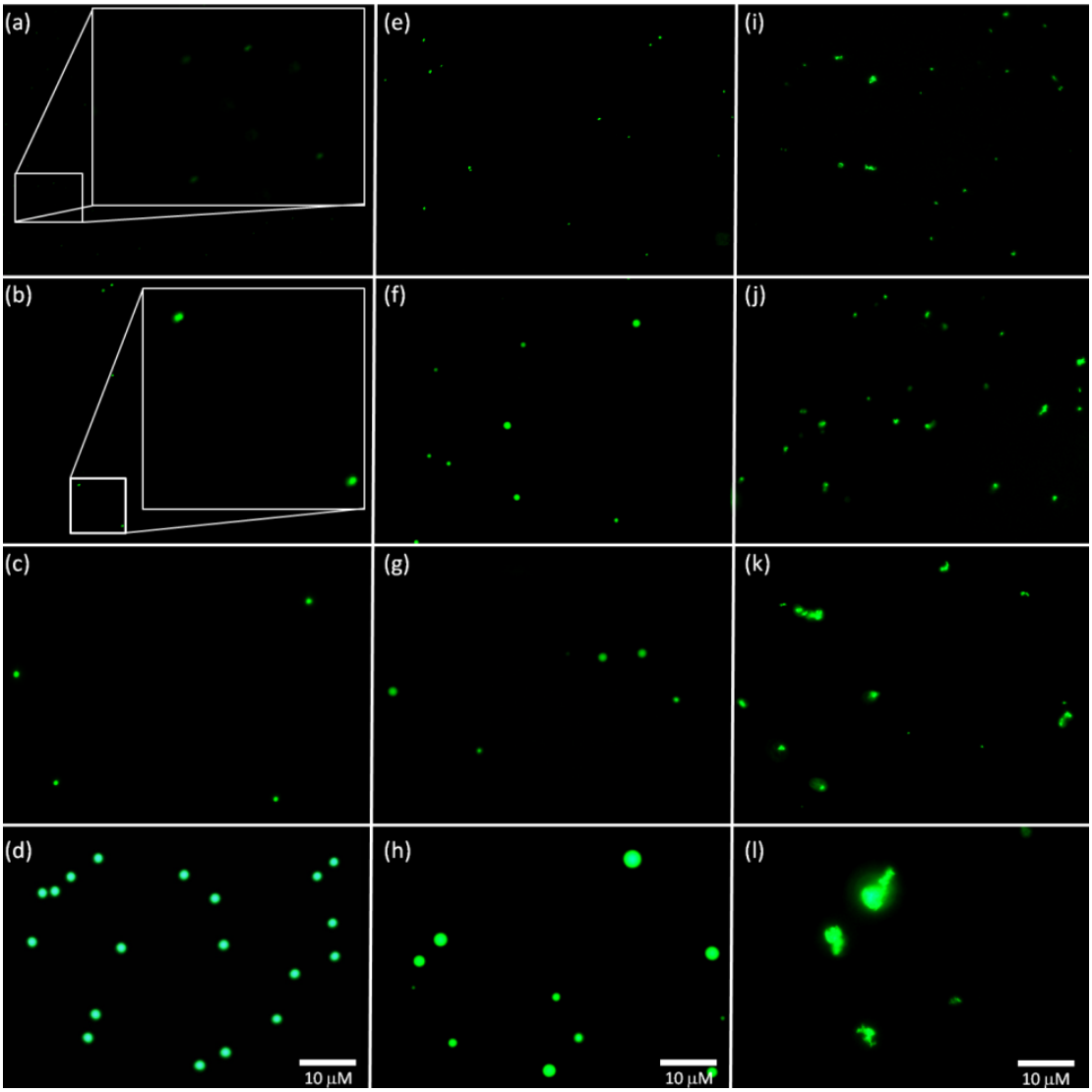

Figure 4.9: Fluorescence micrograph of fluorescently labelled particles and Microbead standards. Protein aggregates were captured after ca. 60 minute incubation (RT). Microbead standards are shown in (a)-(d); (a) 190 nm, inset is a 4x enlargement of selected area, (b) 520 nm, inset is a 4x enlargement of selected area, (c) 1020 nm and (d) 1900 nm. Alexa 488 labelled galectin-3 (A488gal-3, 31 μM) with lactose functionalized dendrimers (0.14 μM) are shown in (e)-(h); (e) A488gal-3 and **1**; (f) A488gal-3 and **2**; (g) A488gal-3 and **3**; (h) A488gal-3 and **4**. FITC labelled Con A (FITC-ConA, 4 μM) with mannose functionalized dendrimers (17 nM are shown in (i)-(l); (i) FITC-ConA and **5**; (j) FITC-ConA and **6**; (k) FITC-ConA and **7**; (l) FITC-ConA and **8**.

Regardless, qualitative comparison of the calculated diameters for lower generations of mannose functionalized dendrimer did not show any distinguishable trend,

while aggregates formed with FITC-Con A and compound **8** appear to be larger (Figure 4.9, l). If the population of small particles mentioned above were excluded from the number average and weighted average diameter, trends of increasing aggregate size might emerge. However, since these results would still be of a very qualitative nature, further analysis was not performed.

The irregular morphology was even more significant for aggregates formed by FITC-labeled streptavidin and generation 6 biotin-functionalized dendrimers (compound **12**, Figure 4.10). The polydispersity of these samples also increased compared to the Con A and mannose functionalized glycodendrimer aggregates. Comparison of the two higher concentrations of compound **12** tested (3:1 and 9:1 excess streptavidin), showed no significant difference in the size or polydispersity of aggregates formed (Figure 4.10, b and c). The highest concentration of compound 12 (Figure 4.10, c) simply displayed a higher density of aggregates. Smaller aggregates were observed for the 220 fold excess streptavidin sample (Figure 4.10, a).

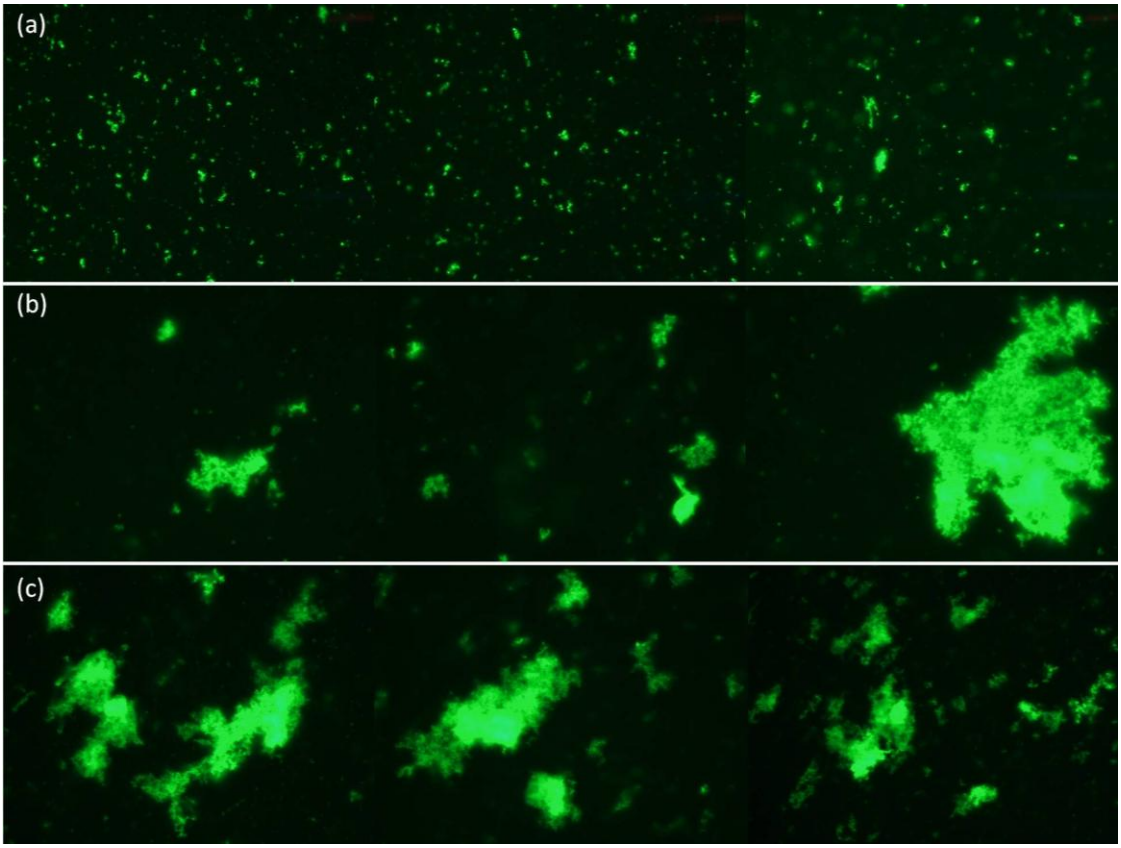

Figure 4.10. Series of 3 images of aggregates for varying ratios of streptavidin-to-biotin dendrimer. (a) 220:1, (b) 9:1, (c) 3:1.

The smaller aggregates observed for the 220:1 streptavidin: biotinylated glycodendrimer could be a result of fewer binding sites available to crosslink nucleation sites, resulting in smaller aggregates. It should also be mentioned that the stock solution of **12** used for the sample containing the lowest concentration of biotinylated glycodendrimer was 10 times lower than the stock concentration of **12** used in the higher concentration samples. Since no distinction in size was observed at higher concentrations of biotinylated glycodendrimer, it is believed that the different stock solutions of compound 12 used is the primary reason for the observed size difference. The strength of the biotin-streptavidin interaction forms immediate crosslinks between the protein and

biotinylated dendrimers creating a complex and unorganized network. Long-term rearrangement of these complexes could not be qualitatively observed for DLS measurements, (Figure 4.18) supporting the hypothesis that aggregates formed by streptavidin and compound **12** are fixed. This hypothesis needs to be verified by using additional biotinylated glycodendrimer stocks at varying concentrations, or evaluating the aggregates formed for the higher concentration biotinylated glycodendrimer samples using the lower concentration stock. If this hypothesis is true, increasing the concentration of biotinylated glycodendrimer will not result in larger aggregates, but rather an increased density of small aggregates.

In summary, the aggregate size of protein/functionalized dendrimer particles appears to depend on both the ability to participate in multivalent interactions, and the concentrations of both protein and functionalized dendrimer present. The increased avidity of streptavidin-biotin and Con A-mannose systems created polydisperse and non-spherical or irregularly shaped particles. The observed characteristics of higher avidity systems suggest less mobility of individual particles within the assembly.

Differences in the monomeric binding affinity of the protein-ligand systems appear to have a lesser affect on the particle morphology and size as compared to the valency of the protein. This statement is supported by the similarities between Con A and streptavidin induced aggregates, and the lack of similarity for Con A and galectin-3 aggregates. The monomeric binding affinity of galectin-3 is similar to the monomeric binding affinity of Con A for mannose. Aggregates of lactose functionalized dendrimers with galectin-3 displayed a regular, spherical shape, and were relatively monodispersed.

The regularity and decreased polydispersity of the galectin-3/lactose functionalized dendrimer aggregates suggest movement of assembly components to a concise and more stable particle, and make it distinct from both Con A and streptavidin systems.

Kinetics

The kinetics of aggregate growth for Con A with mannose functionalized dendrimers could be observed through the uncorrelated light scattering of growing particles. Changes in light scattering during the first 3-5 minutes were observed for small dendrimers (generation 2 and 3, Figure 4.11, a and b, respectively) at high concentrations (110 and 330 nM, Figure 4.11, red and green traces, respectively). At the lowest concentration of glycodendrimer added, only the generation 6 functionalized dendrimer displayed a response in the first five minutes (Figure 4.11, d, blue) The fast kinetics of samples containing higher concentrations of larger glycodendrimers prevented observation of the initial section of the kinetic curve (Figure 4.11, c and d, red and green traces). Generation 2 and 3 glycodendrimers, compounds **5** and **6**, showed increasing aggregation rates with increasing glycodendrimer concentration. Rate enhancements as a result of increasing concentrations could not be evaluated for generation 4 glycodendrimer, compound **7**, since the first part of the curve was not obtained (Figure 4.11, c). The concentration dependence of generation 6 glycodendrimer, compound **8**, showed an initial rate enhancement as the glycodendrimer concentration was increased from 4.5 nM to 110 nM (Figure 4.11, d, blue and red traces, respectively). However, the aggregate rate at 330 nM was less than the aggregation rate at 110 nM (Figure 4.11, d, red and green traces,

respectively). When compared to **7**, the aggregation rate for **8** at both 110 and 330 nM glycodendrimer was reduced. At the lowest concentration of glycodendrimer tested, changes are only observed for generation 6 mannose functionalized dendrimer.

Of particular interest is the shape of the kinetic profile for 110 nM G2- and G3-mannose functionalized dendrimer (Figure 4.11, a and b, red traces). This type of behavior was not observed in previous FLS studies,[48] nor was it reported in a recent publication using real-time surface plasmon resonance measurements to investigate Con A binding kinetics.[107] The lag phase present at early times is typically associated with the rate of formation of nucleation sites. This is followed by a cooperativity phase, characteristically containing an increased rate of aggregate growth. Given that Con-A interactions between oligomers have been observed this second phase may correlate with a complex that allows protein-protein interactions.

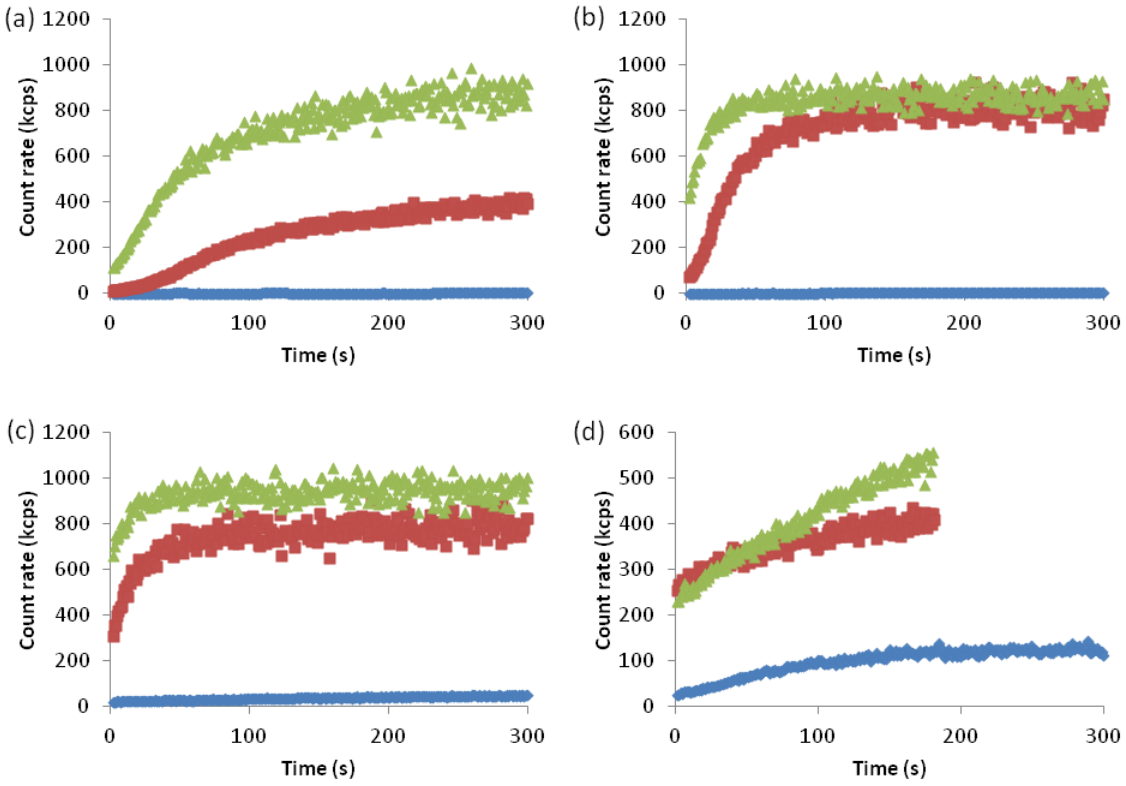

Figure 4.11. Initial five-minute DLS scan following addition of varying concentrations of mannose functionalized dendrimers (4.5 nM, blue; 110 nM, red; 330 nM, green) to Con A (1 μM). (a) Compound **5**, (b) **6**, (c) **7**, (d) **8**.

DLS measurements taken at roughly three minute intervals showed continued growth and increasing polydispersity of aggregates formed with Con A and **8** (Figure 4.12). Enhanced rates and larger aggregates were observed when higher concentrations of both Con A (4 μM compared to 1 μM) and 8 (17 nM compared to 4.5 nM) were tested at the same molar ratio as previous experiments (220 excess Con A).

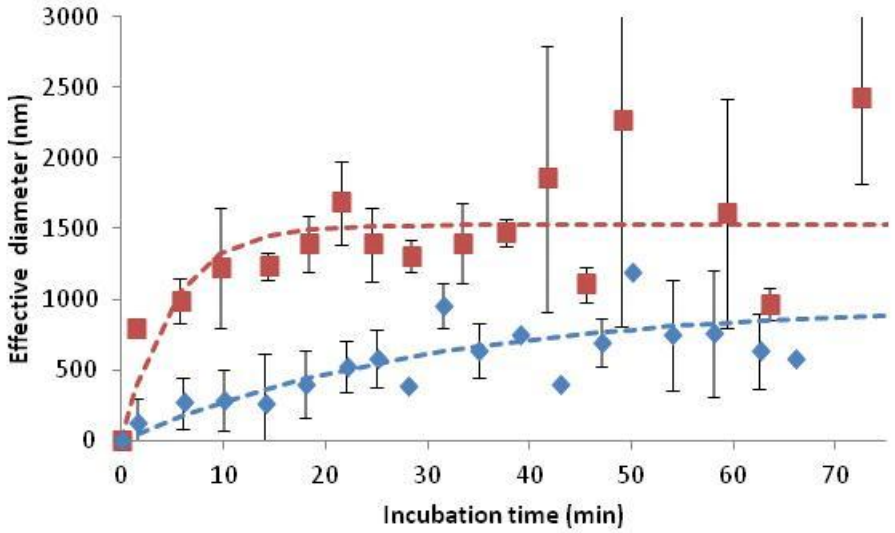

Figure 4.12. Long term kinetics for Con A and compound **8** showing the effect of concentration on aggregate growth. Error bars represent standard deviation of at least duplicate scans of 1 μM Con A + 4.5 nM **8** (blue) and 4 μM Con A + 17 nM **8** (red).

Aggregates formed by Con A/glycodendrimer aggregates were very stable. Collection of DLS and FM data for FITC-labeled Con A with compounds **5**-**8** at 26 hours following glycodendrimer addition show large, polydisperse particles (Figure 4.13 and Table 4.7). Micrographs a-c of Figure 4.13 and numerical results of Table 4.7 show maintenance of the observed trend of increasing size with increasing glycodendrimer generation for compounds **5**-**7**. However, there is a less significant size difference for compounds **7** and **8** after long periods of time (Figure 4.13, c and d). This may indicate that the thermodynamic equilibrium of the protein aggregate, in this case, is independent of the size of the nucleating scaffold, so long as this scaffold permits multivalent interactions. These results suggest that the protein concentration may play a more significant role. Aggregates at time points longer than 26 hours would need to be quantitated to confirm this hypothesis as the trajectory of the smaller glycodendrimer

aggregates is currently unknown. Visual observation indicated that samples stored at room temperature for longer than one week still contained particles.

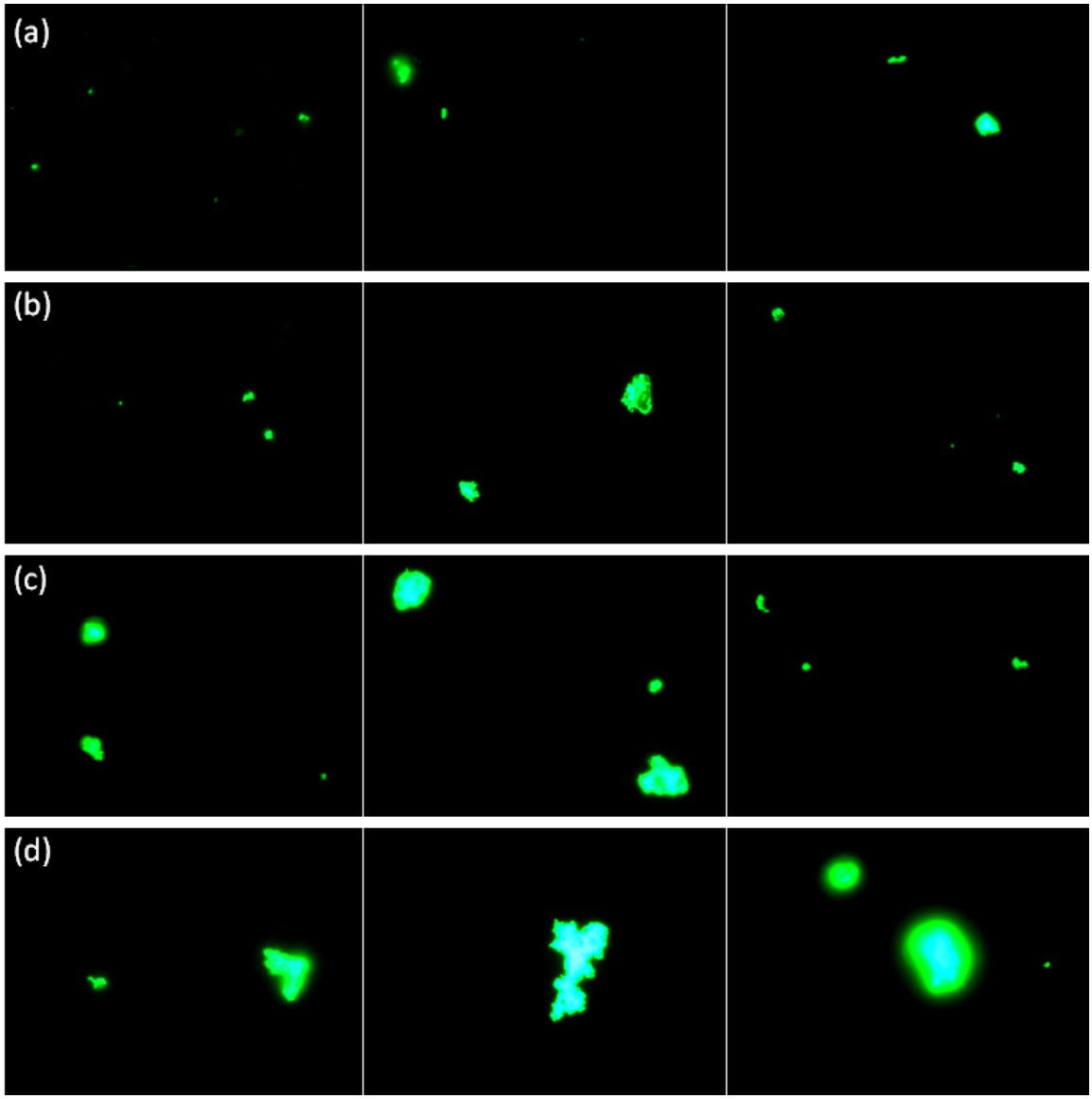

Figure 4.13. Sample of three fluorescent micrographs of Con A (4 μM) + mannose functionalized dendrimers (17nM) at 26 hours following glycodendrimer addition. (a) **5**, (b) **6**, (c) **7**, and (d) **8**. Samples were protected from light and stored at room temperature during incubation period.

Table 4.7. Micrograph characterization of Con A (1 and 4 μM)/mannose functionalized dendrimer aggregates following 26 hour incubation (220× excess Con A)

[Con A]	Compound†	D_{hyd} (nm)*	D_N (nm)	σ D_N (nm)	Rel Var	D_W (nm)	PDI
1μM	**5**	437	505	274	0.54	646	1.3
	6	1475	931	736	0.79	1550	1.7
	7	1743	887	729	0.82	1487	1.7
	8	831	648	463	0.71	1048	1.6
4μM	**5**	ND	1289	1633	1.27	3327	2.6
	6	ND	2893	8269	2.86	25900	9.0
	7	ND	1851	1676	0.91	3363	1.8
	8	1513	4126	5371	1.30	11001	2.7

†Dendrimers were added at 1/220 the concentration of protein
*Standard deviation for all DLS measurements were >200 nm and most were >600 nm meaning numbers presented have little significance.
D_{hyd}=hydrodynamic radius from DLS measurement
D_N=number average diameter
Rel Var = Relative variance = σ/D_N
D_W = weighted average diameter =Σdiameter×frequency; frequency represented as a percent of total particles sampled
PDI=polydispersity index=D_W/D_N
ND=not determined

In contrast to the stability observed for aggregates of Con A/mannose functionalized dendrimers, galectin-3 and lactose functionalized dendrimers appeared to disassemble several hours following glycodendrimer addition. DLS data showed decreasing signals in the first five minute scan (Figure 4.14). There are two possible causes for the observed signal reduction. The aggregates could be combining, producing a smaller number of large aggregates or the aggregates could be disassembling. Analysis of the autocorrelation functions showed increasing aggregate size regardless of glycodendrimer size for several hours (Figure 4.15), suggesting that a smaller number of large particles are forming.

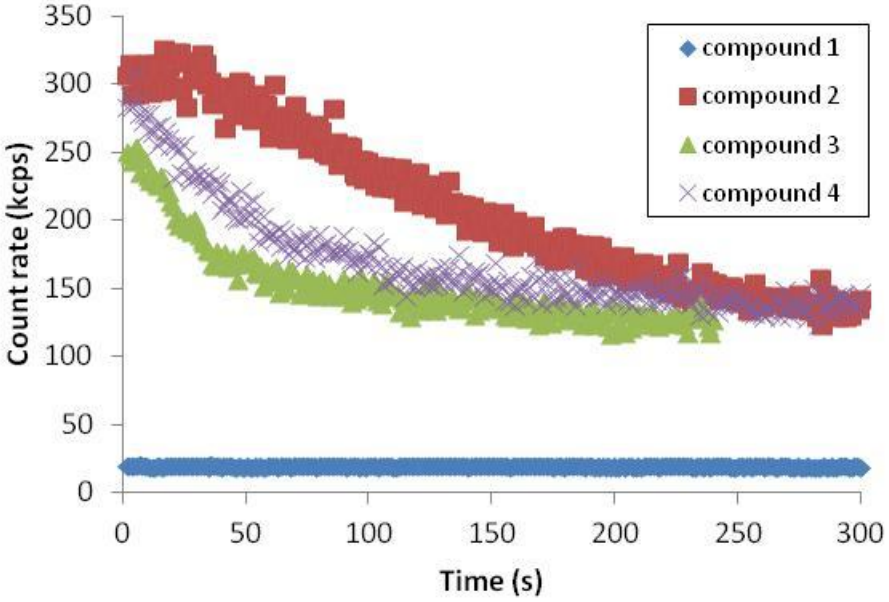

Figure 4.14. Initial five-minute DLS scan following addition of lactose functionalized dendrimers (0.14 μM) to galectin-3 (31 μM). Compound **1** (blue), **2** (red), **3** (green), and **4** (purple). Incident light was adjusted to 200-400 kcps for compounds **2**-**4**.

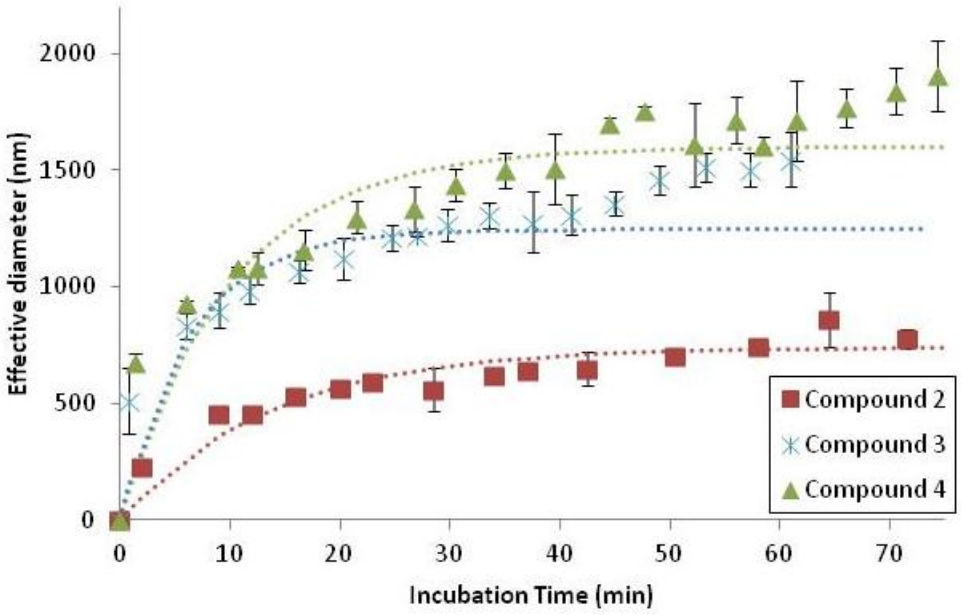

Figure 4.15. One hour kinetic profile for 31 μM galectin-3 + 0.14 μM lactose glycodendrimer compounds **2** (red), **3** (blue), and **4** (green).

However, extended DLS measurements (Figure 4.16) and micrographs taken at 2, 4, 6 and 14 hours following addition of compound **4** provided further evidence for shrinking and disassembly of large particles (Figure 4.17). The initial several hour growth phase was followed by a period of disassembly. Disassembly was supported by the observation of decreasing aggregate diameter of galectin-3 and **4** for both DLS and FM methods.

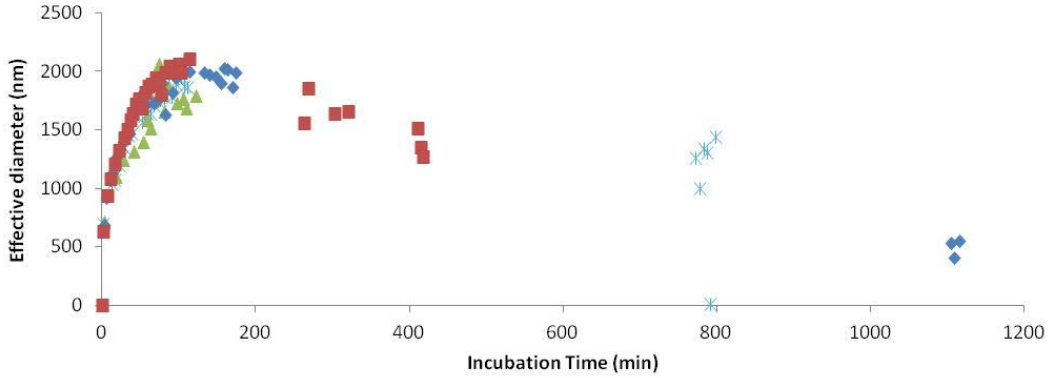

Figure 4.16. Effective diameter of aggregates formed by addition of compound **4** to galectin-3 (different colors represent individual trials).

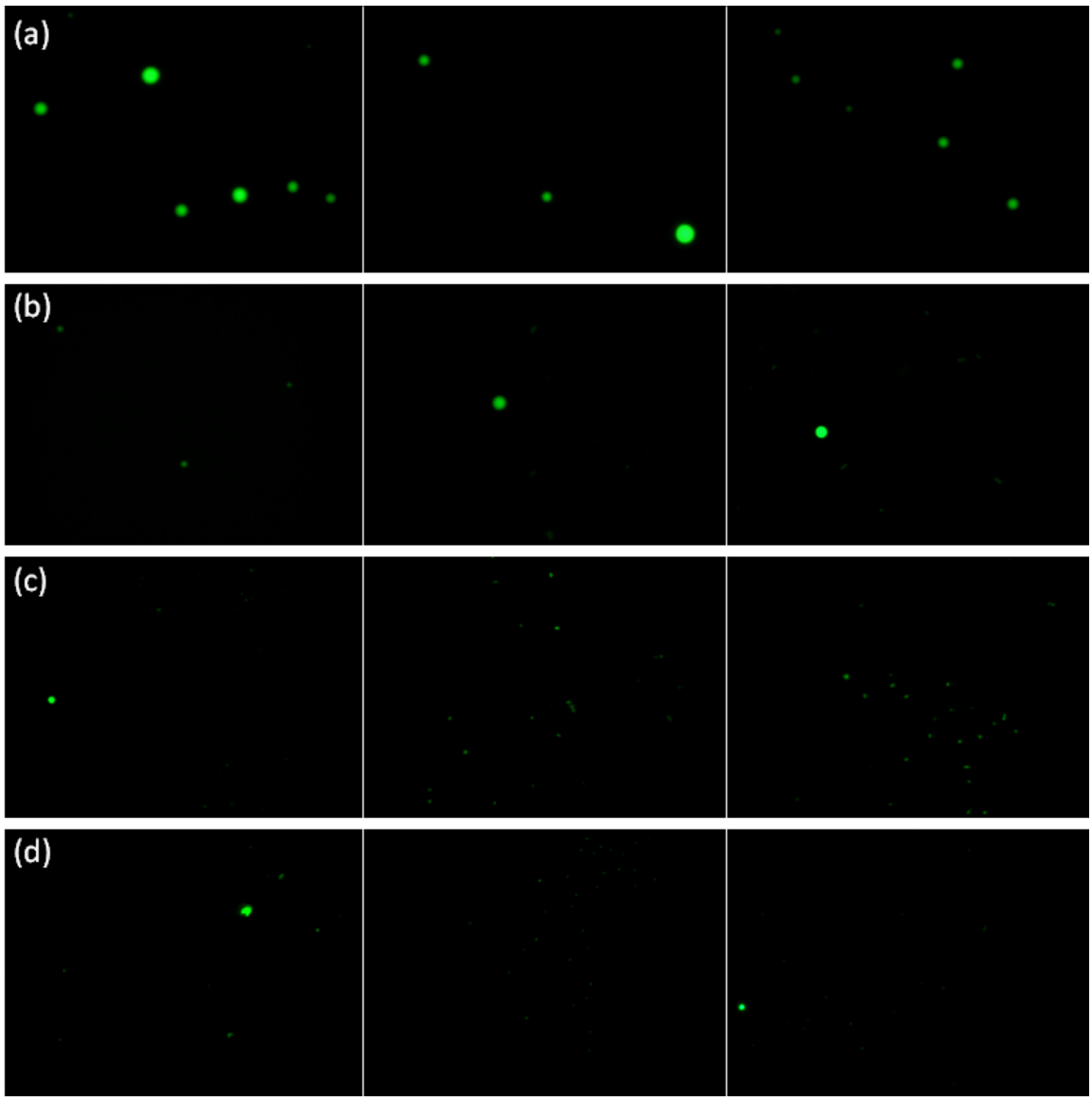

Figure 4.17. Sample of three fluorescent micrographs of galectin-3 + **4** at (a) 2 hours, (b) 6 hours, (c) 14 hours and (d) 26 hours following glycodendrimer addition. Samples were protected from light and stored at room temperature.

Disassembly of galectin-3/glycodendrimer aggregates could be a result of the high entropic cost of ordering the N-terminal domain, thereby restricting its motion. Similar in nature to polyvalent ligands connected by a flexible framework, the enthalpic gain of binding does not, in all cases, compensate for the loss of motion in flexible regions of a

molecule. Whitesides alludes to the consequence of increasing entropy in his statement regarding the design of polyvalent ligands,

> "Incomplete understanding of the entropy in the design of polyvalent molecules that are less effective or only marginally more effective than their monovalent counterparts. The many bivalent systems joined by flexible linkers (e.g. oligo9ethylene glycol) or polymethylene) provide examples of systems that can almost be guaranteed to fail for entropic reasons." [5]

While Whitesides is referring to the entropy of long, flexible linkers between ligands, the same would hold true for oligomeric receptors held together by flexible domains.

Streptavidin and biotinylated glycodendrimers **9**-**12** rapidly formed complex aggregates. The formation of aggregates occurred too rapidly to be characterized by methods employed. Additionally, the highly polydisperse and irregular nature of these aggregates make any quantitative conclusion he nature of this aggregate a simple conjecture. A sample kinetic profile acquired for DLS results is shown for compound **12** and streptavidin at 220 fold excess in Figure 4.18. The large error bars of these data reveal the difficulty of making any type of qualitative or quantitative comparison.

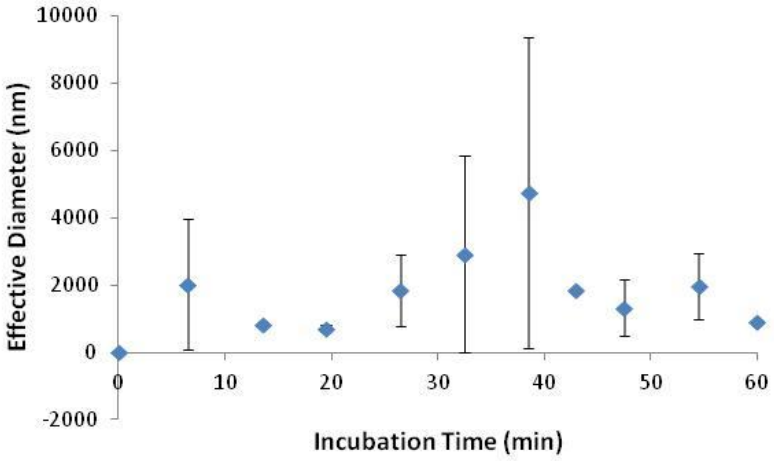

Figure 4.18. One hour kinetic profile for streptavidin (220 fold excess) and compound **12**.

Inhibition

Inhibition of functionalized dendrimer mediated nanoparticles with the monomeric ligand was tracked using DLS. (Figure 4.19) Samples were pre-incubated with monomeric ligand, then glycodendrimer constructs were added and the diameter of the nanoparticles was determined. The alternative method of titrating monomeric ligand into preformed particles could not be used as galectin-3 aggregates are held together weakly, and addition of water alone disrupted the interaction (data not shown).

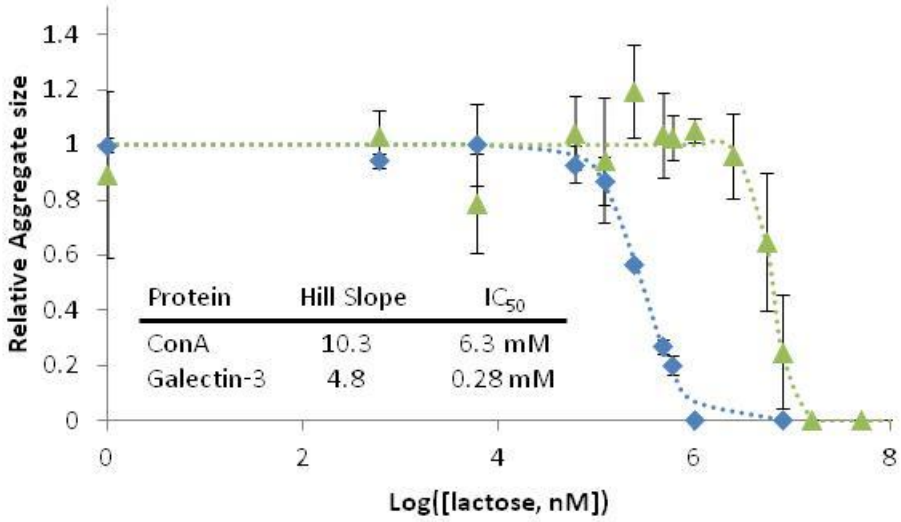

Figure 4.19: Inhibition curves for galectin-3+**4** (blue) and Con A + **8** (green). Data represents average of three scans recorded at 1 hour incubation of triplicate samples.

The IC_{50} of monomeric mannose required to disrupt aggregates of Con-A and **8** was approximately 20 times higher than the monomeric lactose required to disrupt aggregates formed by galectin-3 and **4** (6.5 and 0.28 mM, respectively). Given that these two proteins have comparable affinities for their preferred carbohydrate, the IC_{50} differences were ascribed to the higher valency associated with Con A.

An enhancement factor, β, was introduced by Whitesides, et al. that related the monomeric binding affinity, K^{mono}, to polyvalent binding avidities calculated via ELISA assay, K^{ELISA}, by the following expression:[5]

$$K^{ELISA} = \beta K^{mono} \tag{16}$$

If the IC^{50} value calculated above is considered synonymous to K^{ELISA} then the ratio of β terms for galectin-3 relative to Con A is 0.04, and reflects a less favorable avidity enhancement for the galectin-3 aggregates compared to that of Con A. The lack of

cooperativity for the galectin-3 system likely contributes to the eventual disassembly of these particles. The assumption of a proportional relationship between IC^{50} and K^{ELISA} comes from knowing that both values represent the system where the assay response is half the maximum expected response.

Stoichiometry

The stoichiometric ratios of galectin-3/glycodendrimer aggregates were determined to evaluate the protein clustering ability of the glycodendrimer system. Conventionally, this is done by separating the precipitate through centrifugation, dissolution of the precipitate, and measuring the absorbance at 280 nm to quantitate the amount of protein.[104, 108] This was not possible for the galectin-3 system studied. The particles were too small and the centrifugal force required to pellet exceeded the ability of available equipment. An alternative method was designed to filter the precipitate after an hour incubation and quantitate both protein and glycodendrimer components of the filtrate using UV-Vis spectra.

Experimental

Galectin-3 glycodendrimer nanoparticles of varying size spontaneously assembled upon mixing with compounds **1**-**4** (0.14, 3.4 and 11.5 μM) with galectin-3 (31 μM). DLS and microscopy results show that for compounds **2**-**4** a majority of these particles exceed 400 nm, suggesting filtration with a 220 nm pore size diameter should be efficient means to separate aggregates. Following incubation at room temperature for 1 hour, nanoparticles were removed by filtration with 0.22 μm Millipore syringe tip filters

(PVDF, 4 mm diameter). Particles were then disassembled and washed from filter with β-lactose (300 μL, 10 mM, washed over filter 3 times). UV-Vis spectra (190 nm-350 nm, SpectraMax Plus 384, Molecular Devices) were recorded for the pre-filtered solution, filtrate and lactose wash. These spectra were fit to predetermined glycodendrimer and galectin-3 spectra using a least squares method to determine the stoichiometric ratio.

Precipitation Assay Results and Discussion

The figure below compares the area normalized glycodendrimer and galetin-3 UV-Vis spectra. The spectral shapes were concentration independent for the range listed (Figure 4.20). Molar extinction coefficients for galectin-3 and glycodendrimers were calculated from the slope of absorbance versus concentration plot at 240 nm (Figure 4.21, top) and 280 nm (Figure 4.21, bottom).

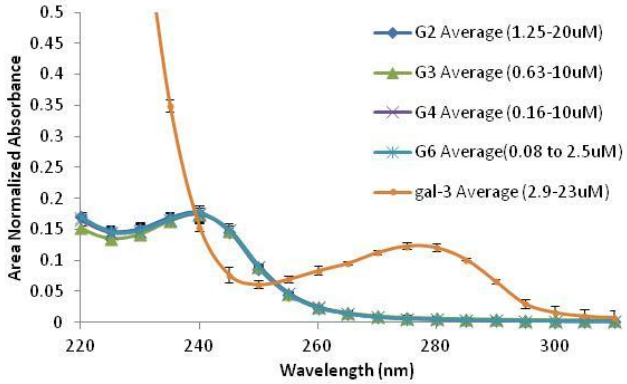

Figure 4.20. UV-Vis spectra of lactose functionalized dendrimer and galectin-3 samples. Error bars represent 3σ of 3-7 spectra

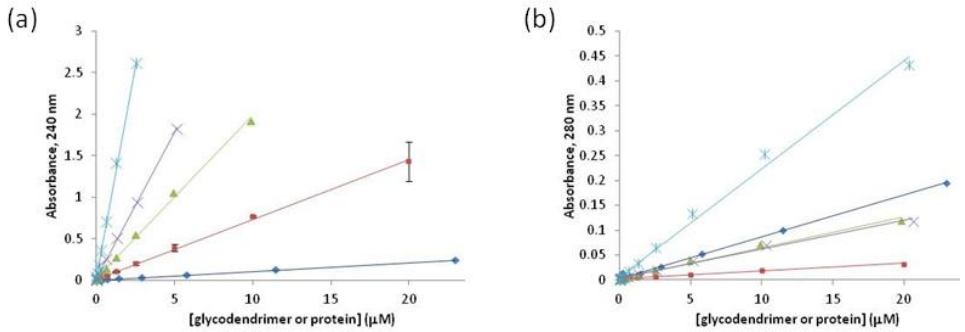

Figure 4.21. Absorbance standard curves for galectin-3 (blue diamonds), **1** (red squares), **2** (green triangles), **3** (purple crosses), **4** (blue crosses) at (a) 240 nm and (b) 280 nm.

Quantization of galectin-3 and glycodendrimer aggregates was done via fitting UV-Vis data for the lactose wash with the above spectra using equation (16), as shown in Figure 4.22. The coefficients, *D* and *G* correspond to relative amounts of glycodendrimer and galectin-3, respectively. The coefficients were converted to molar concentrations using the determined molar extinction coefficient (Table 4.8) before calculating the ratio of galectin-3-to-glycodendrimer (Table 4.9).

$$A_s(\lambda) = DA_d(\lambda) + GA_g(\lambda) \tag{16}$$

Here, A_s is the measured absorbance spectra of the glycodendrimer/galecin-3 sample, A_d and A_g are the dendrimer and galectin-3 spectrum, respectively, *D* is a scalar representing the relative amount of glycodendrimer, and *G* is a scalar representing the relative amount of galectin-3. Sample spectra with fits are shown in Figure 4.22.

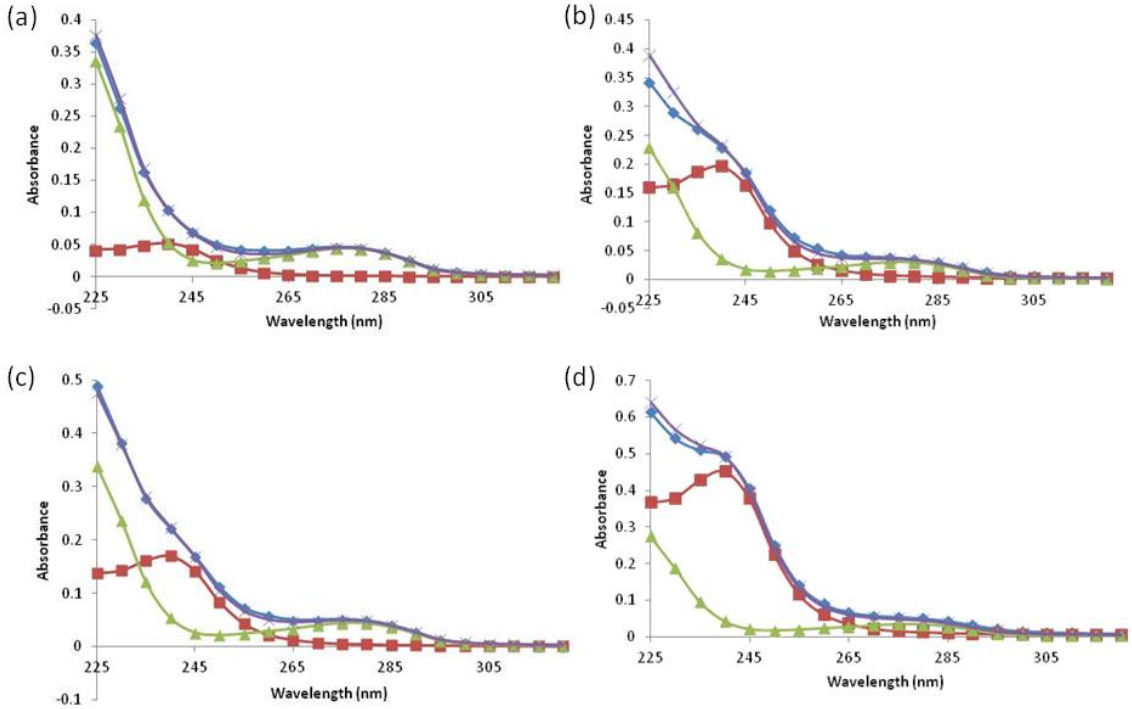

Figure 4.22. Sample-fitted spectra for the lactose wash of galectin-3 and 3.4 μM (a) Galectin-3 + **1**, (b) Galectin-3 + **2**, (c) Galectin-3 + **3**, and (d) Galectin-3 + **4** glycodendrimer added. Measured data (blue squares), fitted data (purple crosses), glycodendrimer component (red squares), and galectin-3 component (green triangle).

This process worked well for samples where an appreciable amount of signal could be observed for both components. When one component was in large excess, as in the case with aggregates formed by galectin-3 and 11.5 μM **4**, the minor component could not be determined confidently (Table 4.9). Use of an extrinsic fluorophore to label the minor component should provide the sensitivity needed to circumvent this problem.

Table 4.8: Molar extinction coefficients

Sample	$\epsilon_{240\ nm}$ ($M^{-1}cm^{-1}$)	$\epsilon_{280\ nm}$ ($M^{-1}cm^{-1}$)
1	151000	2700
2	435000	15700
3	747000	15200
4	2256000	51600
Galectin-3	22400	18000

Table 4.9: Calculated stoichiometric ratio of galectin-3:glycodendrimer

Sample	[dendrimer] (μM)		
	0.014	3.4	11.5
1	23 ± 3	9 ± 5	3 ± 0.6
2	32 ± 15	11 ± 2	5 ± 1.6
3	56 ± 17	12 ± 2	3 ± 1.3
4	57 ± 8	12 ± 3	ND

The stoichiometric ratios of galectin-3 and lactose functionalized aggregates that were determined by the method described above are shown in Tables 4.9. Samples containing lower stoichiometric ratios of galectin-3-to-glycodendrimer (3:1 and 9:1 stoichiometric excess of galectin-3) revealed similar stoichiometries to the sample makeup within the aggregate. In other words, the average number of galectin-3 molecules in the nanoparticles was equivalent to the ratio of excess galectin-3 molecules in solution. This was not the case for samples containing a large excess of galectin-3 relative to the glycodendrimer scaffold. All calculated stoichiometries for aggregates formed in the presence of 220 molar excess galectin-3 were substantially less than 220. As expected, an increasing trend in the stoichiometric ratio of galectin-3-to-glycodendrimer was observed with increasing glycodendrimer size for compounds **1**-**3**. This shows that the larger the molecular scaffold, the greater number of entities that can bind to the scaffold.

Interestingly, the saturation value of galectin-3 for compounds **4** and **6** were similar. There are two possible explanations for the saturation of galectin-3 molecules with glycodendrimer size for **4** and **6**. The first is that even though total surface area of **6** is approximately 2 fold higher than the surface area of **4**, the thermodynamically favored equilibrium state at 1 hour is similar for both **4** and **6**. The kinetics of galectin-3 and **6** aggregates are fastest for this generation of glycodendrimer, increasing the likelihood of disordered nucleation sites. This could create a situation where multiple carbohydrate endgroups are unbound within the core of the aggregate, resulting in a lower than expected stoichiometric ratio.

Another possibility is that electrostatic repulsion is greater for galectin-3 with **6**. For most lactose functionalized dendrimers, the remaining, unfunctionalized amines account for roughly 25% of the total number of endgroups. However, in the functionalized G6 construct, approximately half of the terminal amines remain. The pI of galectin-3, calculated using EXPASY was determined to be 8.6, suggesting the protein contains an overall positive charge under the solution conditions of the experiment. The increasingly positive surface of **6** compared to lower generations of lactose functionalized dendrimers exerts a larger repulsive force on the bound galectin-3 molecules. Lactose functionalized dendrimers efficiently interacted with negatively charged dodecylsulfate molecules and could be pulled through an SDS polyacrylamide gel (data not shown). This partially supports the idea of a positively charged surface for lactose functionalized dendrimers. This hypothesis could also be confirmed by evaluating the surface charge of both galectin-3 and glycodendrimer components via zeta-potential measurements.

Summary Comparison of Protein Aggregates

The quaternary structure of a protein is likely to impact the nanoparticle formed via PAMAM scaffold mediated protein aggregation. The quaternary structures of Con A and streptavidin are similar in that both are tetrahedral, while galectin-3 is most likely a dimer or a less defined oligomer. Thus, direct comparisons between Con A and streptavidin were made to determine the affect of the monovalent binding association on assemblage.

Similarities in the particle morphology and polydispersity for Con A and streptavidin systems suggest that the enhanced avidity of higher order oligomer systems causes irregular morphology and increased polydispersities. The increased oligomeric state of the protein creates a higher valency system, assuming each binding site remains accessible upon oligomerization. This enhanced avidity resulted in slower moving (Con A and mannose glycodendrimer) and even stagnant (streptavidin and biotinylated glycodendrimer) assemblies.

The most notable difference between streptavidin and Con A systems was observed in the kinetics of aggregate assembly. The 100 billion fold enhanced monomeric binding affinity of streptavidin relative to Con A resulting in dramatically increased aggregation rates. Streptavidin and biotin functionalized dendrimer aggregates formed instantaneously while Con A and mannose functionalized dendrimers continued to grow for at least 26 hours.

Galectin-3 and Con A, on the other hand, have similar binding affinity but different valencies, making their comparison quite useful to determine the affect of the

valency and binding site orientation on aggregation. There appears to be a fast and slow process for galectin-3 and Con-A systems. This has been previously modeled via SPR measurements of immobilized Con A with mannosyl and glucosyl decorated 2-4th generation gallic acid−triethylene glycol dendrimers.[107] These authors ascribe the rapid initial association to the initial sugar-binding event which was enhanced for generation 3 and 4 glycodendrimers. The slower second phase has been attributed to the rearrangement of these aggregates. Continual growth was also observed for Con A.

Galectin-3 and lactose functionalized aggregates appeared to form more rapidly than Con A and mannose functionalized aggregates. Rather than continually growing, galectin-3/glycodendrimer aggregates appear to undergo an initial growth phase followed with eventual denucleation and dissolution. The cause of the disassembly process is currently unknown, and further studies will need to be done to characterize the assembly with time.

CHAPTER 5

IMPLICATIONS OF MONOVALENT BINDING AND VALENCY ON AGGREGATION BEHAVIOR: OVERARCHING SUMMARY AND FUTURE INVESTIGATIONS

The ability to understand and manipulate polyvalent interactions would allow us to control diseases where polyvalent interactions result in catastrophe. In many cases, the catastrophe comes in the form of crosslinking between entities resulting in aggregation. Aggregation prevents the protein from functioning properly, and sometimes these aggregates cannot be broken down by conventional, physiological means. The first step to control these systems or to create systems that interfere with these processes is characterization. There are two aggregation phenomena that would be useful if characterized. The first being the forces driving the interaction, and the second being the identification of assembly progression. In other words, it would be desirable to know what conditions contribute to cause nucleation, and does particle growth occur through monomer addition or combination of nuclei. PAMAM dendrimers offer a tunable and characteristically favorable scaffold that can be used in understanding the significance of forces involved in particle formation.

Particle Growth Theory

The process of molecular assembly to form nanoparticles is a topic of debate and appears to depend on the individual conditions of each system. Classical nucleation theory describes an initial nucleation event where free monomers come together to form nuclei. Nuclei act as an activated state once reaching a critical size, and the instability of

the activated state results in growth to a thermodynamically equilibrated state. Aggregates smaller than the critical size are unstable and disassemble to their monomer form.[109] The particles larger than the critical size are stabilized by reduction of the overall surface area-to-volume ratio. A single large aggregate, whose volume is equal to the sum of the volumes of several smaller particles, has a smaller exposed surface area compared to the total surface area of the smaller particles. The interfacial curvature of the solid to liquid phase is greater for large particles resulting in lower stress and a lower energy system. The process of particle assembly to reduce the overall interfacial volume is known as Ostwald ripening, and typically increases the heterogeneity of the sample. [110] While classical nucleation theory cannot provide accurate descriptions of the kinetic processes of nanoparticle formation, it is capable of predicting the steady-state conditions required for monodispersed nanoparticles.[105] Particle growth kinetics have been modeled under the assumption that growth results due to the addition of monomers to the nucleation site.[29] Data is fit using monomer association and dissociation rates. Most equations modeling monomer addition include nucleation parameters, or an additional term describing the nucleation event. However, some models such as the reversible association model used by Eisenberg, *et al*. and Thusius, *et al.* only consider the concentration of protein in monomer and polymer forms.[111-113]

The critical nucleation size and nucleation rate of the system are dependent on the attractive and repulsive intermolecular forces of the system. These forces include charge based interactions, hydrogen bonding, dipole-dipole or dipole-induced interactions (van der Waals), and interactions due to the hydrophobic effect. Particle growth depends on

the attractive forces of the system compensating for and overcoming the repulsive forces of the systems. While all interactions have the possibility of occurring for each component, the relative strength of the interaction determines its contribution to the overall system. In other words, some of these interactions may be too weak to be considered relevant. For example, in the DVLO model ranks van der Waals, charge and "acid-base" interactions as the most significant interactions. The DVLO model for molecular colloidal adhesion defines the spontaneity of assemblage using a free energy term. The free energy is a combination of van der Waals interactions (ΔG^{vdW}), charge based interactions (ΔG^{dl}) and "acid-base" interactions (ΔG^{AB}).*109*

Use of Dendrimers to Understand Forces Involved in Particle Assembly

The studies herein use functionalized dendrimers as nucleation sites. The dendrimer acts as a stability factor in the aggregate assembly. Additional attractive forces occur between protein and functionalized dendrimer to force protein molecules in close proximity. Characteristically, these aggregates may or may not reflect protein aggregation in the cellular environment because the aggregates created are heterogeneous ensembles of dendrimer and protein entities, but they are realistic of protein interactions at the cell surface environment. At the cellular surface, proteins can be post-translationally modified to contain multiple epitopes of a single molecule, one example being polyglycated membrane proteins.

The process of molecules coming together, interacting in a multivalent fashion, and then assembling into a nanoparticle is driven by attractive forces. The first event is

the monomeric binding event, which is closely followed by a multivalent binding event, so long as the proximity of ligands allow binding to multiple receptors. The strength of the multivalent event, determines the time two entities are associated with one another, and depend on the valency of the components.

Dendrimer Effects on Particle Growth

In theory, the use of functionalized dendrimers to mediate protein aggregates could facilitate or adversely affect the nucleation event. Functionalized dendrimers were designed to provide a scaffold that has affinity for the protein counterparts. Therefore, the functionalized dendrimers have the ability to recruit proteins, bring them into close proximity, and possibly induce protein-protein interactions. The degree of attraction is determined through the mono- and polyvalent interactions between scaffold and protein (see section Assembly Progression in terms of Binding in Chapter 1 for more information on polyvalent binding). The nucleation ability would depend on the competition between protein-protein interactions and protein-ligand interactions of the functionalized dendrimer/protein environment. When both the protein-ligand and protein-protein interactions are cooperative then the functionalized dendrimers could serve to enhance nucleation. In this situation, the functionalized dendrimer would effectively recruit proteins, then these proteins could interact with one another to create a higher valency receptor. The increased valency would enhance the overall avidity between the protein "cluster" and functionalized dendrimer, and increase the interaction time. Increasing the interaction time would increase the probability for additional proteins to dock to the glycodendrimer scaffold and interact with the protein "cluster". This cycle could continue

until either all available protein has been complexed, or until equilibrium between complexed and free protein is achieved.

There is also the possibility of functionalized dendrimer constructs to negatively affect nucleation rate. In this scenario, the protein-ligand interaction must be more favorable than the enhanced avidity observed as a consequence of protein-protein interactions. The forces holding protein oligomers together are less favorable than the energy of protein-ligand binding. Therefore, the probability of nucleation is decreased when the system contains an excess of ligated scaffolds and the protein-protein interactions are weak.

Contributions of Monomeric Binding Constant, Valency and Charge on Aggregate Formation

The monovalent interaction dominates and the mobility of entities within a molecular assembly is lost in cases where the monovalent association constant is very high. Loss of mobility was also observed for systems of increased avidity as a result of multivalent interactions. The greater the number of interactions that occur to hold molecules together, the higher the avidity and the longer the two are associated.

The structure of Con A and streptavidin aggregates formed in the presence of polyvalent dendrimer constructs were polydisperse and morphologically irregular. An extensive network of protein-glycodendrimer complexes resulted when increasing nucleation sites were made available. The primary difference observed between streptavidin and Con A aggregates was the rate at which they formed. Aggregates of Streptavidin and biotin functionalized dendrimers formed rapidly, and either did not

require a nucleation event or the nucleation event occurred to quickly to be observed. Classical polymerization appeared true for the Con A and mannose functionalized dendrimer system. A lag period was observed in which the mannose functionalized dendrimers facilitated Con A nucleation, and based on the aggregate morphology, the nucleation sites combined in the growing aggregate. Even though the monovalent binding affinity of Con A for mannose would suggest possible rearrangement of the particles, the enhanced avidity due to multivalent interactions between Con A and mannose functionalized dendrimers appears to prevent any particle rearrangement.

Galectin-3 and Con A have similar monomeric binding affinities yet exist at distinct oligomeric states. Comparing galectin-3 and Con A systems reveal the importance of the valency of the system. Results showed that glycodendrimer induced Con A aggregates were slower to form but had superior stability, while galectin-3 aggregates formed very quickly but disappeared over time.

For the Con A system, it is speculated that the charge based interactions are attractive under the experimental conditions of the experiment. The dendrimers are expected to have an overall positive charge, based on the pKa of the unlabeled terminal amines. Con A tetramers are expected to be slightly negatively charged based on the calculated pI of the protein. There is the possibility of reducing the avidity by altering the charge of either component of the system. Altering the charge of the Con A tetramer could be done by changing the buffer system used. However, Con A is known to dimerize at pH values below 5.[10] Therefore it would be easier to modify the glycodendrimer system to create either a neutral or negatively charges species to investigate the role of the

charge based interactions. The charge of the PAMAM dendrimers could be moderated by capping the terminal amines with a neutral tether.

Dendrimers in Disease Control

Dendritic, multivalent systems provide a method of targeting, drug delivery, and ultimately disease control. The disease can be pathogen-based or amyloidogenic. In pathogen-based diseases the enhanced avidity of multivalent frameworks provides a means of higher specificity in binding (detecting pathogens). In amyloidogenic diseases, multivalency offers a means to break up and interfere with the amyloidogenic process, ultimately preventing aggregation. The multivalent scaffolds developed must have certain characteristics in order to be FDA approved. The scaffold must be non-toxic, soluble, effective, show minimal interference, and must be eventually excreted. PAMAM dendrimers have been shown to contain many of these properties depending on the exterior functionalization. Additionally, PAMAM dendrimers are systematically grown using a two-step synthesis procedure creating a tunable and regular framework.

Significance of Lectin-Carbohydrate Interactions

Patterns of cell-surface carbohydrates change during development, differentiation, oncogenesis and metastasis. These changes are believed to be involved in signaling pathways and cell recognition. A link exists between binding to specific glycans and the resulting signaling response. Characteristically, monomers binding to these carbohydrate components are weak and non-specific. Polyvalency is one mechanism that is used in nature to increase the binding affinity or avidity of protein carbohydrate interactions, but

polyvalency does not explain the specificity of the interaction. The specificity, and resulting signaling response, may arise from the protein-protein interactions that occur after the carbohydrate-docking event. In other words, the carbohydrates act as a nucleation site enabling proteins to come together. The polyvalency of glycan-containing scaffolds amplifies binding making the interaction specific and causing a specific biological response. This type of interaction is commonly seen in pathogen and cell recognition and the immune response. Using tunable glycodendrimers to mimic this environment provides a mechanism to study carbohydrate mediated interactions.

REFERENCES CITED

1. Amano, T., Nakamizo, A., Mishra, S. K., Gumin, J., Shinojima, N., Sawaya, R., and Lang, F. F. (2009) Simultaneous phosphorylation of p53 at serine 15 and 20 induces apoptosis in human glioma cells by increasing expression of pro-apoptotic genes, *Journal of Neuro-Oncology 92*, 357-371.

2. Ferrero, M., Ferragud, J., Orlando, L., Valero, L., del Pino, M. S., Farras, R., and de Mora, J. F. (2011) Phosphorylation of AIB1 at Mitosis Is Regulated by CDK1/CYCLIN B, *Plos One 6*, 12.

3. Olsen, J. V., Blagoev, B., Gnad, F., Macek, B., Kumar, C., Mortensen, P., and Mann, M. (2006) Global, in vivo, and site-specific phosphorylation dynamics in signaling networks, *Cell 127*, 635-648.

4. Ali, M. H., and Imperiali, B. (2005) Protein oligomerization: How and why, *Bioorganic & Medicinal Chemistry 13*, 5013-5020.

5. Mammen, M., Choi, S. K., and Whitesides, G. M. (1998) Polyvalent interactions in biological systems: Implications for design and use of multivalent ligands and inhibitors, *Angewandte Chemie-International Edition 37*, 2755-2794.

6. Klyosov, A., Vitczak, Z., and Platt, D. (2008) *Galectins*, John Wiley & Sons, Inc., New Jersey.

7. Woller, E. K., and Cloninger, M. J. (2002) The lectin-binding properties of six generations of mannose-functionalized dendrimers, *Organic Letters 4*, 7-10.

8. Wolfenden, M. L., and Cloninger, M. J. (2005) Mannose/glucose-functionalized dendrimers to investigate the predictable tunability of multivalent interactions, *Journal of the American Chemical Society 127*, 12168-12169.

9. Gestwicki, J. E., Cairo, C. W., Strong, L. E., Oetjen, K. A., and Kiessling, L. L. (2002) Influencing receptor-ligand binding mechanisms with multivalent ligand architecture, *Journal of the American Chemical Society 124*, 14922-14933.

10. Mangold, S. L., and Cloninger, M. J. (2006) Binding of monomeric and dimeric Concanavalin A to mannose-functionalized dendrimers, *Organic & Biomolecular Chemistry 4*, 2458-2465.

11. Kiessling, L. L., Gestwicki, J. E., and Strong, L. E. (2000) Synthetic multivalent ligands in the exploration of cell-surface interactions, *Current Opinion in Chemical Biology 4*, 696-703.

12. Levental, K. R., Yu, H., Kass, L., Lakins, J. N., Egeblad, M., Erler, J. T., Fong, S. F. T., Csiszar, K., Giaccia, A., Weninger, W., Yamauchi, M., Gasser, D. L., and Weaver, V. M. (2009) Matrix Crosslinking Forces Tumor Progression by Enhancing Integrin Signaling, *Cell 139*, 891-906.

13. Green, D. E., and Perdue, J. F. (1966) Membranes as Expressions of Repeating Units, *Proceedings of the National Academy of Sciences of the United States of America 55*, 1295-&.

14. Varki, A. (1993) Biological Roles of Oligosaccharides - All of the Theories are Correct, *Glycobiology 3*, 97-130.

15. Niv, Y. (2008) MUC1 and colorectal cancer pathophysiology considerations, *World Journal of Gastroenterology 14*, 2139-2141.

16. Kotera, Y., Fontenot, J. D., Pecher, G., Metzgar, R. S., and Finn, O. J. (1994) Humoral Immunity Against a Tandem Repeat Epitope of Human Mucin MUC-1 in Sera from Breast, Pancreatic, and Colon-Cancer Patients, *Cancer Research 54*, 2856-2860.

17. Arcinas, A., Yen, T. Y., Kebebew, E., and Macher, B. A. (2009) Cell Surface and Secreted Protein Profiles of Human Thyroid Cancer Cell Lines Reveal Distinct Glycoprotein Patterns, *Journal of Proteome Research 8*, 3958-3968.

18. Lalonde, S., Ehrhardt, D. W., Loque, D., Chen, J., Rhee, S. Y., and Frommer, W. B. (2008) Molecular and cellular approaches for the detection of protein-protein interactions: latest techniques and current limitations, *Plant Journal 53*, 610-635.

19. Kumar, S., Ma, B. Y., Tsai, C. J., Sinha, N., and Nussinov, R. (2000) Folding and binding cascades: Dynamic landscapes and population shifts, *Protein Science 9*, 10-19.

20. Ma, B. Y., Kumar, S., Tsai, C. J., and Nussinov, R. (1999) Folding funnels and binding mechanisms, *Protein Engineering 12*, 713-720.

21. Tsai, C. J., Kumar, S., Ma, B. Y., and Nussinov, R. (1999) Folding funnels, binding funnels, and protein function, *Protein Science 8*, 1181-1190.

22. Simons, K., and Toomre, D. (2000) Lipid rafts and signal transduction, *Nature Reviews Molecular Cell Biology 1*, 31-39.

23. Fink, A. L. (1998) Protein aggregation: folding aggregates, inclusion bodies and amyloid, *Folding & Design 3*, R9-R23.

24. Vasan, S., Foiles, P., and Founds, H. (2003) Therapeutic potential of breakers of advanced glycation end product-protein crosslinks, *Archives of Biochemistry and Biophysics 419*, 89-96.

25. Lee, A. S., Galea, C., DiGiammarino, E. L., Jun, B., Murti, G., Ribeiro, R. C., Zambetti, G., Schultz, C. P., and Kriwacki, R. W. (2003) Reversible amyloid

formation by the p53 tetramerization domain and a cancer-associated mutant, *Journal of Molecular Biology 327*, 699-709.

26. Newkome, G. R., Moorefield, C. N., and Vögtle, F. (2001) *Dendrimers and dendrons : concepts, syntheses, applications*, Wiley-VCH, Weinheim ; New York.

27. Cloninger, M. J. (2002) Biological applications of dendrimers, *Current Opinion in Chemical Biology 6*, 742-748.

28. Lee, C. C., MacKay, J. A., Frechet, J. M. J., and Szoka, F. C. (2005) Designing dendrimers for biological applications, *Nature Biotechnology 23*, 1517-1526.

29. Morris, A. M., Watzky, M. A., and Finke, R. G. (2009) Protein aggregation kinetics, mechanism, and curve-fitting: A review of the literature, *Biochimica Et Biophysica Acta-Proteins and Proteomics 1794*, 375-397.

30. Klajnert, B., Cortijo-Arellano, M., Cladera, J., and Bryszewska, M. (2006) Influence of dendrimer's structure on its activity against amyloid fibril formation, *Biochemical and Biophysical Research Communications 345*, 21-28.

31. Demeule, B., Gurny, R., and Arvinte, T. (2007) Detection and characterization of protein aggregates by fluorescence microscopy, *International Journal of Pharmaceutics 329*, 37-45.

32. Bhat, S. A., and Bano, B. (2014) Conformational behaviour and aggregation of chickpea cystatin in trifluoroethanol: Effects of epicatechin and tannic acid, *Archives of biochemistry and biophysics 562*, 51-61.

33. Hawe, A., Sutter, M., and Jiskoot, W. (2008) Extrinsic fluorescent dyes as tools for protein characterization, *Pharmaceutical Research 25*, 1487-1499.

34. Michel, A. K., Nangia-Makker, P., Raz, A., and Cloninger, M. J. (2014) Lactose-Functionalized Dendrimers Arbitrate the Interaction of Galectin-3/MUC1 Mediated Cancer Cellular Aggregation, *Chembiochem : a European journal of chemical biology 15*, 2106-2112.

35. Giepmans, B. N. G., Adams, S. R., Ellisman, M. H., and Tsien, R. Y. (2006) Review - The fluorescent toolbox for assessing protein location and function, *Science 312*, 217-224.

36. Roding, M., Deschout, H., Braeckmans, K., and Rudemo, M. (2013) Measuring absolute nanoparticle number concentrations from particle count time series, *Journal of Microscopy 251*, 19-26.

37. Cheng, S. H., Li, F. C., Souris, J. S., Yang, C. S., Tseng, F. G., Lee, H. S., Chen, C. T., Dong, C. Y., and Lo, L. W. (2012) Visualizing Dynamics of Sub-Hepatic

Distribution of Nanoparticles Using Intravital Multiphoton Fluorescence Microscopy, *Acs Nano 6*, 4122-4131.

38. Pecora, R. (2000) Dynamic light scattering measurement of nanometer particles in liquids, *Journal of Nanoparticle Research 2*, 123-131.

39. Panacek, A., Kvitek, L., Prucek, R., Kolar, M., Vecerova, R., Pizurova, N., Sharma, V. K., Nevecna, T., and Zboril, R. (2006) Silver colloid nanoparticles: Synthesis, characterization, and their antibacterial activity, *Journal of Physical Chemistry B 110*, 16248-16253.

40. Lynn, D. M., and Langer, R. (2000) Degradable poly(beta-amino esters): Synthesis, characterization, and self-assembly with plasmid DNA, *Journal of the American Chemical Society 122*, 10761-10768.

41. Pourianazar, N. T., Mutlu, P., and Gunduz, U. (2014) Bioapplications of poly(amidoamine) (PAMAM) dendrimers in nanomedicine, *Journal of Nanoparticle Research 16*.

42. Majoros, I. J., Williams, C. R., and Baker, J. R. (2008) Current dendrimer applications in cancer diagnosis and therapy, *Current Topics in Medicinal Chemistry 8*, 1165-1179.

43. Baird, E. J., Holowka, D., Coates, G. W., and Baird, B. (2003) Highly effective poly(ethylene glycol) architectures for specific inhibition of immune receptor activation, *Biochemistry 42*, 12739-12748.

44. Ottaviani, M. F., Cangiotti, M., Fiorani, L., Fattori, A., Wasiak, T., Appelhans, D., and Klajnert, B. (2012) Kinetics of Amyloid and Prion Fibril Formation in the Absence and Presence of Dense Shell Sugar-Decorated Dendrimers, *Current Medicinal Chemistry 19*, 5907-5921.

45. He, Z. Q., Uchimiya, M., and Cao, H. P. (2014) Intrinsic Fluorescence Excitation-Emission Matrix Spectral Features of Cottonseed Protein Fractions and the Effects of Denaturants, *Journal of the American Oil Chemists Society 91*, 1489-1497.

46. Bohren, K. M., Vonwartburg, J. P., and Wermuth, B. (1987) Kinetics of Carbonyl Reductase from Human-Brain, *Biochemical Journal 244*, 165-171.

47. Zhou, T. Q., and Rosen, B. P. (1997) Tryptophan fluorescence reports nucleotide-induced conformational changes in a domain of the ArsA ATPase, *Journal of Biological Chemistry 272*, 19731-19737.

48. Schlick, K. H., Lange, C. K., Gillispie, G. D., and Cloninger, M. J. (2009) Characterization of Protein Aggregation via Intrinsic Fluorescence Lifetime, *Journal of the American Chemical Society 131*, 16608-+.

49. Holub, O., Seufferheld, M. J., Govindjee, C. G., Heiss, G. J., and Clegg, R. M. (2007) Fluorescence lifetime imaging microscopy of Chlamydomonas reinhardtii: non-photochemical quenching mutants and the effect of photosynthetic inhibitors on the slow chlorophyll fluorescence transient, *Journal of Microscopy-Oxford 226*, 90-120.

50. Lakowicz, J. R. (2006) *Principles of fluorescence spectroscopy*, 3rd ed., Springer, New York.

51. Sundberg, S. A. (2000) High-throughput and ultra-high-throughput screening: solution- and cell-based approaches, In *Current Opinion in Biotechnology*, pp 47-53, Elsevier.

52. Hornig, J., and McGregor, A. (2014) Design and development of antivirals and intervention strategies against human herpesviruses using high-throughput approach, *Expert Opinion on Drug Discovery 9*, 891-915.

53. (2008) Standardization and Quality Assurance in Fluorescence Measurements I: Techniques, *Standardization and Quality Assurance in Fluorescence Measurements I: Techniques 05*, 1-496.

54. Muretta, J. M., Kyrychenko, A., Ladokhin, A. S., Kast, D. J., Gillispie, G. D., and Thomas, D. D. (2010) High-performance time-resolved fluorescence by direct waveform recording, *Review of Scientific Instruments 81*, 8.

55. Dean, K. M., and Palmer, A. E. (2014) Advances in fluorescence labeling strategies for dynamic cellular imaging, *Nature Chemical Biology 10*, 512-523.

56. Yamauchi, K., Yang, M., Jiang, P., Xu, M. X., Yamamoto, N., Tsuchiya, H., Tomita, K., Moossa, A. R., Bouvet, M., and Hoffman, R. M. (2006) Development of real-time subcellular dynamic multicolor imaging of cancer-cell trafficking in live mice with a variable-magnification whole-mouse imaging system, *Cancer Research 66*, 4208-4214.

57. Vogt, R. F., Jr., Marti, G. E., and Zenger, V. (2008) Quantitative Fluorescence Calibration: a Tool for Assessing the Quality of Data Obtained by Fluorescence Measurements, *Standardization and Quality Assurance in Fluorescence Measurements I: Techniques 05*, 3-31.

58. International, A. (2014) ASTM E2719-09, In *Standard Guide for Fluorescence--Instrument Calibration and Qualification*, ASTM International, West Conshohocken, PA.

59. Lakowicz, J. R. (2006) *Principles of fluorescence spectroscopy*, 3rd ed., Springer, New York.

60. Gardecki, J. A., and Maroncelli, M. (1998) Set of secondary emission standards for calibration of the spectral responsivity in emission spectroscopy, *Applied Spectroscopy 52*, 1179-1189.

61. Lakowicz, J., R. (2006) *Principles of fluorescence spectroscopy*, 3rd ed., Springer, New York.

62. International, A. (2013) ASTM E578-07, In *Standard Test Method for Linearity of Fluorescence Measuring Systems*, ASTM International, West Conshohocken, PA.

63. Albani, J. R. (2014) Origin of Tryptophan Fluorescence Lifetimes. Part 2: Fluorescence Lifetimes Origin of Tryptophan in Proteins, *Journal of Fluorescence 24*, 105-117.

64. Ghosh, S., Paul, B. K., and Chattopadhyay, N. (2014) Interaction of cyclodextrins with human and bovine serum albumins: A combined spectroscopic and computational investigation, *Journal of Chemical Sciences 126*, 931-944.

65. Boens, N., Qin, W. W., Basaric, N., Hofkens, J., Ameloot, M., Pouget, J., Lefevre, J. P., Valeur, B., Gratton, E., Vandeven, M., Silva, N. D., Engelborghs, Y., Willaert, K., Sillen, A., Rumbles, G., Phillips, D., Visser, A., van Hoek, A., Lakowicz, J. R., Malak, H., Gryczynski, I., Szabo, A. G., Krajcarski, D. T., Tamai, N., and Miura, A. (2007) Fluorescence lifetime standards for time and frequency domain fluorescence spectroscopy, *Analytical Chemistry 79*, 2137-2149.

66. Zhang, X. F., Zhang, J. L., and Liu, L. M. (2014) Fluorescence Properties of Twenty Fluorescein Derivatives: Lifetime, Quantum Yield, Absorption and Emission Spectra, *Journal of Fluorescence 24*, 819-826.

67. Yip, R. W., Wen, Y. X., and Szabo, A. G. (1993) Decay Associated Fluorescence-Spectra of Coumarin-1 and Coumarin-102 - Evidence for a 2-State Solvation Kinetics in Organic-Solvents, *Journal of Physical Chemistry 97*, 10458-10462.

68. Magde, D., Rojas, G. E., and Seybold, P. G. (1999) Solvent dependence of the fluorescence lifetimes of xanthene dyes, *Photochemistry and Photobiology 70*, 737-744.

69. Alfano, R. R., Shapiro, S. L., and Yu, W. (1973) Effect of soap on the fluorescent lifetime and quantum yield of rhodamine 6G in water, In *Optics Communications*, pp 191-192, Elsevier.

70. Vekshin, N. (2002) *Photonics of Biopolymers*, Springer-Verlag, Berlin.

71. Jones, G., Jackson, W. R., Choi, C., and Bergmark, W. R. (1985) Solvent Effects on Emission Yield and Livetime for Coumarin Laser-Dyes - Requirements for a Rotatory Decay Mechanism, *Journal of Physical Chemistry 89*, 294-300.

72. Liu, S. M., Kokot, S., and Will, G. (2009) Photochemistry and chemometrics-An overview, *Journal of Photochemistry and Photobiology C-Photochemistry Reviews 10*, 159-172.

73. de Juan, A., and Tauler, R. (2003) Chemometrics applied to unravel multicomponent processes and mixtures - Revisiting latest trends in multivariate resolution, *Analytica Chimica Acta 500*, 195-210.

74. Kasimova, M. R., Grigiene, J., Krab, K., Hagedorn, P. H., Flyvbjerg, H., Andersen, P. E., and Moller, I. M. (2006) The free NADH concentration is kept constant in plant mitochondria under different metabolic conditions, *Plant Cell 18*, 688-698.

75. Kania, A., and Fiedor, L. (2006) Steric control of bacteriochlorophyll ligation, *Journal of the American Chemical Society 128*, 454-458.

76. Thaler, C., and Vogel, S. S. (2006) Quantitative linear unmixing of CFP and YFP from spectral images acquired with two-photon excitation, *Cytometry Part A 69A*, 904-911.

77. Doering, K., Meder, G., Hinnenberger, M., Woelcke, J., Mayr, L. M., and Hassiepen, U. (2009) A Fluorescence Lifetime-Based Assay for Protease Inhibitor Profiling on Human Kallikrein 7, *Journal of Biomolecular Screening 14*, 1-9.

78. Pan, C.-P., Muino, P. L., Barkley, M. D., and Callis, P. R. (2011) Correlation of Tryptophan Fluorescence Spectral Shifts and Lifetimes Arising Directly from Heterogeneous Environment, *Journal of Physical Chemistry B 115*, 3245-3253.

79. Saraboji, K., Hakansson, M., Genheden, S., Diehl, C., Qvist, J., Weininger, U., Nilsson, U. J., Leffler, H., Ryde, U., Akke, M., and Logan, D. T. (2012) The Carbohydrate-Binding Site in Galectin-3 Is Preorganized To Recognize a Sugarlike Framework of Oxygens: Ultra-High-Resolution Structures and Water Dynamics, *Biochemistry 51*, 296-306.

80. Bittiger, H., and Schnebli, H. P. (1976) Concanavalin A as a Tool, *Bittiger, H. and H. P. Schnebli (Ed.). Concanavalin a as a Tool. Xv+639p. Illus. John Wiley and Sons: New York, N.Y., USA; London, England. Isbn 0-471-01350-1*, V-639.

81. Pace, C. N. (1990) Conformational Stability of Globular-Proteins, *Trends in Biochemical Sciences 15*, 14-17.

82. Pace, C. N., Shirley, B. A., McNutt, M., and Gajiwala, K. (1996) Forces contributing to the conformational stability of proteins, *Faseb Journal 10*, 75-83.

83. Pace, C. N. (1990) Measuring and Increasing Protein Stability, *Trends in Biotechnology 8*, 93-98.

84. Pace, C. N. (1975) The Stability of Globular Proteins, *Critical Reviews in Biochemistry 3*, 1-43.

85. Gauer, J. W., Sisk, R., Murphy, J. R., Jacobson, H., Sutton, R. B., Gillispie, G. D., and Hinderliter, A. (2012) Mechanism for Calcium Ion Sensing by the C2A Domain of Synaptotagmin I, *Biophysical Journal 103*, 238-246.

86. Singh, R. S., Tiwary, A. K., and Kennedy, J. F. (1999) Lectins: Sources, activities, and applications, *Critical Reviews in Biotechnology 19*, 145-178.

87. Cribbs, D. H., Kreng, V. M., Anderson, A. J., and Cotman, C. W. (1996) Cross-linking of concanavalin a receptors on cortical neurons induces programmed cell death, *Neuroscience 75*, 173-185.

88. Woller, E. K., Walter, E. D., Morgan, J. R., Singel, D. J., and Cloninger, M. J. (2003) Altering the strength of lectin binding interactions and controlling the amount of lectin clustering using mannose/hydroxyl-functionalized dendrimers, *Journal of the American Chemical Society 125*, 8820-8826.

89. Bouckaert, J., Hamelryck, T. W., Wyns, L., and Loris, R. (1999) The crystal structures of Man(alpha 1-3)Man(alpha 1-0)Me and Man(alpha 1-6)Man(alpha 1-0)Me in complex with concanavalin A, *Journal of Biological Chemistry 274*, 29188-29195.

90. Lis, H., and Sharon, N. (1998) Lectins: Carbohydrate-specific proteins that mediate cellular recognition, *Chemical Reviews 98*, 637-674.

91. Dundas, C. M., Demonte, D., and Park, S. (2013) Streptavidin-biotin technology: improvements and innovations in chemical and biological applications, *Applied Microbiology and Biotechnology 97*, 9343-9353.

92. Weber, P. C., Ohlendorf, D. H., Wendoloski, J. J., and Salemme, F. R. (1989) Structural Origins of High-Affinity Biotin Binding to Streptavidin, *Science 243*, 85-88.

93. Danguy, A., Camby, I., and Kiss, R. (2002) Galectins and cancer, *Biochimica Et Biophysica Acta-General Subjects 1572*, 285-293.

94. Nieminen, J., Kuno, A., Hirabayashi, J., and Sato, S. (2007) Visualization of galectin-3 oligomerization on the surface of neutrophils and endothelial cells using fluorescence resonance energy transfer, *Journal of Biological Chemistry 282*, 1374-1383.

95. Dumic, J., Dabelic, S., and Flogel, M. (2006) Galectin-3: An open-ended story, *Biochimica Et Biophysica Acta-General Subjects 1760*, 616-635.

96. Saraboji, K., Hakansson, M., Diehl, C., Nilsson, U. J., Leffler, H., Akke, M., and Logan, D. T. (2011) 3ZSJ: Crystal structure of Human Galectin-3 CRD in complex with Lactose at 0.86 angstrom resolution, *Protein Data Bank*.

97. Hirabayashi, J., Hashidate, T., Arata, Y., Nishi, N., Nakamura, T., Hirashima, M., Urashima, T., Oka, T., Futai, M., Muller, W. E. G., Yagi, F., and Kasai, K. (2002) Oligosaccharide specificity of galectins: a search by frontal affinity chromatography, *Biochimica Et Biophysica Acta-General Subjects 1572*, 232-254.

98. Ahmad, N., Gabius, H. J., Andre, S., Kaltner, H., Sabesan, S., Roy, R., Liu, B. C., Macaluso, F., and Brewer, C. F. (2004) Galectin-3 precipitates as a pentamer with synthetic multivalent carbohydrates and forms heterogeneous cross-linked complexes, *Journal of Biological Chemistry 279*.

99. Stone, N., and Meister, A. (1962) Function of Ascorbic Acid in Conversion of Proline to Collagen Hydroxyproline, *Nature 194*, 555-&.

100. Lepur, A., Salomonsson, E., Nilsson, U. J., and Leffler, H. (2012) Ligand Induced Galectin-3 Protein Self-association, *Journal of Biological Chemistry 287*, 21751-21756.

101. Yang, J., and Hlavacek, W. S. (2011) Scaffold-mediated nucleation of protein signaling complexes: Elementary principles, *Mathematical Biosciences 232*, 164-173.

102. Goodman, C. K., Wolfenden, M. L., Nangia-Makker, P., Michel, A. K., Raz, A., and Cloninger, M. J. (2014) Multivalent scaffolds induce galectin-3 aggregation into nanoparticles, *Beilstein Journal of Organic Chemistry 10*, 1570-1577.

103. Bargeron, C. B. (1974) Analysis of intensity correlation spectra of mixtures ofpolystyrene latex spheres: comparison of direct least squares fitting with the method of cumulants, *The Journal of Chemical Physics 60*, 2516-2519.

104. Wolfenden, M. L., and Cloninger, M. J. (2006) Carbohydrate-functionalized dendrimers to investigate the predictable tunability of multivalent interactions, *Bioconjugate Chemistry 17*, 958-966.

105. Skrdla, P. J. (2012) Roles of Nucleation, Denucleatiion, Coarsening, and Aggregation Kinetics in Nanoparticle Preparations and Neurological Disease, *Langmuir 28*, 4842-4857.

106. Spring, K. R., and Davidson, M. W. (2000-2013) Introduction to Fluorescence Microscopy, Nikon Microscopy U, http://www.microscopyu.com/articles/fluorescence/fluorescenceintro.html.

107. Munoz, E. M., Correa, J., Riguera, R., and Fernandez-Megia, E. (2013) Real-Time Evaluation of Binding Mechanisms in Multivalent Interactions: A Surface Plasmon Resonance Kinetic Approach, *Journal of the American Chemical Society 135*, 5966-5969.

108. Khan, M. I., Mandal, D. K., and Brewer, C. F. (1991) Interactions of Concanavalin-A with Glycoproteins - A Quantitative Precipitation Study of Concanavalin-A with the Soybean Agglutinin, *Carbohydrate Research 213*, 69-77.

109. Hermansson, M. (1999) The DLVO theory in microbial adhesion, *Colloids and Surfaces B-Biointerfaces 14*, 105-119.

110. Voorhees, P. W. (1992) Ostwald Ripening of 2-Phase Mixtures, *Annual Review of Materials Science 22*, 197-215.

111. Eisenber.H. (1971) Glutamate Dehydrogenase - Anatomy of a Regulatory Enzyme, *Accounts of Chemical Research 4*, 379.

112. Thusius, D. (1975) Mechanism of Bovine Liver Glutamate-Dehydrogenase Self-Assembly.2. Simulation of Relaxation Spectra for an Open Linear Polymerization Proceeding via a Sequential Addition of Monomer Units, *Journal of Molecular Biology 94*, 367-383.

113. Reisler, E., Pouyet, J., and Eisenber.H. (1970) Molecular Weights, Association, and Frictional Resistance of Bovine Liver Glutamate Dehydrogenase at Low Concentrations - Equilibrium and Velocity Sedimentation, Light-Scattering Studies, and Settling Experiments with Macroscopic Models of Enzyme Oligomer, *Biochemistry 9*, 3095.

114. Nangia-Makker, P., Balan, V., and Raz, A. (2012) Galectin-3-Binding and Metastasis, *Methods in Molecular Biology*, 251-266.

115. Ahmad, N., Gabius, H. J., Sabesan, S., Oscarson, S., and Brewer, C. F. (2004) Thermodynamic binding studies of bivalent oligosaccharides to galectin-1, galectin-3, and the carbohydrate recognition domain of galectin-3, *Glycobiology 14*, 817-825.

116. *Molecular Probes Handbook, A Guide to Fluorescent Probes and Labeling Technologies*, 11th ed.

APPENDICES

APPENDIX A

LIST OF NOVAFLUOR DATA COLLECTION ACRONYMS AND DEFINITION

Real-time Data

Collects and displays fluorescence decay curves at designated settings for a single sample. This type of collection allows users to optimize settings by viewing the resulting signal change in real-time. Only a single waveform can be saved from this measurement.

WTM: Wavelength-Time Matrix

WTM refers to wavelength time matrix and measures the time-resolved information at a range of emission wavelengths and a fixed excitation wavelength.

KIN: Kinetic

KIN refers to a kinetic measurement in which a series of waveforms are collected at time intervals determined by the averaging selected. The time required to acquire a single waveform at the selected averaging is determined by the pulse repitition frequency of the laser and time to transfer and digitize the signal. Approximate values are calculated by the software (Figure A1). This mode is excellent for studying kinetics of interactions occurring on the second to minute time scale.

STM: Series-time Matrix

Collects a designated number of fluorescence decay curves for a single well at fixed excitation, emission, temperature, attenuation and polarization settings. This type of measurement allows users to view time dependent changes in the fluorescence (binding kinetics, photochemistry).

WTM: Emission Wavelength-time Matrix

Collects fluorescence decay curves at various emission wavelengths. The integrated intensity plot provides what is conventionally known as the emission spectra.

XTM: Excitation Wavelength-time Matrix

Collects fluorescence decay curves at various excitation wavelengths. The integrated intensity of this type of measurement is conventionally known as an excitation spectrum.

MVM: Multi-Variable Matrix

This collection mode combines 2 of the above measurements into a single scan. Most commonly, it combines a sample-time matrix with one of the other modes. For example, if you would like to collect an emission spectrum for an entire plate, this mode would be used.

APPENDIX B

GALECTIN-3 EXPRESSION, PURIFICATION AND CHARACTERIZATION

Expression and Purification. Galectin-3 was expressed in *E. coli* transformed with the pGEX-6p-Galectin-3 vector and purified according to previous methods.[114] The bacteria were grown overnight (37°C, 250 rpm) in YT/AMP media then transferred to 1 L YT/AMP media and grown until the OD_{600} reached 1.2 (1-2 hours). At this point, 1 mL of 100 mM IPTG was added and incubation continued for another 4-5 hours. Bacteria were harvested by centrifuging for 15 minutes at 4000 rpm. Resuspended pellets (20% w/w in 1x PBS) were microfluidized then centrifuged at 9000 rpm for 10 minutes. The supernatant was incubated (1 hour, 4°C) with 0.25 mL Glutathione Sepharose (GS) 4B beads (50% w/w in PBS, GE Healthcare) per 12 mL supernatant. These were centrifuged (2000 rpm, 5 min) and washed 2-3 times with 3 mL 1x PBS then once with 1 mL cleavage buffer (50 mM Tris-HCl pH 7, 150 mM NaCl, 1 mM EDTA, 1 mM DTT). Overnight incubation (4°C) in 0.920 mL cleavage buffer and 0.080 mL PreScission Protease (GE Healthcare) cleaved protein product from sepharose. The protein solution was removed following centrifugation (2000 rpm, 5 min), then beads were washed twice with 1x PBS to remove all galectin-3. The three protein solutions were combined, then this solution was further purified using a lactose sepharose affinity column, with 0.2 M lactose displacement from the column followed by extensive dialysis in PBS (200 mL, 4-6 hours, on ice, switching buffer 2-3 times). As observed in Figure B.1 below, a high molecular weight band is observed for samples that are not subjected to the final affinity column purification (Lane 5) and for more weakly bound protein (PBS wash, Lane 6). The purity of the final galectin-3 product was verified by SDS-PAGE gel (15% agarose, 10 μL protein loaded), as shown in Lane 1 of the figure below.

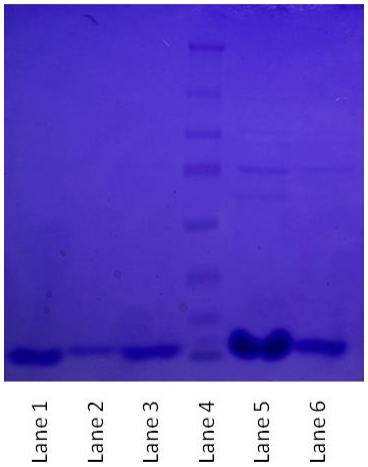

Lane	Sample
1	Galectin-3 product
2	Fraction 4—Buffer wash of galectin-3 loaded column
3	Fraction 2 – Buffer wash of galectin-3 loaded column
4	Ladder
5	Galectin-3 before additional purification on lactose column
6	Fraction 3—Buffer wash of galectin-3 loaded column

Figure B.1. SDS-PAGE of galectin-3 product and selected fractions from lactose affinity column.

Protein concentration was determined spectrophotometrically (280 nm, 1x PBS reference) using a previously reported $\varepsilon^{1\%}$ (6.1). [98, 115] Concentrations were adjusted by either dilution with 1x PBS or using a protein concentrator (Pierce) to afford a 45 μM solution (A_{280} = 0.81).

Alexa-labeled galectin-3 preparation. Purified galectin-3 (3mg/ml) was dialyzed (Spectrum Labs, MWCO 3500) for 2 hours then overnight in 100 mM sodium bicarbonate buffer (pH 8.3). Approximately 0.2mg AlexaFluor 488 succinimidyl ester (Molecular Probes) was dissolved in 20 μL DMSO and immediately added to 1 mL of the galectin-3 solution. The reaction was rotated for 1 hour at room temperature and was purified via dialysis (Spectrumlabs, MWCO 3500). The degree of labeling was determined according to the labeling protocol provided by Molecular Probes.[116] The solution of purified, Alexa-488 labeled galectin-3 was filtered and diluted to a final concentration of 31 μM.